


8-2016

Design and analysis of a high performance valve

Jordan M. Garrity
Purdue University

Follow this and additional works at: https://docs.lib.purdue.edu/open_access_theses

 Part of the [Bioresource and Agricultural Engineering Commons](#), and the [Mechanical Engineering Commons](#)

Recommended Citation

Garrity, Jordan M., "Design and analysis of a high performance valve" (2016). *Open Access Theses*. 945.
https://docs.lib.purdue.edu/open_access_theses/945

This document has been made available through Purdue e-Pubs, a service of the Purdue University Libraries. Please contact epubs@purdue.edu for additional information.

**PURDUE UNIVERSITY
GRADUATE SCHOOL
Thesis/Dissertation Acceptance**

This is to certify that the thesis/dissertation prepared

By Jordan Michael Garrity

Entitled

DESIGN AND ANALYSIS OF A HIGH PERFORMANCE VALVE

For the degree of Master of Science in Agricultural and Biological Engineering

Is approved by the final examining committee:

John H. Lumkes

Chair

Andrea Vacca

Gregory M. Shaver

To the best of my knowledge and as understood by the student in the Thesis/Dissertation Agreement, Publication Delay, and Certification Disclaimer (Graduate School Form 32), this thesis/dissertation adheres to the provisions of Purdue University's "Policy of Integrity in Research" and the use of copyright material.

Approved by Major Professor(s): John H. Lumkes

Approved by: Bernard A. Engel

Head of the Departmental Graduate Program

7/26/2016

Date

DESIGN AND ANALYSIS OF A HIGH PERFORMANCE VALVE

A Thesis

Submitted to the Faculty

of

Purdue University

by

Jordan M. Garrity

In Partial Fulfillment of the

Requirements for the Degree

of

Master of Science in Agricultural and Biological Engineering

August 2016

Purdue University

West Lafayette, Indiana

For Kassie.

ACKNOWLEDGEMENTS

This work was supported by the Center for Compact and Efficient Fluid Power, National Science Foundation Engineering Research Center funded under the cooperative agreement number EEC-0540834.

I'd like to start by thanking Dr. John Lumkes for his continued guidance and support spanning multiple projects over many years at Purdue. His mentorship will have a lasting impact on me. I would also like to thank my lab colleagues Tyler Helmus and Farid Breidi, whose feedback and friendship made my time in graduate school gratifying. Special thanks to David Wilson, Jeremy Robison, Dan Skelton, Shaoping Xiong, and Gabe Wilfong for their individual contributions and goodwill. I'd like to also acknowledge the help of Steve Weber of Sun Hydraulics who helped in the design and manufacturing of the spool valve and RB Machine Company for help in manufacturing the poppet valve. Lastly, I'm indebted in thanking my family for their endured support and encouragement.

TABLE OF CONTENTS

	Page
LIST OF TABLES	vii
LIST OF FIGURES	viii
NOMENCLATURE	xii
ABSTRACT	xv
CHAPTER 1. INTRODUCTION	1
1.1 Research Objectives	1
1.2 Motivation	1
CHAPTER 2. BACKGROUND	4
2.1 Digital Control in Hydraulics	4
2.1.1 Hydraulic Switching Control	4
2.2 High Speed Actuators	5
2.2.1 Solenoid Actuation	6
2.2.2 Active Material Actuation	7
2.2.2.1 Piezoelectric Actuation	7
2.2.2.2 Shape Memory Materials (SMMs) Actuation	9
2.2.2.2.1 Shape Memory Alloys (SMAs)	9
2.2.2.2.2 Magnetic Shape Memory Alloys (MSMAs)	9
2.2.3 Magnetostrictive Actuation	10
2.2.3 Voice Coil Actuation	11
2.2.4 Torque Motor	12
2.3 High Performance Valves	13
2.3.1 Production High Performance Valves	15
2.3.1.1 Parker VCD Valve	15

	Page
2.3.1.2 Sturman Digital Valve	16
2.3.1.3 MOOG Direct Drive Servo Valve (DDV).....	17
2.3.2 Researched High Performance Valves	18
2.3.2.1 Piloted Fast Switching Multi Poppet Valve	18
2.3.2.2 Direct Drive Piezostack Actuated Spool Valve.....	20
2.3.2.3 Bidirectional Check Valve.....	21
CHAPTER 3. VALVE AND ACTUATOR DESIGN	22
3.1 Primary Applications.....	22
3.2 Primary Requirements.....	22
3.3 ECA Design.....	23
3.3.1 Magnetorheological Fluid.....	23
3.3.2 Actuator Results.....	25
3.3.3 ECAV Design	25
CHAPTER 4. VALVE MODELING.....	28
4.1 Model Description.....	28
4.2 Electromagnetic Domain.....	29
4.2.1 ECA Circuit	29
4.2.2 MR Fluid Electromagnetic Domain.....	30
4.3 Fluidic Domain.....	31
4.3.1 Hydraulic Fluid Domain	32
4.3.2 MR Fluid Domain.....	41
4.4 Mechanical Domain	42
4.5 Model Implementation	46
CHAPTER 5. PROTOTYPE ECAV DESIGN	47
5.1 ECA Assembly	47
5.1.1 ECA Assembly Structural Analysis.....	48
5.1.1.1 Actuator Assembly	48
5.1.1.2 Actuator Box Assembly.....	49
5.2 Poppet Valve Assembly	52

	Page
5.2.1 Valve Block Design.....	52
5.2.2 O-Ring Selection	53
5.2.3 Valve Assembly Structural Analysis	55
5.2.3.1 Bolt Structural Calculation	55
5.2.3.2 Finite Element Analysis.....	56
5.3 Machined ECAV Assembly	58
5.4 Spool Valve Assembly	62
CHAPTER 6. EXPERIMENTAL TESTING	65
6.1 Test Stand Components.....	65
6.1.1 Sensors.....	66
6.2 NI Data Acquisition System.....	69
6.3 Electric Circuit	69
6.4 Actuator Setup and Experimental Results.....	70
6.5 Poppet Valve Setup and Experimental Results	72
6.5.1 Dynamic Poppet Experimental Results	75
6.6 Comparison with Simulation Performance	81
6.7 Spool Valve Setup and Experimental Results.....	82
6.7.1 Dynamic Spool Experimental Results	88
CHAPTER 7. CONCLUSION.....	94
LIST OF REFERENCES	96

LIST OF TABLES

Table	Page
Table 2.1 Comparison of active materials listed (Gauthier et al., 2006)	11
Table 2.2: Typical values for commercial solenoid on/off valves (Xiong, 2014)	14
Table 2.3: Typical dynamic values for 4-way spool type valves all rated at 15 L/min at 10 bar Δp (Plummer, 2016).....	18
Table 4.1: Poppet geometry variations	35
Table 5.1: Actuator component masses	59
Table 6.1: Test bench hydraulic components	66
Table 6.2: Sensors used on the test stand.....	67

LIST OF FIGURES

Figure	Page
Figure 1.1 Energy losses in mobile load sensing system (Love, 2012).....	2
Figure 1.2 Efficiency of on/off valves when comparing flow area and valve transition time (Merrill, 2012)	3
Figure 2.1 Switching control circuit comparison of a) electrical motor, b) hydraulic actuator (Scheidl, 2013).....	5
Figure 2.2: Hydac direct acting, solenoid cartridge valve (HYDAC, 2012)	7
Figure 2.3 Piezoelectric actuation methods (Plummer, 2016).....	7
Figure 2.4: Valve architecture and prototype (Chase et al., 2015)	8
Figure 2.5 Schematic layout of a servo valve with (a) magnetostrictive actuator mechanically amplified and (b) magnetically based (Karunanidhi & Singaperumal, 2009)	10
Figure 2.6: Parker Hannifin Voice Coil Drive (VCD) (Besch, 2012)	11
Figure 2.7 Torque motor assembly in a double flapper servo valve (Besch, 2012)	12
Figure 2.8: Parker Voice Coil Drive DFplus NG6 (Parker Hannifin Corporation, 2009)	15
Figure 2.9: Sturman High Speed Valve (Sturman, 1998).....	16
Figure 2.10: MOOG D633 Valve (MOOG, 2009)	17
Figure 2.11: Multi poppet design (left), pilot spool valve (right), (Winkler, et al., 2010)	19
Figure 2.12: Valve configuration for the piezostack DDV (Jeon et al., 2014).....	20

Figure	Page
Figure 2.13: BDCV schematic (Wilfong, 2011).....	21
Figure 3.1: Cross-section of ECA layout.....	23
Figure 3.2: Working principle (Truong & Ahn, 2012).....	24
Figure 3.3: Simulation and experimental results.....	25
Figure 3.4: ECAV layout (Skelton, 2014).....	26
Figure 3.5: Stacked valve configuration (Xiong, 2014).....	27
Figure 4.1: Modeling multi-domain subsystems.....	28
Figure 4.2: Electrical circuit for one coil set (Xiong, 2014).....	29
Figure 4.3: LORD 132DG fluid yield stress versus flux density (LORD, 2011).....	31
Figure 4.4: CFD geometry.....	34
Figure 4.5: Steady state flow force vs. poppet stroke.....	36
Figure 4.6: Poppet control volume for flow forces (Manring, 2005).....	38
Figure 4.7 Poppet configurations (Sorensen, 1999).....	39
Figure 4.8 FLUENT pressure gradient and streamline flow solved case.....	40
Figure 4.9: Schematic of mushroom shaped poppet (Lauttamus, 2006).....	41
Figure 4.10: Stribeck diagram (Black, 2003).....	44
Figure 4.11: FBD for the ECAV.....	45
Figure 4.12: Peak and hold voltage signal to resultant actuation force.....	46
Figure 5.1: ECA box cross section.....	47
Figure 5.2 Structural FEA on the actuator assembly.....	49
Figure 5.3: Actuator box assembly.....	50

Figure	Page
Figure 5.4: Cross section of valve block assembly.....	52
Figure 5.5: O-ring sealing locations.....	53
Figure 5.6: Updated sealing locations for the ECAV	54
Figure 5.7: Parker OC rod seal with cross section (Parker Fluid Power, 2007).....	55
Figure 5.8: Equivalent stress on valve assembly	57
Figure 5.9: Actuator subassembly front and side.....	58
Figure 5.10: Actuator Box Subassembly	60
Figure 5.11: Poppet valve block subassembly	62
Figure 5.12: Modified DNDC valve next to original model.....	63
Figure 5.13: CAD model of spool valve modifications.....	64
Figure 6.1: Calibrating the differential pressure transducer	68
Figure 6.2: VeriStand user interface	69
Figure 6.3: Displacement profile for one switch, 300RPM.....	71
Figure 6.4: Poppet valve hydraulic test circuit	72
Figure 6.5: Poppet valve test stand	73
Figure 6.6: Flow paths through the poppet valve	74
Figure 6.7: Pressure drop versus flow of the poppet valve.....	74
Figure 6.8: Displacement on/off profile.....	77
Figure 6.9: Poppet valve dynamic experimental results	79
Figure 6.10: Dynamic displacement profile.....	80
Figure 6.11: Simulated versus experimental results	81
Figure 6.12: Spool valve hydraulic test circuit	82

Figure	Page
Figure 6.13: Spool valve test stand	83
Figure 6.14: Step response (port B with high)	85
Figure 6.15: Step response (port A with high).....	87
Figure 6.16: Step response to position 1 with residual magnetism.....	88
Figure 6.17: Alternating flow directions on the spool valve	89
Figure 6.18: Switching high pressure from port A to port B	90
Figure 6.19: Switching high pressure from port B to port A	92

NOMENCLATURE

Symbol	Description	Units
A	Valve flow area	m^2
A_p	Projected area of seal	in^2
a_{poppet}	Acceleration value of main stage poppet	m/s^2
B	Magnetic flux density	T
B_{ave}	Average flux density of gap MR fluid	T
B_{ave_2D}	Average flux density of gap MR fluid, 2D axisymmetric	T
C_d	Discharge coefficient	1
b_{wall}	Damping coefficient of wall spring system	$N/m \cdot s^{-1}$
d_{coil}	ECA coil diameter	m
d_{core}	ECA core diameter	m
d_{disk}	ECA disk (outer) diameter	m
d_{in}	ECA disk inner diameter	m
d_{poppet}	Valve poppet diameter	m
d_{shaft}	Shaft diameter	m
d_{valve}	The diameter of valve poppet/spool	m
E	Electric field	V/m
E_{ind}	Induced electric potential	V
f_c	Friction coefficient due to O-ring compression	N/m
f_h	Friction coefficient due to fluid pressure	m^2
F_{a_2D}	Calculated ECA actuation force, 2D axisymmetric	N
$F_{actuation}$	ECA actuation force	N
F_C	Friction force due to O-ring compression	N
F_{flow}	Flow force	N
$F_{friction}$	Total friction force	N
F_H	Friction force due to fluid pressure	N
F_{oring}	Friction force from O-ring	N
F_p	Fluid pressure force	N
F_{spring}	Return spring force	N
F_{vf}	Fluid viscous friction force of sealing gap flow	N
F_{wall}	Wall force	N
H	Magnetic field intensity	kA/m
h_{gap}	Sealing gap height	m
h_{groove}	ECA disk groove gap height	m
h_{MRF}	MR Fluid gap height	m

h_{plate}	ECA disk plate thickness	m
i_{coil}	Current through the ECA coils	A
K	Fluid bulk modulus	Pa
K_c	Pressure flow gain	$m^3/(Pa \cdot s)$
K_{fc}	Pressure flow force coefficient	m^2
K_{fq}	Flow force gain	N/m
K_q	Flow gain	m^2/s
k_{relief}	Relief valve coefficient	$(Pa \cdot s)/m^3$
k_{spring}	Return spring coefficient	N/m
k_{wall}	Valve body wall stiffness	N/m
L_p	O-ring seal contact length	m
L_{stroke}	Piston stroke length	m
l_{coil}	ECA coil set central distance	m
m_{coil}	Coil mass	kg
m_{core}	Core mass	kg
m_{poppet}	Valve poppet mass	kg
m_{spool}	Wire spool mass	kg
N	Coil turns	1
P_{coil}	Coil driven power	W
p	Fluid pressure	Pa
p_{in}	Inlet fluid Pressure	bar
p_{out}	Outlet fluid Pressure	bar
R_{coil1}	Coil resistance, Coil I	Ω
R_{coil2}	Coil resistance, Coil II	Ω
R_{in}	Internal resistance	Ω
R_{line}	Line resistance	Ω
R_{line1}	Line resistance, Coil I	Ω
R_{line2}	Line resistance, Coil II	Ω
T_{shaft}	Torque on the motor shaft	$N \cdot m$
T_{react}	Reaction torque on the stepper motor	$N \cdot m$
t_{peak}	Coil peak voltage duration time	s
t_{switch}	Valve switching response time	s
V_{hold}	ECA Coil driven holding voltage	V
V_{peak}	ECA Coil driven peak voltage	V
V_s	Supply voltage for coil driving circuit	V
v_{ave}	Average flow velocity at inlet/outlet boundary	m/s
x	Displacement	m
x_{poppet}	Valve poppet displacement	m
x_{wall}	Depth valve poppet intruding into the wall	m
γ	Fluid shear rate	1/s
θ	Valve chamfer angle	rad
μ	Fluid viscosity	$Pa \cdot s$
μ_0	Reference magnetic permeability	1
μ_{MRF}	MR Fluid viscosity	$Pa \cdot s$
μ_r	Relative magnetic permeability	N/A^2

ρ	Fluid density or Charge density	kg/m^3 or C/m^3
ρ_0	Fluid density at 0bar(barometer)	kg/m^3
τ	MR fluid shear stress	$\text{Pa}\cdot\text{s}$
τ_{vf}	MR fluid viscous stress	$\text{Pa}\cdot\text{s}$
τ_{yd}	MR fluid yield stress	$\text{Pa}\cdot\text{s}$
ω	Motor shaft speed	rad/s

ABSTRACT

Garrity, Jordan M. M.S.A.B.E., Purdue University, August 2016. Design and Analysis of a High Performance Valve. Major Professor: John H Lumkes, Jr.

Most valves available in the fluid power industry today are capable of achieving either a large flow rate or a quick response time; however, often they are unable to deliver both simultaneously. Commercially available valves that can produce both at the same time require complex geometries with multiple actuation stages and piloting pressures, making them expensive components. To establish their active usage in applications across the fluid power industry, a reduction in price for these components is paramount.

The Energy Coupling Actuated Valve (ECAV) is capable of solving the large flow rates with fast actuation speeds trade-off by utilizing a new, high performance actuation system. The Energy Coupling Actuator (ECA) is an innovative actuation system that separates the kinetic energy source mass from the actuation mass. Intermittently coupling the actuator to a constantly rotating disk creates an energy transfer from the rotating disk's kinetic energy to the normally stationary actuator. This intermittent coupling process is controlled by changing the magnetic field inside the actuator's two coils.

Magnetorheological (MR) fluid resides in a 0.5mm fluid gap between the spinning disk and the actuator, and when the magnetic flux builds across this gap, it causes the actuator to move rapidly in a translational movement. The MR fluid changes to a solid between

the gap and frictionally binds the actuator to the disk, causing the actuator to move up or down, depending on which coil is actuated on the spinning disk. The liquid-solid conversion from the MR fluid occurs in less than one millisecond and is completely reversible. The shear strength of the fluid is proportional to the magnetic field strength inside the system. The actuator is connected to either a poppet or spool assembly for valve actuation, and the position is controlled through intermittently binding the actuator to the disk.

Two valve prototypes, one poppet and one spool type, were machined, and concept validation has been done in both simulation and experimentally. Experimental results show that the poppet reaches a 4mm displacement in 19.8ms opening and 17ms in closing under 33 L/min flow. The spool valve experimentally transitioned in 4.8ms at the same flow rate.

CHAPTER 1. INTRODUCTION

1.1 Research Objectives

The goal of this research was to integrate a high performance actuation system into a valve to achieve a dynamic response, and to experimentally test the actuation system controlling a prototype valve. The specific objectives were to:

1. Integrate the energy coupling actuator (ECA) with both a poppet and a spool valve body and experimentally investigate the performance of each
2. Develop the bidirectional proportional control algorithms for the energy coupling actuated valve (ECAV)
3. Develop an integrated system (driver circuits, sensors, actuator, and valve)

1.2 Motivation

The hydraulic valve is a common control component in many fluid power systems. Therefore, the entire system is heavily impacted by its inherent overall performance. According to a study by the Department of Energy (Love, 2012), valve energy losses in a mobile hydraulic load sensing system are attributed to:

1. Internal leakage
2. Metering losses from the pressure drop across the valve
3. Delay and slow transition response time

The study found that the main system inefficiencies were associated with the valves in the application. As seen in Figure 1.1 for a mobile machine load sensing system, valve losses alone summed to 43% of the total energy losses.

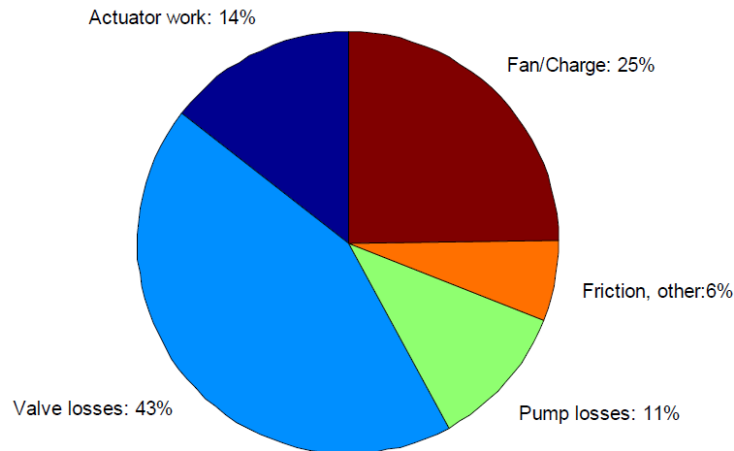


Figure 1.1 Energy losses in mobile load sensing system (Love, 2012)

Research in literature has investigated novel valve concepts and configurations in an attempt to solve this problem (Tu et al., 2012, Van de Ven et al., 2011, Winkler et al., 2010, Pohl et al., 2002, Johnson et al., 2001). Increasing the performance of valves is one example of a key enabler into reducing losses by decreasing the time normally spent throttling flow as the valve transitions from a closed to open position. Fast actuation speeds alone, however, are not sufficient to significantly decrease the losses experienced. State-of-the-art high speed valves should also deliver large flow rates to reduce metering losses across small orifice areas inside the valve. Merrill (2012), found that increasing the flow area of the valve, introducing a longer transition time, still resulted in an overall efficiency increase in the application of on/off high speed valves. In the figure below, a

70mm² flow area valve transitioning in 3ms is still more efficient than a 40mm² valve transitioning at 1ms.

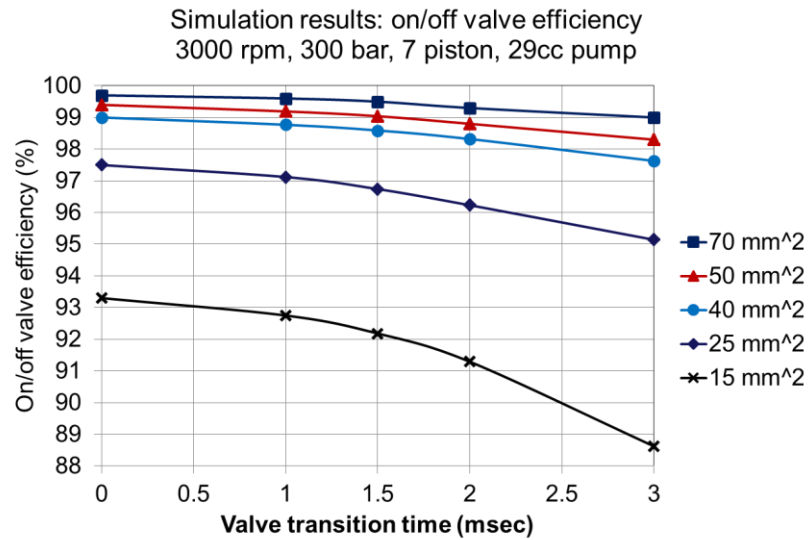


Figure 1.2 Efficiency of on/off valves when comparing flow area and valve transition time (Merrill, 2012)

Solving the tradeoff between large flow rates and fast actuation speeds seen in commercially available valves today would result in an energy savings for the system as a whole. One method of accomplishing this will come from the development of an economical valve that possesses a large flow gain with a rapid transition time.

CHAPTER 2. BACKGROUND

2.1 Digital Control in Hydraulics

The generic definition for a digital system involves a “number of discrete valued components (Linjama, 2008).” Digitally controlling hydraulic systems creates discretized values that can be used to resemble analog components. Research has demonstrated that using digital control over analog systems can increase energy efficiency while delivering a similar performance (Laamanen et al., 2004). Within digital fluid power exists two sub-branches of systems: systems involving components connected in parallel, and systems that are founded on switching technologies. Motivation in the area of switching control comes from the success of switching control seen in modern electric drives.

2.1.1 Hydraulic Switching Control

The key enabling component in digital fluid power is a high speed on/off valve. The performance of this valve dictates the overall operation of the system and is often the limiting factor in the pursuit of a high speed system. Figure 2.1 shows a fundamental analogy between an electrical and hydraulic switching circuit. In an electric motor, the current is driven from a pulse width modulation (PWM) voltage signal. It offers fast switching frequencies on a magnitude of 10^4 Hz with low fluctuations in angular speed (ω), ultimately yielding a constant output speed.

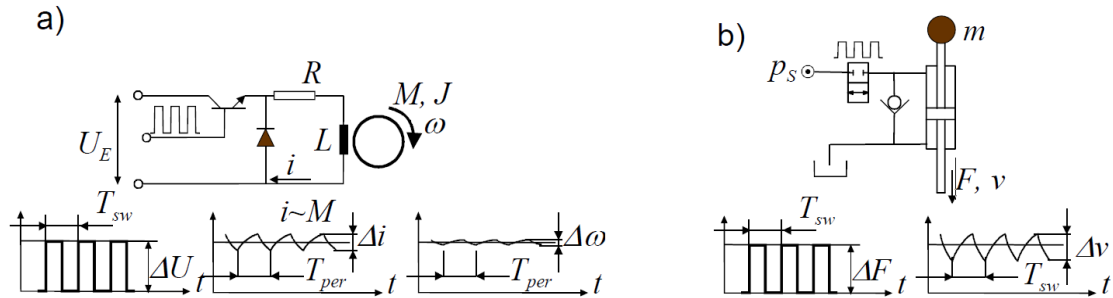


Figure 2.1 Switching control circuit comparison of a) electrical motor, b) hydraulic actuator (Scheidl, 2013)

Hydraulic switching inherently has larger speed fluctuations due to the hydraulic force rectangular signal corresponding with the acceleration of the actuator. For hydrostatic systems, the force is dependent upon pressure. This leads to large pressure pulsations with changes in force signal. Hydraulic systems have an innate high capacitance when compared to electrical systems, which gives them a low inductance to capacitance ratio (Merrill et al., 2010). This ultimately causes high structure-borne and fluid-borne noise. The main concern with this system is developing an economical fast-switching valve under high loads with a control algorithm that can handle pulsations. Advancements in valve technology need to be made in digital fluid power when compared to the progress made in the electrical domain in power semiconductor technology for hydraulic switching to become a realization (Scheidl et al., 2012).

2.2 High Speed Actuators

The actuation mechanism for a valve influences the opening and closing dynamics of the valve. Actuator types include manual, hydraulic, electric, and spring based control. The

actuator discussion below will focus on performance characteristics. Several aspects are key for actuators to obtain high performance characteristics ranging from a compact profile to large actuation force generation. Greater actuation forces accomplished by an actuator develops into a larger possible differential pressure between the control edges, which ultimately means an increased volumetric flow rate at a given orifice area.

2.2.1 Solenoid Actuation

The most common high speed valve actuation mechanism in the fluid power industry is the solenoid actuated valve. It is very reliable, basic in design, low in manufacturing costs, and delivers a moderately fast response. It consists of a coil set surrounding a ferrous core that is moveable with respect to the coil set when the coils are energized. It can be treated as an electromechanical transducer as it converts electrical signal to a mechanical force. A spring is required in single-solenoid actuators as the pulling effect is only in one direction. Forces generated by a solenoid reach a maximum at magnetic saturation of the iron core and decay with the moving position of the core, thus limiting strokes of these type of valves. Max flow rates for directly operated solenoid valves are generally around 45 L/min (Fitch & Hong, 2001). Response times for these valves are on the order of magnitude of tens of milliseconds. HYDAC, Figure 2.2, shows a poppet solenoid valve that is capable of generating 19 L/min in 35ms to turn on and 50ms to turn off.

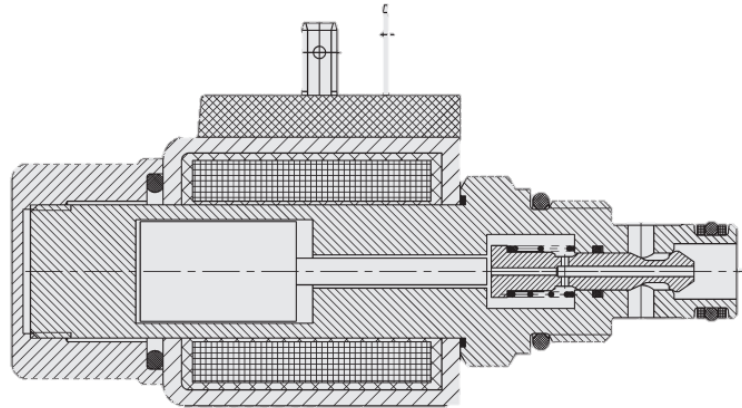


Figure 2.2: Hydac direct acting, solenoid cartridge valve (HYDAC, 2012)

2.2.2 Active Material Actuation

2.2.2.1 Piezoelectric Actuation

Piezoelectric (piezo) ceramics are constructed of a material that, when put under mechanical stress, generates an electrical charge. Piezos are also reversible in that when induced by an electric field, it generates strain and deforms quickly, creating a means for high frequency actuation. However, maximum strains attainable are in the order of 0.15%. There are three typical methods of actuation, shown in Figure 2.3.

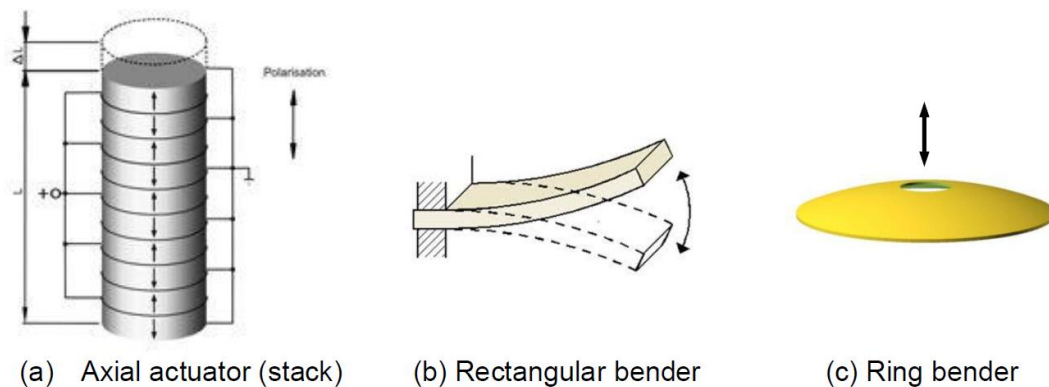


Figure 2.3 Piezoelectric actuation methods (Plummer, 2016)

Axial stacking, (a), allows for a longer stroke at lower operating voltages; however, typical operating voltages can be 100V or more. The rectangular type, (b), allows for acceptable displacement but at much lower force generation when compared to the stacked type. Rectangular benders also allow for an arrangement in an array to achieve a larger flow rate when compared to a single, larger orifice. Figure 2.4 shows a pneumatic prototype valve that utilizes this arrangement on the Micro-Electrical Mechanical Systems (MEMS) scale.

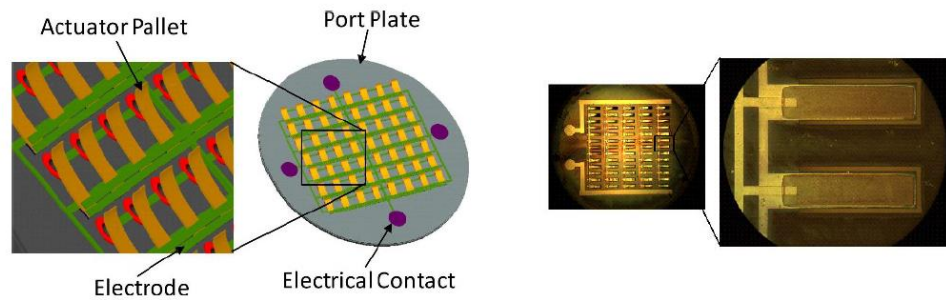


Figure 2.4: Valve architecture and prototype (Chase et al., 2015)

Ring benders, (c), can provide both adequate strokes (0.2mm max) and force generation between 10-100N while operating with voltages around 50V (Bertin et al., 2014). In general, some sort of motion amplification (mechanical or hydraulic) is often needed, even if used as a first stage actuation method. Piezoelectric materials are prone to large amounts of hysteresis (~20%), and more work is needed in reducing both electrical power consumption and heat generation inside the material (Sirohi & Chopra, 2003). Current technology in piezo actuated valves suggests that they are only suitable for pilot control with small flow rates.

2.2.2.2 Shape Memory Materials (SMMs) Actuation

2.2.2.2.1 Shape Memory Alloys (SMAs)

Shape memory alloys (SMAs) are metallic materials that after manipulation during a memorization process can return to their original shape or size. This transformation, named the shape memory effect (SME), takes place between two transformation phases, which is either temperature or magnetic field dependent. While the power to volume ratio is about the same when comparing SMA with hydraulic actuator technologies ($\sim 7\text{W}/\text{cm}^3$), SMA is principal in power to weight ratio (1.1 W/g versus 0.63 W/g for hydraulics) (Reynaerts & Brussel, 1998). There exist several challenges when incorporating SMAs that actuate through heat transfer into hydraulic valves due to its inherently low actuation frequency, low controllability, low accuracy, and low energy efficiency. However, SMA has demonstrated success in the aerospace industry in the innovative design of a hydraulic coupling that was first introduced on the F-14 jets in the 1970's (Jani, 2014).

2.2.2.2.2 Magnetic Shape Memory Alloys (MSMAs)

Magnetically transforming shape memory alloys can yield higher bandwidths up to 1 kHz. It offers strain rates comparable to SMAs when operating at lower temperatures with a maximum strain 32 times larger than magnetostrictive Terfenol-D. These materials could fill a niche for certain valve applications where large displacements at lower actuation forces exist, but they are still limited in application as they require low temperature for maximum operation and are very brittle. Further material improvements are needed for direct implementation into hydraulic valves (Jani, 2014).

2.2.2.3 Magnetostrictive Actuation

Like MSMA's, magnetostrictive materials transform shape when induced by a magnetic field. However, this effect is brought about by a rotation of the magnetization inside the material. In MSMA's, the effect is accomplished through "field-induced twin-boundary motion" (Handley, 2007). Research has been done recently in applying this material in a dynamic servo valve (Karunanidhi & Singaperumal, 2009; Yang et al., 2014). Figure 2.5 shows two methods researched in actuating the flapper nozzle of a servo valve. The mechanically amplified and magnetically biased actuator could achieve a time response of 0.68ms and 0.45ms respectively.

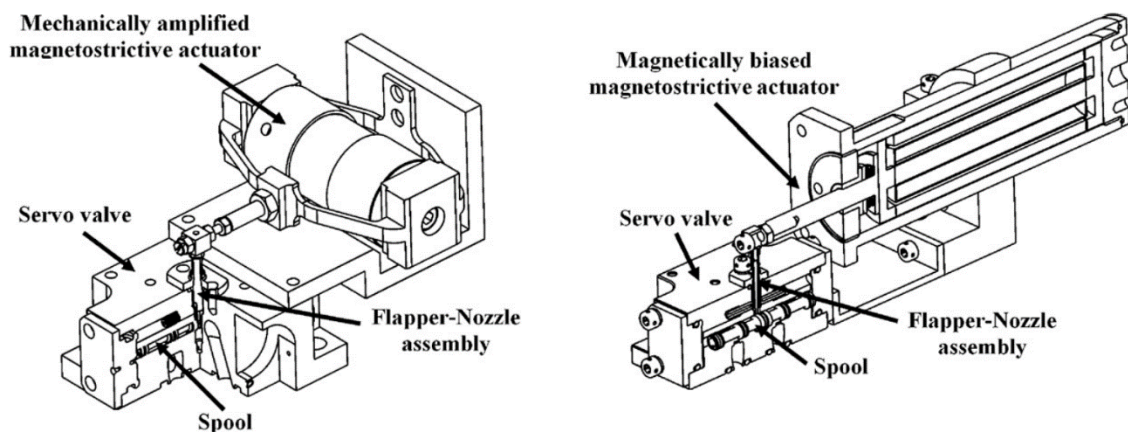


Figure 2.5 Schematic layout of a servo valve with (a) magnetostrictive actuator mechanically amplified and (b) magnetically based (Karunanidhi & Singaperumal, 2009)

Like the other active materials listed above, this technology is still limited by small strokes, hysteresis, and susceptible to temperature problems. When compared to SMA's, MSMA's fall short in actuation force generation and need some type of force amplifier for proper operation. Lastly, Table 2.1 compares the above active material actuation methods in regards to strain, stress, and response time of each material.

Table 2.1 Comparison of active materials listed (Gauthier et al., 2006)

	Piezoelectric (PZT)	Magnetostrictive (Terfenol-D)	SMA (NiTi)	MSMA (Ni-Mn-Ga)
Control Mode	Electric	Magnetic	Heat	Magnetic
Max Strain (%)	0.1-0.6	0.15-0.2	2-8	6-10
Blocking Stress (MPa)	100	70	250	3
Response Time	μ s	ms	s	ms

2.2.3 Voice Coil Actuation

Voice coil actuation operates similarly to a solenoid actuated valve and has been demonstrated reliably in industry. A coil set of copper wire (Figure 2.6) when energized creates a magnetic field that interacts with a ferrous pole plunger to actuate the valve. In a solenoid valve, it is the heavy ferrous core that shifts the valve. However, in a voice coil valve, it is the coil set that actuates the valve, creating a much more dynamic displacement profile due to its inherent lighter weight.

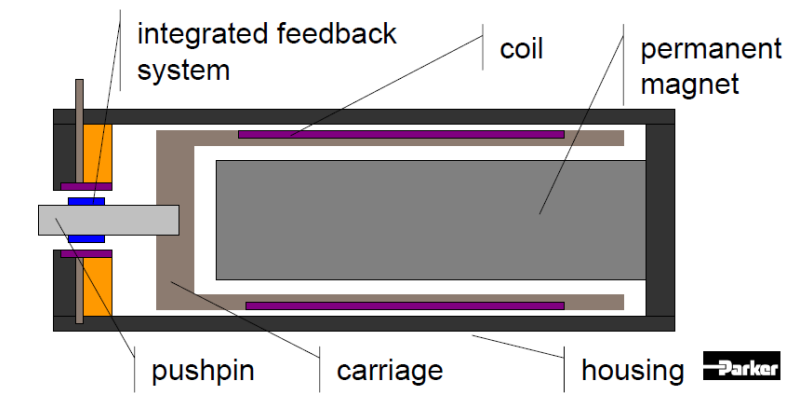


Figure 2.6: Parker Hannifin Voice Coil Drive (VCD) (Besch, 2012)

Parker Hannifin's permanent solenoid is made of a new material that increases the magnetic field 6 orders of magnitude when compared to a normal ferrous solenoid valve. Their actuator can attain 350 Hz, and the force generated is not stroke dependent like solenoids (Parker Hannifin, 2003).

2.2.4 Torque Motor

The torque motor is a widely accepted, bidirectional, proportional actuator. Figure 2.7 graphically details a torque motor attached to one of the most common servo valve designs with mechanical feedback. In this system, the torque motor acts as an electro-mechanical converter. The two coil sets are wrapped around the armature whose own ends are aligned with a permanent magnetic frame. An electrical signal (on the order of magnitude of around 20mW) sent to the coil sets builds up an increased magnetic field that ultimately results in armature movement (Ivantysyn & Ivantysynova, 2003).

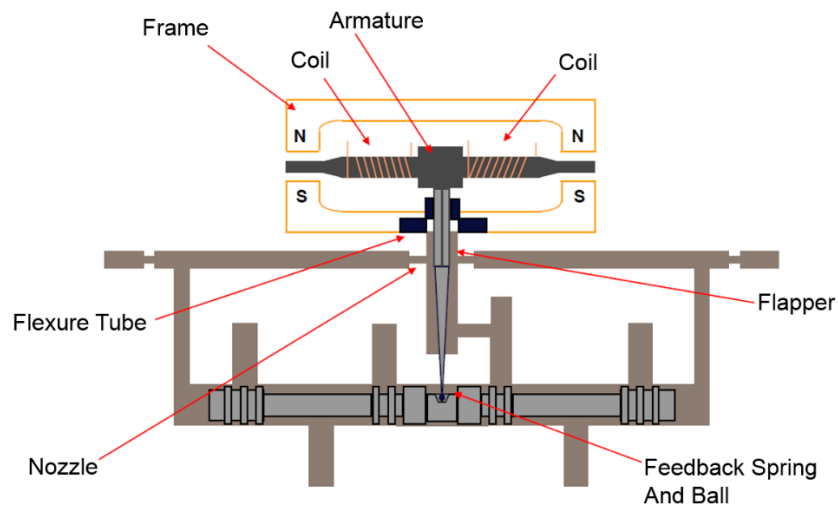


Figure 2.7 Torque motor assembly in a double flapper servo valve (Besch, 2012)

The flexure tube is the supporting element for the armature flapper combination. It allows a friction-free pivot while also separating the hydraulic fluid from the torque motor assembly. The flapper stroke is $\sim 0.1\text{mm}$, and as it moves, it also restricts flow at the nozzles. (Plummer 2016). This pressure differential creates a force imbalance on the spool, allowing it to actuate. While it moves, feedback through the spring and ball fixed to the spool is translated back to the flapper to ultimately move back to the neutral position, assuming a torque balance is achieved between the torque motor and the restoring forces. According to Plummer (2016), the spool actuation is around 1mm , and the ratio of electrical input power to hydraulic output power (power amplification factor) is $\sim 10^5$. Average hydraulic output power is a magnitude around 10kW . Additional stages would give additional amplification factors of $100:1$. This actuator is seen commonly on modern axial piston variable displacement pump designs that utilize electro-hydraulic control for the variable movement of the swashplate. However, this actuator is expensive due to the precise machining required. They have the highest radial clearances required, typically $2\text{-}4\ \mu\text{m}$, making them also prone to contamination (Watton, 2009).

2.3 High Performance Valves

As the last section focused mostly on the background behind high performance actuators, the following section focuses mainly on the incorporation of these high performance actuators into valves found, both in production and in state of the art research. While the performance of the actuator dictates the dynamics of the valve, the overall valve configuration and control algorithm also heavily impacts the operation profile. For example, solenoid valves innately lag in performance due to their heavy moving mass

and actuation force drop off with displacement; however, several research focuses have studied ways of improving the characteristics of these valves through new circuit designs, optimized control strategies, and innovative valve configurations to reduce response times to as little as 2ms (Mikkola et al., 2007; Breidi et al., 2014; Xu et al., 2014; Reuter et al., 2010). Table 2.2 depicts commercial solenoid valves and their common characteristics.

Table 2.2: Typical values for commercial solenoid on/off valves (Xiong, 2014)

	Valve Type	Response Time	Nominal Flow (5 bar Δp)	Size (mm) (Excluding Connectors)
Rexroth Bosch H-4WEH10	Pilot operated spool	On:50-70ms Off: 30-40ms	130 L/min	382×305×117
Parker DSH081	poppet valve	On:30ms Off:50ms	30 L/min	87.9×62.7×33.8
Hydac WS08D051	Direct operated poppet	On:35ms Off:45ms	17 L/min	146.5×60×36.3
Rexroth Bosch WE... SO407	Direct operated spool	On:25-45ms Off:10-25ms	50 L/min	206×90×45
Eaton SV3-8-C/CM	Pilot operated poppet	On:18ms Off:46ms	23 L/min	86×50.8×38.2

Spool and poppet configurations are the most commonly seen in valves. Each has its own shortfalls from leakage and high tolerances involved with spool configurations to large flow forces seen on poppet valves when used as direct actuation. Other novel configurations like the rotary spool valve and multi-poppet valve are researched attempts to make advancements in valve configurations (Tu et al., 2012; Winkler et al., 2010). The valves detailed below all have high bandwidths at varying flow rate levels.

2.3.1 Production High Performance Valves

2.3.1.1 Parker VCD Valve

Figure 2.8 below details the closed loop, spool type, directional control valve configuration with an integrated electronics drive and VCD.

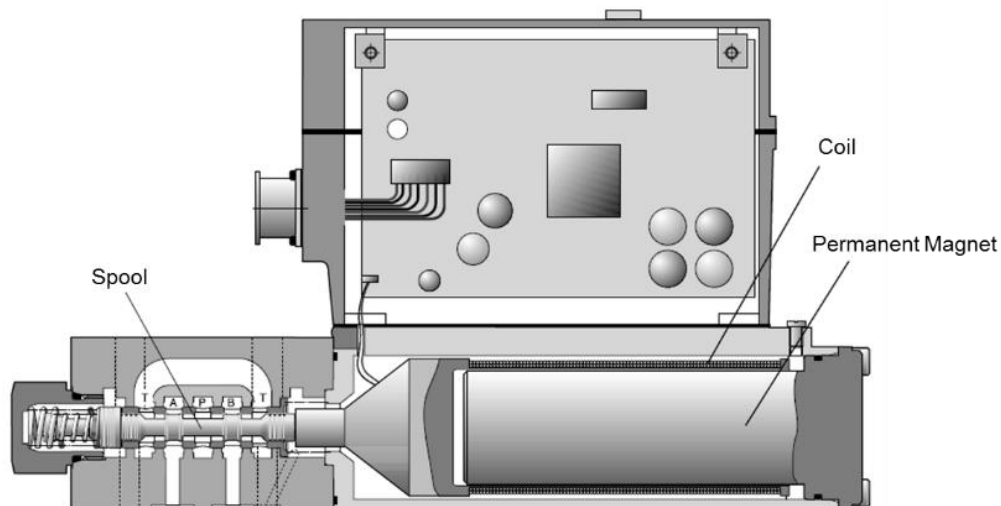


Figure 2.8: Parker Voice Coil Drive DFplus NG6 (Parker Hannifin Corporation, 2009)

Parker Hannifin's patented idea allows the spool to be directly connected to the moveable coil set instead of the permanent magnet. This valve generates a nominal flow of 40

L/min at 35 bar pressure drop with a step response in 3.5ms. It can generate an actuation force of 100N. An inductive position transducer sits between the coil set and the valve slider for position feedback. The valve has a position resolution of 0.021% with an accuracy to 0.5 μm (Parker Hannifin, 2003). This valve type has no deadband in the spool to sleeve interface, making it a highly precise piece to manufacture; this ultimately yields larger costs for the valve when compared to standard on/off valves.

2.3.1.2 Sturman Digital Valve

Sturman Industries manufactures a wide variety of fast switching digital latching valves. These switching times range between 0.25 and 1.5ms. Actuation is achieved via a dual electromagnet coil; significant energy can be saved through an innovative method of latching the valve with residual magnetism. The position of the spool inside the valve can be latched without the need for holding currents. Figure 2.9 shows a patented section view of their 3-way control valve. The model SI-1000 valve has a performance rating of 0.45ms switching time delivering 17 L/min at 10 bar Δp (Johnson et al., 2001).

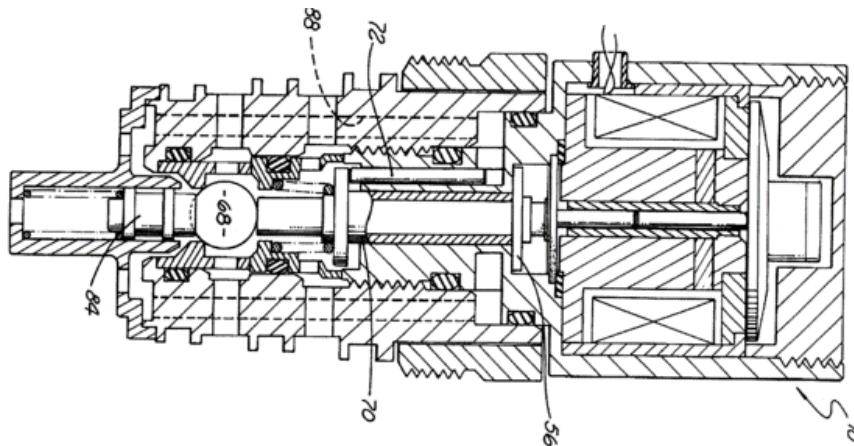


Figure 2.9: Sturman High Speed Valve (Sturman, 1998)

2.3.1.3 MOOG Direct Drive Servo Valve (DDV)

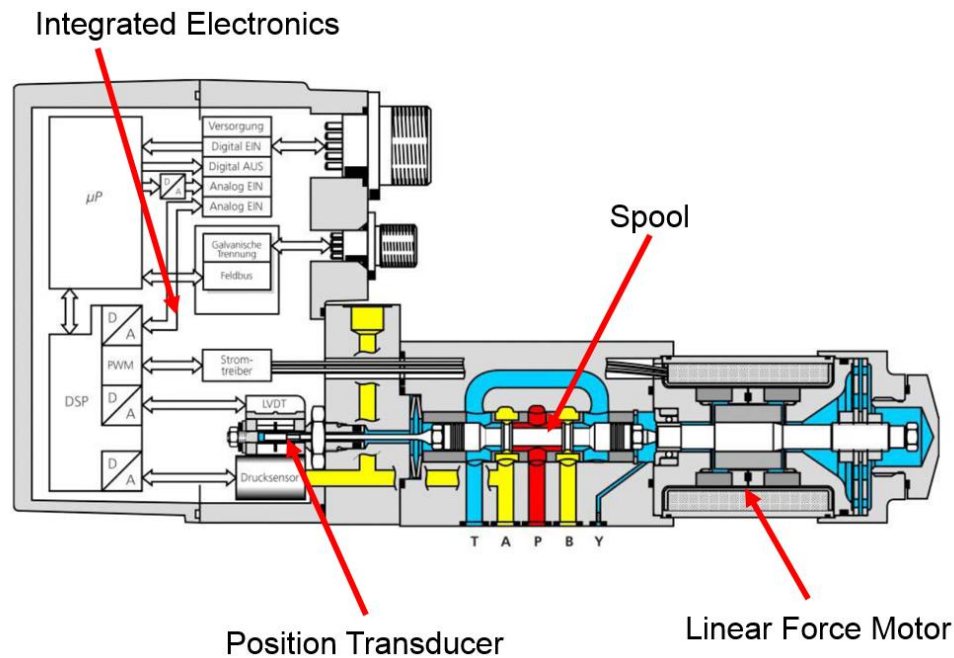


Figure 2.10: MOOG D633 Valve (MOOG, 2009)

Direct drive servo valves, (Figure 2.10), employ linear force motors for actuation. A major benefit of this valve over the flapper nozzle type servo valve is that this valve does not need two stages for operation, making it more economical than two stage servo valves. Like many other dynamic valves found today, this valve also has a closed loop control with integrated electronics for position feedback. An electrical signal is established in the form of a PWM current based on the desired spool position requested. This ultimately creates a proportional spool position based on the commanded signal. This direct acting valve can operate at pressures up to 350 bar and deliver flows up to 75 L/min. Typical response times for this valve are less than 12 ms at 0.2% hysteresis

(MOOG, 2009). Table 2.3 goes into more depth on typical values for valves similar to the MOOG D633.

Table 2.3: Typical dynamic values for 4-way spool type valves all rated at 15 L/min at 10 bar Δp (Plummer, 2016)

Spool Actuation Type	Direct Drive Valve (DDV)		Two-Stage Servo Valve	
	Proportional Solenoid Closed Loop	Linear Force Motor	Piloted, Mechanical Feedback	Piloted, Electrical Feedback
Actuation Force	~50 N	~200 N	~500N	~500 N
Hysteresis	2%	0.20%	2%	0.20%
Step Response (100%)	50ms	15ms	10ms	3ms
90deg phase lag frequency	10Hz	50Hz	100Hz	200Hz
Cost	low	medium	high	very high
Size	very large	very large	small	medium

2.3.2 Researched High Performance Valves

2.3.2.1 Piloted Fast Switching Multi Poppet Valve

A novel valve by Winkler et al., (2010) produced a valve capable of a nominal flow rate of 100 L/min with a switching time of 1-2 ms at a pressure drop of 5 bar.

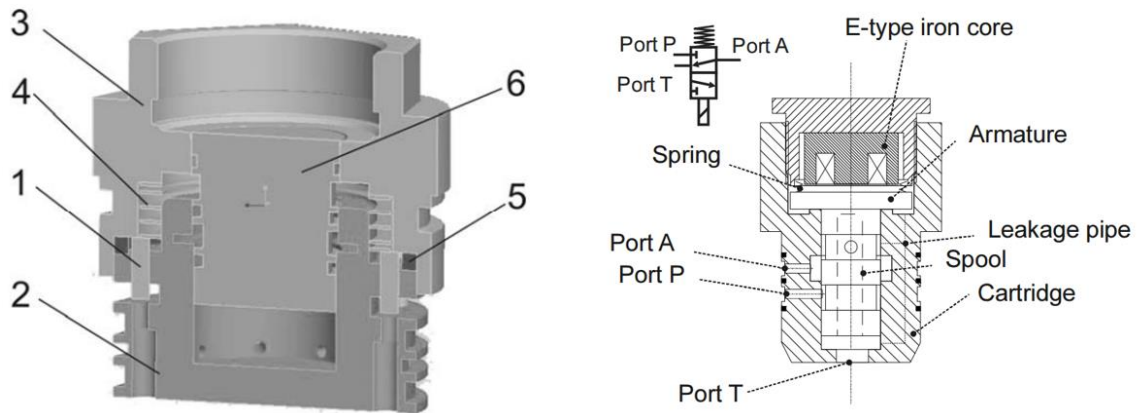


Figure 2.11: Multi poppet design (left), pilot spool valve (right), (Winkler, et al., 2010)

Figure 2.11 details the design of the mainstage 3/2 spool valve (right) and the multi poppet on the left. The basic concept behind this design is based on the relationship between increased flow rate and increased stroke length or poppet size diameter. The pilot valve (6) is inserted into the poppet housing (2 and 3). (5) represents a centering ring to align the compartments, and (1) represents one of the 14 poppets that exist around the valve housing. Lastly, (4) is the single wave spring common to all the poppets. The spool valve has two metering edges and is actuated through the use of an E-type iron core solenoid. The wave spring aids in the opposite direction of the solenoid to reach bi-directional movement (Winkler et al., 2010).

2.3.2.2 Direct Drive Piezostack Actuated Spool Valve

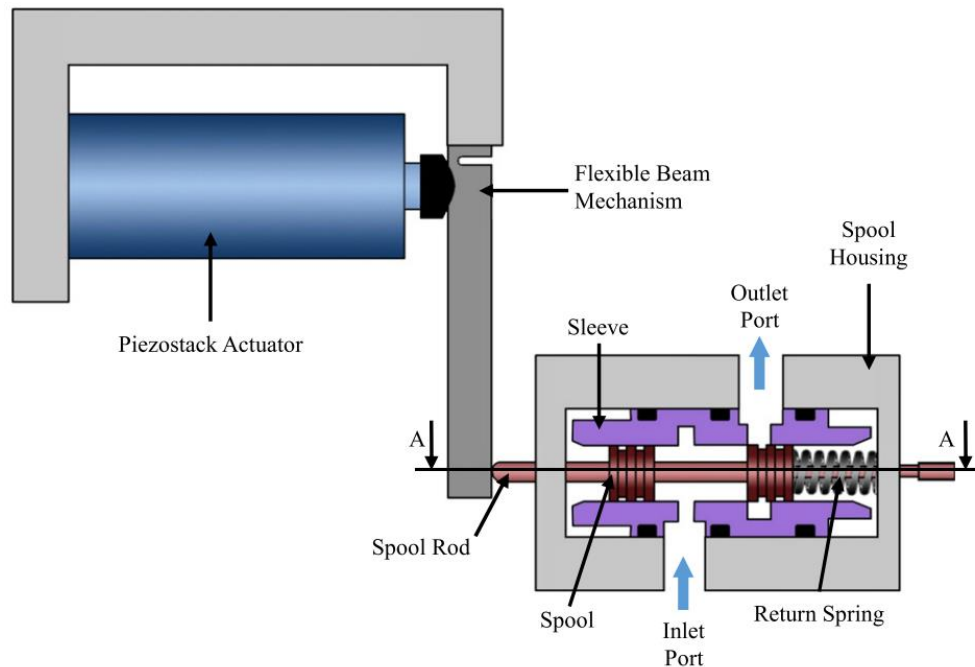


Figure 2.12: Valve configuration for the piezostack DDV (Jeon et al., 2014)

Jeon et al., (2014) simulated and tested a prototype piezostack directly driven spool valve. Piezostack actuation alone is limited to applications in piloting stages due to the limited stroke capabilities. This valve amplifies the actuation through a mechanical lever, making it capable of implementation into a single stage valve. The operation of the valve required an input voltage of 150V. The stack elongates proportionally with the voltage applied and deflects the beam counter-clockwise, creating a proportional position of the spool valve. This valve is limited to one-way actuation and relies on the dynamics of the return spring to close the inlet port with the outlet port. It achieved a 0.353mm displacement at a max flow rate of 7.65 L/min (Jeon et al., 2014).

2.3.2.3 Bidirectional Check Valve

Figure 2.13 depicts the design of a bidirectional check valve (BDCV).

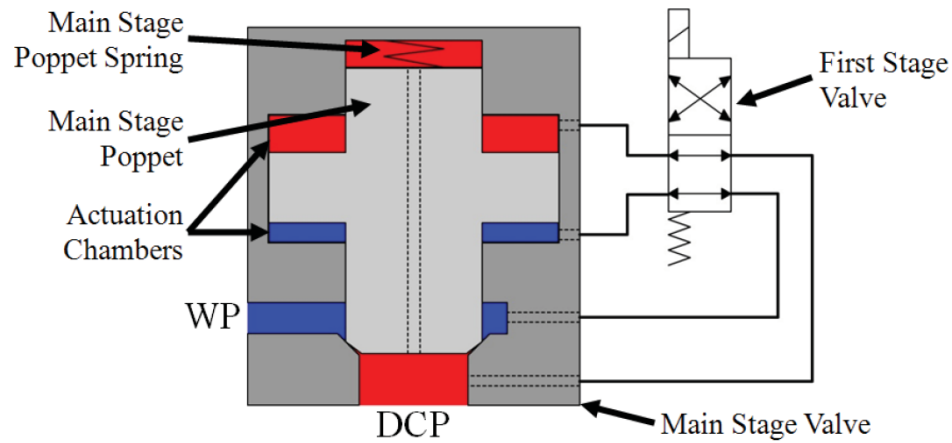


Figure 2.13: BDCV schematic (Wilfong, 2011)

A BDCV consists of a two stage, pilot-operated, pressure balanced seated poppet valve. The operating ports are the displacement chamber port (DCP) and the working port (WP). The first stage valve switches the pressure ports on the pressure balanced poppet to open the valve, allowing flow from DCP to WP. The poppet is designed to also allow reversible flow from WP to DCP and is two-way actuation compatible. Lastly, the valve is then closed by switching the piloting pressures. Results found experimentally showed that 30 L/min flows were achieved at a 5 bar Δp with a response time of 2-8ms.

CHAPTER 3. VALVE AND ACTUATOR DESIGN

3.1 Primary Applications

A typical application for the ECAV is any hydraulic circuit, in mobile or industrial applications, that requires a high dynamic response at comparatively large flow rates. Digital hydraulics is another potential application for implementing the valve. In general, this area of hydraulics requires on/off valves that are economical and reliably fast in switching states from off to on. This technology requires several valves in a circuit, thus requiring the valves to be relatively simple in operation and cheap to manufacture. While this valve could be operated as an on/off valve in digital hydraulics, it could also be utilized as a proportional valve. Examples of applications in industrial settings include multi-axis shaker tables, die casting machines, presses, and injection molding equipment.

3.2 Primary Requirements

Design considerations derived from background research coupled with ongoing research at Purdue University established the fundamental criteria for the ECAV. Below are the constraints.

1. 100 L/min nominal flow rate at 5 bar Δp (Flow area greater than 75mm²)
2. Symmetrical switching transition time of 3ms or less
3. Simple to manufacture, direct acting, pressure balanced, positive sealed valve designed for cost-effectiveness

3.3 ECA Design

This innovative actuation mechanism separates the mass of a kinetic energy source (rotating disk) from the actuation mass (poppet or spool valve) through an intermittent coupling and decoupling process. Figure 3.1 depicts a detailed view of the actuation mechanism. The rotating disk requires external power, either from an electric motor or engine/pump shaft, depending on the system implementation. The disk has a groove in it so that the translational piece can fit inside the disk, allowing two surfaces for the application of shearing force. The translational piece holds two coil sets on either side of the shaft spinning the disk and translates the actuation force to the poppet/spool valve that would exist below the actuator.

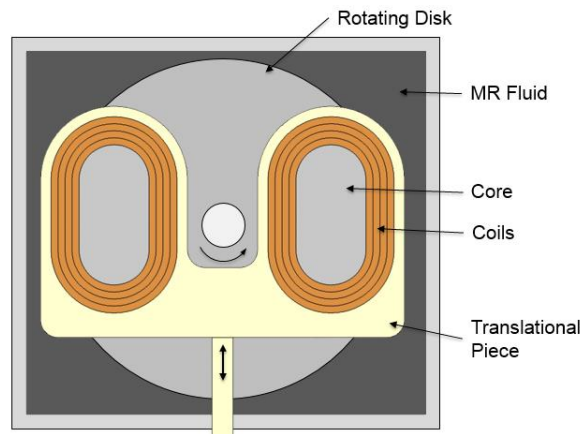


Figure 3.1: Cross-section of ECA layout

3.3.1 Magnetorheological Fluid

The working smart fluid is magnetorheological (MR) fluid. LORD MRF-132DG fluid is a hydrocarbon based MR fluid. Typical applications for this fluid are in controllable, energy-dissipating applications such as brakes, shocks, and dampers. Figure 3.2 shows the suspension of iron particles in the fluid when without and with a magnetic field

present. In a) the liquid behaves similarly to motor oil and is free to flow. When the magnetic field is produced, the micron sized iron particles align with the external field as they acquire a dipole moment. The chains of particles formed restricts fluid movement and creates a solidified system. This dynamic movement creates the shearing force, and is proportional to the magnetic field strength inside the system, allowing proportional control.

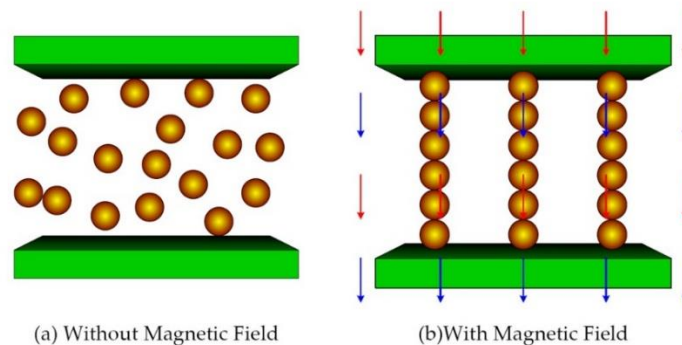


Figure 3.2: Working principle (Truong & Ahn, 2012)

When the coils in the ECA are not energized and the system is not magnetized, the liquid viscous friction forces between the rotating disk and the translational piece are small (Lord, 2011). Since the disk is spinning in a counterclockwise manner in the figure above, energizing the right coil set would create a magnetic flux across the gap between the disk and the translational piece and causes the MR fluid to thicken, thus generating a shearing force in the net upwards direction. This ultimately opens the valve. Similarly, energizing the left coil set actuates the translational piece downward to close the valve. The liquid-solid conversion is fast (<1ms) and reversible.

3.3.2 Actuator Results

The ECA has been investigated both in simulation and experimentation (Skelton, 2014; Xiong, 2014). The ECA was built, and a displacement profile can be seen in Figure 3.3. These results captured were at a 600rpm disk speed using a peak and hold circuit at 96V and 5V respectively. This investigation proved long stroke capabilities of the ECA when compared to other actuation mechanisms, as it was able to reach a 7mm stroke in 7ms.

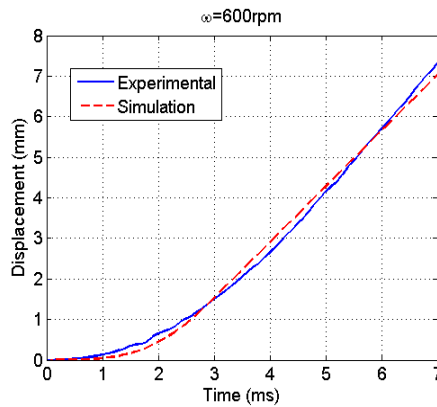


Figure 3.3: Simulation and experimental results

3.3.3 ECAV Design

Figure 3.4 shows the basic schematic of the ECAV. The same actuator can be used to drive both a poppet or spool valve proportionally or on/off in operation. The ECA assembly can scale to the operation required by the valve in the system it runs in.

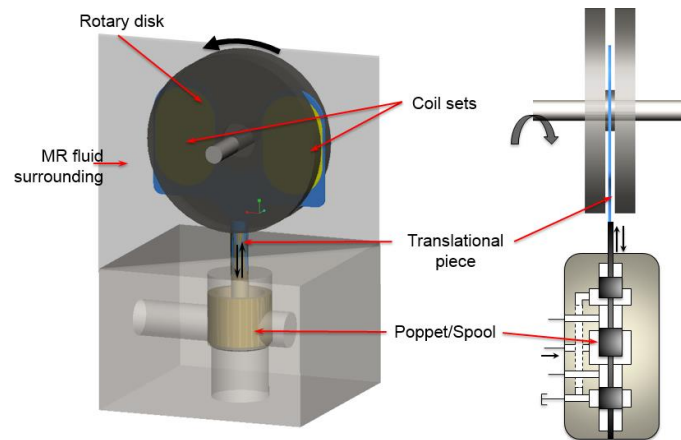


Figure 3.4: ECAV layout (Skelton, 2014)

Incorporating the ECA into a valve gives several advantages:

1. Small moving mass
2. High pressure allowed at either port
3. No pressure piloting necessary
4. Low leakage through positive poppet sealing
5. Proportional force control that is bidirectional and scalable
6. Large stroke capability
7. Compact axial stacking

The ECAV inherently has a small moving mass as the energy sourced mass has been separated from the actuation mass. The valve is also capable of two-way actuation regardless of system flow direction. The disk size along with rotational speed is scalable to achieve the actuation force necessary for the specific hydraulic application in operation. In this research, the valve is a direct acting valve that requires larger actuation forces to overcome flow forces and friction, thus leading to a larger disk size (100mm

diameter). Smaller disk sizes could have a more compact design if the ECAV was used in an application with smaller actuation force requirements. Figure 3.5 illustrates the axial compactness the ECAV offers if stacked on a common shaft. In the figure, there are 3 independent actuator/valve combinations that would be attractive in digital hydraulics and in compact areas in mobile hydraulics.

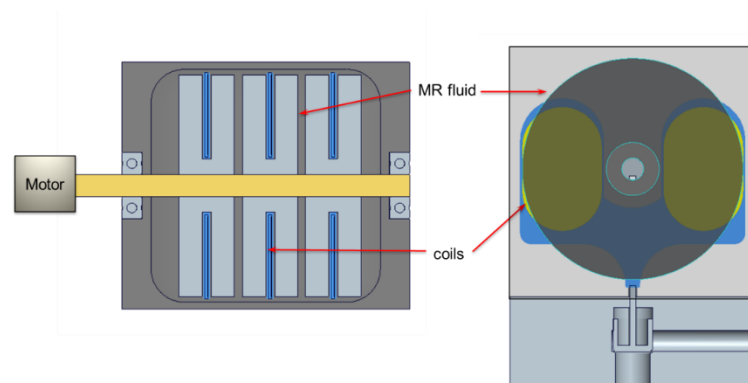


Figure 3.5: Stacked valve configuration (Xiong, 2014)

CHAPTER 4. VALVE MODELING

4.1 Model Description

The ECAV was simulated in a lumped parameter coupled multi-domain model within Simulink. Lumped parameter models are simpler and less computationally expensive when compared to models based on distributed parameters. The domains for this valve model included electromagnetic, fluidic, and mechanical domains. Figure 4.1 characterizes the relationship between the multiple domains in the model and their interaction with one another.

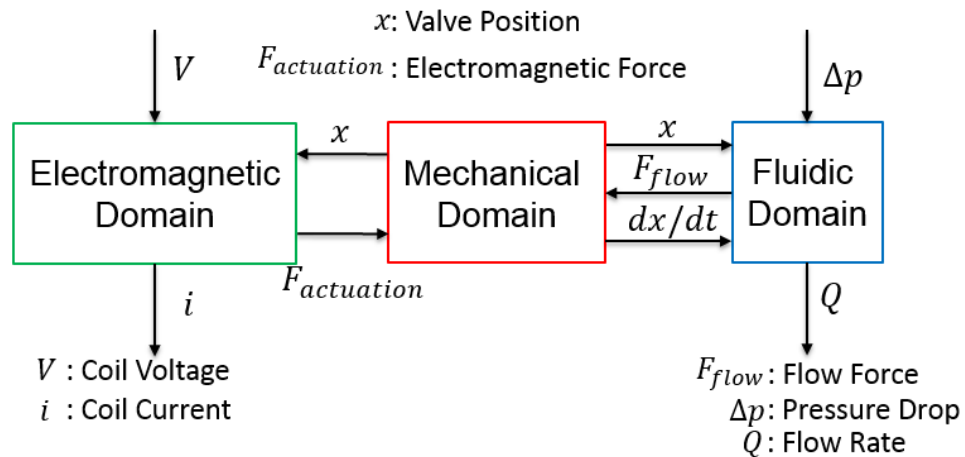


Figure 4.1: Modeling multi-domain subsystems

The actuation force is proportional to the shear strength of the MR fluid, which is proportional to the magnetic field strength inside the ECA. The magnetic field strength is dependent on coil current applied to the ECA. The initial model was built to capture the basic valve design and aided in the final design of the prototype. Fabricating the valve to be machinable with off the shelf components ultimately drove the model to be updated after the prototype was machined and assembled to more accurately describe the separate subsystems in the model to depict valve response time.

4.2 Electromagnetic Domain

4.2.1 ECA Circuit

Figure 4.2 below illustrates the electric circuit used to dynamically drive the coil sets. The power source V_s is a peak and hold profile. A capacitor in parallel with the voltage source steadies the rapid voltage changes. The two resistors represent the internal resistance in the system and the resistance from the lines. The coil is modeled as a resistor-inductor (RL) in series.

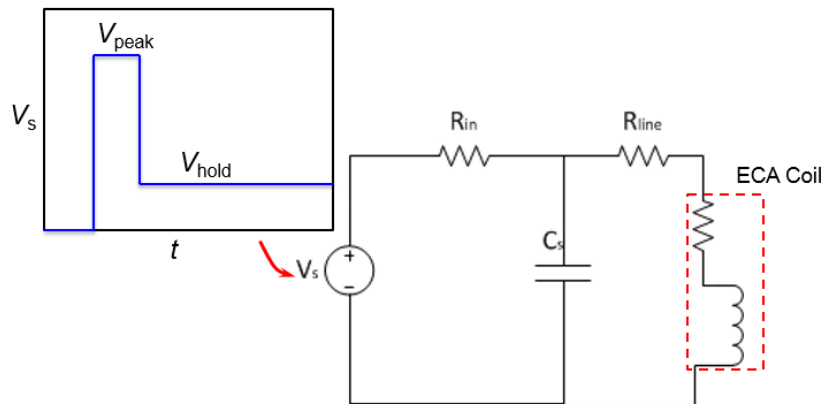


Figure 4.2: Electrical circuit for one coil set (Xiong, 2014)

The coil current inside each coil can be described in the following equations:

$$\begin{cases} V_c = i_{coil} \cdot (R_{line} + R_{coil}) + E_{ind} \\ (C_s \frac{dV_c}{dt} + i_{coil}) \cdot R_{in} + V_c = V_s \end{cases} \quad \text{Eq. 4.1}$$

Where E_{ind} is the electrically induced potential from the dynamic change in the magnetic field. This value was based on previous work using a 2D axisymmetric FEA solution of the magnetic flux density (B) in the system:

$$E_{ind} = \frac{d\Phi}{dt} = \frac{d\left(\int_{\Gamma_\Phi} B \cdot 2\pi r dr\right)}{dt} \quad \text{Eq. 4.2}$$

The average magnetic flux density in the FEA solution is solved for in Equation 4.3.

$$B_{ave_2D} = \frac{\int_0^{r_{core}} B \cdot 2\pi r dr}{\pi r_{core}^2} \quad \text{Eq. 4.3}$$

The magnetic flux (Φ) of the MR fluid gap at the core is calculated using Equation 4.4.

$$V = -N \cdot \frac{d\Phi}{dt} \quad \text{Eq. 4.4}$$

Where V is the voltage supplied to the ECA and N is the number of turns the copper wire wraps around the core.

4.2.2 MR Fluid Electromagnetic Domain

The yield stress equation for the MR fluid was created from a polynomial interpolation from the technical sheet provided by LORD Corp. Figure 4.3 graphically depicts the yield stress generated with an increasing magnetic flux density in the system.

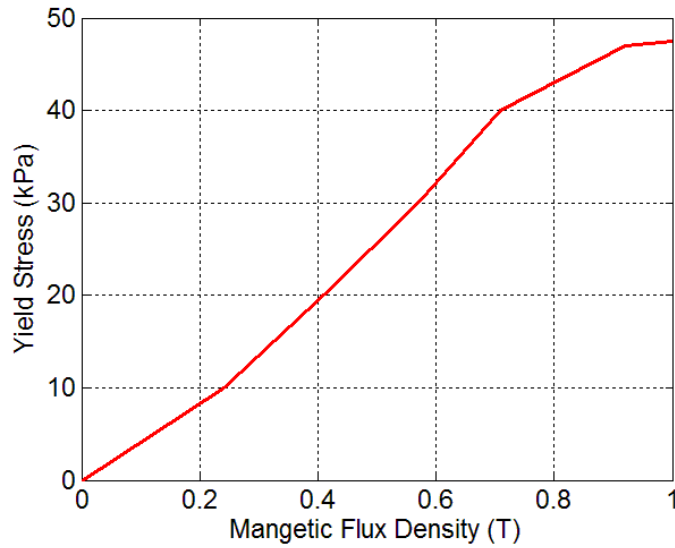


Figure 4.3: LORD 132DG fluid yield stress versus flux density (LORD, 2011)

The equation for yield stress is:

$$\tau_{yd}(B) = a_4 B^4 + a_3 B^3 + a_2 B^2 + a_1 B + a_0 \quad \text{Eq. 4.5}$$

Where $a_0=0.0983\text{kPa}$, $a_1=12.249\text{kPa/T}$, $a_2=146.66\text{kPa/T}^2$, $a_3=-155.87\text{kPa/T}^3$, $a_4=44.989\text{kPa/T}^4$ (Xiong, 2014). With the flux density (Equation 4.3) known, the yield stress the MR fluid generates can be calculated.

The steady state actuation force generated from the electromagnetic domain is:

$$F_{actuation} = \tau_{yd}(B_{ave_2D}) \cdot \pi R_{core}^2 \quad \text{Eq. 4.6}$$

These values were found and added to the valve model using a lookup table.

4.3 Fluidic Domain

Accurately capturing the fluid domain is essential for the valve to operate appropriately.

This domain describes the pressure drop across the valve, flow forces, leakages, and

viscous friction that take place inside the operation of the ECAV. Modeling techniques for each area are evaluated.

4.3.1 Hydraulic Fluid Domain

Flow through the orifice of a valve is governed by the pressure drop across it. This pressure drop is simulated in a laminar or turbulent flow model. Laminar pressure drops can occur at low pressure drops, low temperatures, or at small openings of long edged geometry orifices. Turbulent flow is generally found at small openings of sharp edged geometry orifices. The Reynolds number for a laminar flow is low when compared to a turbulent flow. Reynolds number can be described by (Manring, 2005):

$$\text{Re} = \frac{Q_o D_H}{A_o \nu} \quad \text{Eq. 4.7}$$

Where D_H is:

$$D_H = \sqrt{\frac{4A_o}{\pi}} \quad \text{Eq. 4.8}$$

Laminar and turbulent flows for hydraulic orifices are defined by the Reynolds number:

$$Q_o = \begin{cases} C_d A_o \sqrt{\frac{2|\Delta p|}{\rho}} * \text{sign}(\Delta p) & \text{for } \text{Re} \geq \text{Re}_{cr} \\ 2C_{d,lam} A_o \frac{D_H}{\nu \rho} \Delta p & \text{for } \text{Re} < \text{Re}_{cr} \end{cases} \quad \text{Eq. 4.9}$$

Where $C_{d,lam}$ is:

$$C_{d,lam} = \left(\frac{C_d}{\sqrt{\text{Re}_{cr}}} \right)^2 \quad \text{Eq. 4.10}$$

Poiseuille flow, Equation 4.11, modeled the leakage around the pressure balanced poppet spool seal interface. The flow here is assumed to be isothermal, laminar, with a constant gap height.

$$Q_{pois} = \frac{\pi d_{spool} h^3}{12 \rho \nu L_{spool}} \Delta p \quad \text{Eq. 4.11}$$

Viscous friction was modeled as a damping force from laminar gap flow. Couette flow was neglected in this model as it is considered negligible in dynamic valve motion.

$$F_{vf, pois} = -\pi r h \Delta p \quad \text{Eq. 4.12}$$

Flow forces, especially in direct acting valves, impede upon the dynamic characteristics and can even result in the valve not actuating to full stroke. Flow forces derive from a change in momentum in the valve as the flow passes through an orifice and exits the valve. Flow forces have been quantified theoretically; however, several works have shown that these equations do not accurately capture the full magnitude of both steady state and dynamic flow forces due to their model simplifications and valve geometry assumptions (Stone, 1960; Johnston et al., 1991; Bergada & Watton, 2004; Lugowski, 2015). Computational fluid dynamics (CFD) has demonstrated robust usage in predicting flow forces (Vaughan, Johnston, & Edge, 1992). CFD solves conservation equations for energy, mass, and momentum. For turbulent flows, additional transport equations are also solved. ANSYS FLUENT was chosen as the CFD software package in predicting flow forces. The results were ultimately added to the fluidic domain of the model as a lookup table.

$$F_{flow} = f(\Delta p, x) \quad \text{Eq. 4.13}$$

An axisymmetric 2D solver was used to compute flow forces on the pressure balanced poppet design. Basic valve geometry was established with assumptions including stroke and diameter. Figure 4.4 depicts the simplified valve CFD geometry. Reducing the 3D geometry to a 2D mesh along an axis of revolution greatly reduces the computational expense for solving several iterations quickly.

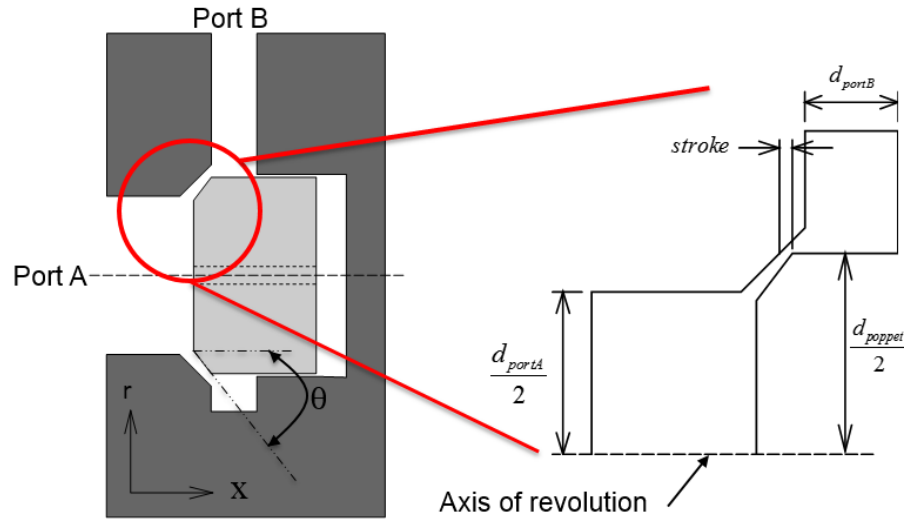


Figure 4.4: CFD geometry

The flow area (flow from A to B) is:

$$A = \pi d_{portA} x \sin(\theta) \left\{ 1 - \frac{x}{2d_{portA}} \sin(2\theta) \right\} \quad \text{Eq. 4.14}$$

For sharp edged orifices, this equation can be simplified to:

$$A = \pi d_{portA} x \quad \text{Eq. 4.15}$$

With a goal of 75mm² flow area or greater, poppet stroke and diameter were varied with respect to each other to predict flow forces while achieving 100 L/min nominal flow at a 5 bar Δp . Table 4.1 shows this comparison where each valve combination equals 75mm² or greater flow area. Considering the previous work on the ECA in developing an

actuator that could achieve up to 7mm displacement stroke, work on developing a valve with a 5+ mm stroke was desired.

Table 4.1: Poppet geometry variations

Poppet Type	Stroke (mm)	Diameter (mm)
1	1	24
2	1.5	16
3	3	8
4	5	5

The modeling parameters for CFD were:

1. 2D axisymmetric, steady state solver
2. Viscous model: k-epsilon
3. Fluid density: 875 kg/m^3 , viscosity = 32 cSt @ 40°C
4. Assumed constant density and kinematic viscosity
5. Set solver to converge when residuals < $1e-5$
 - a. Residuals: continuity, x & y velocity, k, epsilon

The stroke of the poppet was varied from .01 mm to 6mm at set intervals with varying intervals of pressure drop across the valve in both directions (from Port A to Port B and also from Port B to Port A). The total force reacting against the poppet and the corresponding flow rate was recorded for each interval. Flow forces were added to the model in the form of a lookup table given poppet stroke. Simulation was also done to match what the hydraulic trainer could produce, which is a max 100 bar Δp across the valve at a maximum flow of 33 L/min. Figure 4.5 graphically illustrates this simulation.

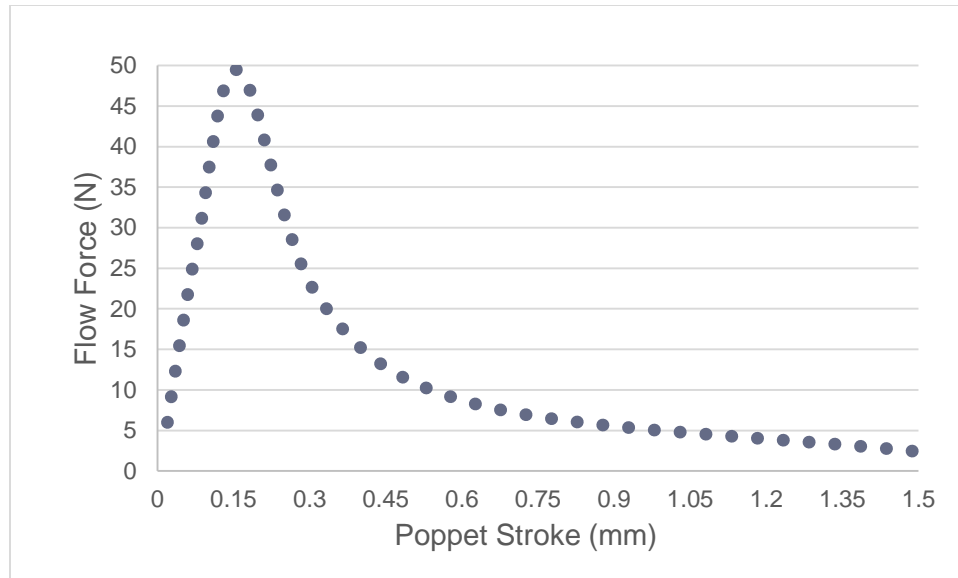


Figure 4.5: Steady state flow force vs. poppet stroke

In this plot, a flow-limited scenario was set so that to the left of the peak at 0.16mm, the pressure drop across the ports was set to 100 bar until full flow was achieved. Once the orifice became flow limited (right side of the peak), the pressure drop across the ports was reduced to stay at maximum flow allotted. This is often seen in hydraulic system startup when a machine is instantly connected to a high pressure line.

Simulating dynamic flow forces inside ANSYS FLUENT is set up by applying dynamic meshing to the valve geometry. A velocity profile for the valve inside the geometry must be specified for the CFD to solve. Time constraints prohibited the completion of dynamic simulation and subsequently was not implemented into the valve model. Steady state flow forces, in general, generate the magnitude of force that the valve needs to surmount. The transient flow forces will, however, impact the dynamic characteristics of the valve. Two terms amount to the dynamic flow force: one being proportional to the poppet's velocity and the other resulting from sudden changes in pressure in the hydraulic circuit.

Merritt, 1967 directs that the pressure transient term can be neglected; however, Manring in 2004 explained how this term can grow large enough to almost cancel out all the other transients in the dynamic flow force contribution. His work also showed that there is under a 2% difference in flow force calculation when assuming steady state only, in valves operating below 100 Hz. Wilfong, 2011 described that as valve frequency increases, the error also increases. For example, a valve operating at 300 Hz would have flow forces at approximately 11% less at steady state consideration only. With the ECAV operating within that frequency profile, it can be deduced that the valve model would be up to 11% off in error not including dynamic flow forces.

Manring 2005 described valve flow forces analytically. The equations for flow forces are:

$$F_{flow} = -\rho l K_q \left(\frac{dx}{dt} \right) - \rho l K_c \left(\frac{dp_s}{dt} \right) - K_{fq} x + (A - K_{fc}) p_s \quad \text{Eq. 4.16}$$

$$K_q = \pi d \sin(\theta) C_d \sqrt{\frac{2}{\rho}} p_s \quad \text{Eq. 4.17}$$

$$K_c = \frac{\pi d \sin(\theta) x C_d}{\sqrt{2 \rho p_s}} \quad \text{Eq. 4.18}$$

$$K_{fq} = 2\pi d \sin(\theta) p_s C_d^2 \cos(\theta) \quad \text{Eq. 4.19}$$

$$K_{fc} = 2\pi d \sin(\theta) x C_d^2 \cos \theta \quad \text{Eq. 4.20}$$

Where K_q is the flow gain, K_c is the pressure flow gain, K_{fq} is the flow force gain, and K_{fc} is the pressure flow force gain. The first two terms in Equation 4.16 are the dynamic terms described above, and the last two are the steady state terms. Figure 4.6 shows a positive sealing poppet valve control volume with the flow force designated. It is defined in the negative x-direction and works against the actuation force of the valve.

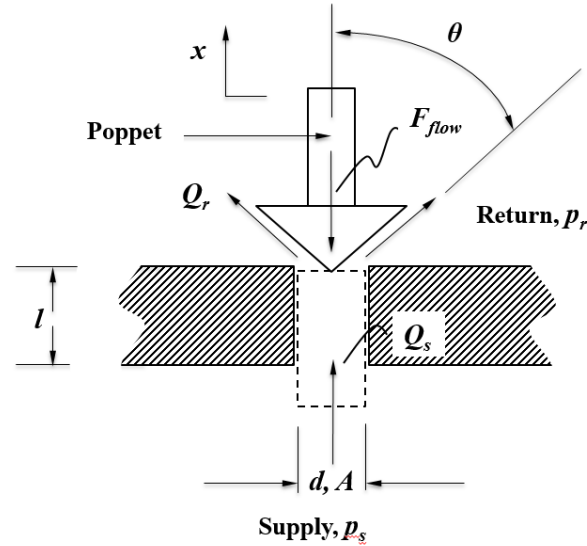


Figure 4.6: Poppet control volume for flow forces (Manring, 2005)

Previous work has shown that analytically solving for flow forces can be two to four times in magnitude higher or lower than from flow force results found through CFD (Wilfong, 2011). These inconsistencies arise from various assumptions, including poppet/seat geometry, jet angle and separation of the hydraulic fluid from the poppet, and downstream chamber sizes. From this information, CFD was ultimately chosen to describe flow forces in the valve model.

As Figure 4.5 showed, flow forces can be considerable in direct acting poppet valves. Initial modeling of flow forces generated values around 300N in magnitude at large pressure drops (~ 100 bar). Since this force opposes the actuation force, investigation into reducing flow forces for the prototype poppet was necessary. Sorensen (1999) investigated three different poppet styles, depicted in Figure 4.7. Valve A had a conical

seat with a sharp edged poppet, valve B was a square seated ball shaped poppet, and valve C was a square seated conical poppet.

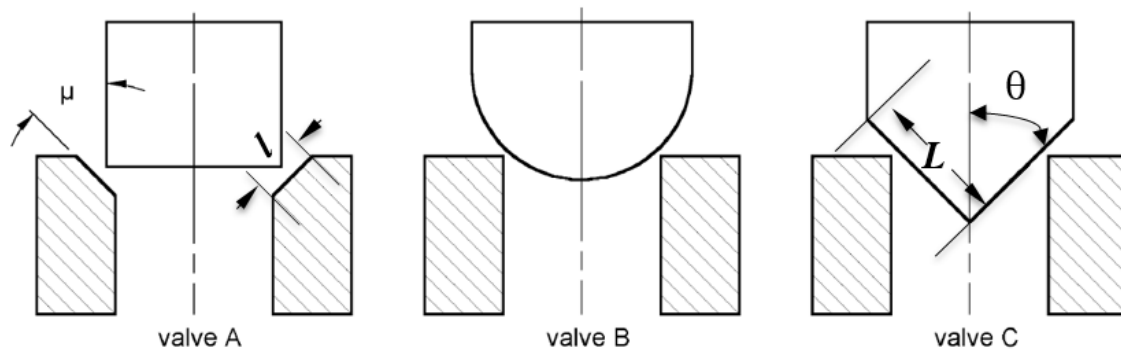


Figure 4.7 Poppet configurations (Sorensen, 1999)

Sorensen tested the three styles both experimentally and in simulation, conducting tests in the range of Reynolds numbers from 300 to 5000. Modeling was done in 2D axisymmetric simulations. From the experiments and simulation, the author concluded that for valve A, decreasing the seat angle (μ) decreases flow forces. Valve B showed that the flow coefficient (K_q) was independent of the flow jet angle. At low Re numbers, valve B generally showed increasing flow forces with increasing jet angle. Valve C results were similar to valve B due to a similar restriction of flow below the seat. Increasing the poppet angle (θ) of valve C with respect to the poppet axis reduced flow forces. In general, the author found that flow forces were largest in magnitude with valve B, while the smallest flow forces were seen in valve A. These results were consistent with the work done by Johnston et al. (1991) and Vaughan et al. (1992). CFD for the ECAV model explored valve types A and C with varying poppet/seat angles (μ & θ) and lengths (l & L). Results from the simulation study proved that a sharp edged poppet

(valve A poppet style) with a seat length (l) of 0.75mm at an angle (μ) of 60° had the lowest flow forces generated. Figure 4.8 graphically illustrates a solved case for this geometry layout.

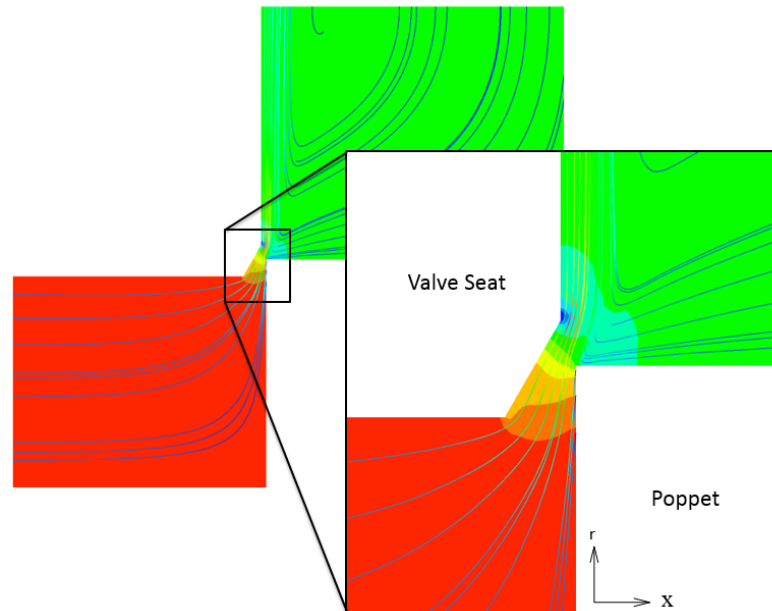


Figure 4.8 FLUENT pressure gradient and streamline flow solved case

The area of lowest pressure (colored dark blue in the figure) is developing at the seat away from the poppet so that the majority of the face of the poppet is still under full pressure. This is the desired case since the poppet is pressure balanced. The back side of the poppet will balance out the force generated from the high pressure acting upon the valves geometry.

Novel configurations of poppet valves have been investigated to help reduce flow forces. A favored design in reducing flow forces utilizes a seating spool valve with a mushroom shaped poppet. It has been researched extensively and is also available commercially (Lauttamus, 2006; Yousong et al., 1991; Cui et al., 1991; Yifei et al., 1989; Hydac 2016).

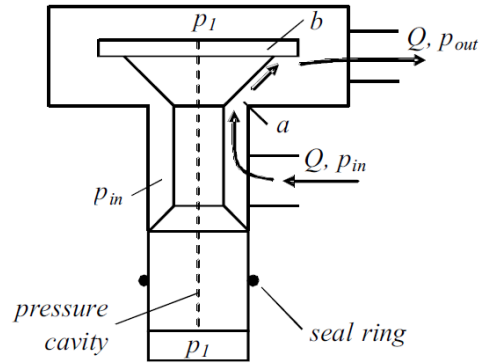


Figure 4.9: Schematic of mushroom shaped poppet (Lauttamus, 2006)

The basic operating principle of this valve, Figure 4.9, is that when the valve closes, it becomes pressure compensated as the bottom stem and top of the mushroom share the same pressure (p_1). Once opened, inside the restriction area a , pressure drops as flow direction changes and the valve will tend to close on itself. However, the top component of the mushroom head b , is affected as flow impacts the rim of its structure and a net impulse force upward is generated, allowing it to stay open. Modeling this type of valve for the ECAV was investigated but proved to not be suitable for the geometry required for the ECA. It also has a much less effect on flow forces at longer strokes and is not suitable for bidirectional flow.

4.3.2 MR Fluid Domain

The rotating disk inside the ECA gives the fluid an angular velocity, ω . The flow should remain laminar to guarantee proper dipole alignment when a magnetic field is present.

Reynolds number for the MR fluid is:

$$\text{Re} = \frac{\rho \omega R h_{MRF}}{\mu} \quad \text{Eq. 4.21}$$

Where h_{MRF} is 0.5mm. At a maximum shaft rotation speed of 1200 RPM, R of 50mm, density of $3 \times 10^3 \text{ kg/m}^3$, dynamic viscosity of 0.112 Pa*s, the equation results in a maximum Re of 1682. This value is well below critical Re of 2300, indicating that laminar flow is present in the system.

The shearing stress due to the viscous force is:

$$\tau_{vf} = \mu_{MRF} \frac{\omega r}{h_{MRF}} \quad \text{Eq. 4.22}$$

However, due to the balanced design of the actuator with two sides exposed to shearing MR fluid, the total shear force equals the MR fluid yield stress, τ_{yd} as the viscous friction forces cancel out.

4.4 Mechanical Domain

Modeling this domain sums cumulative forces and establishes the dynamic motion of the poppet. The actuation force, fluid forces, spring force, wall reaction forces, and friction forces are summed to equate the final resulting force.

The spring force that acts upon the poppet to hold it closed was modeled as a spring and damper system.

$$F_s = F_{s,o} + k_s x_s + b_s \frac{dx_s}{dt} \quad \text{Eq. 4.23}$$

The valve model also considers the wall reaction force to be a stiff spring and damper system. This force occurs when the poppet makes contact with the valve body seat at its closed position and with the top valve plate at the full stroke position. It has no impact on the model when the poppet is not in contact. The equation for the wall intrusion is:

$$F_{wall} = \begin{cases} k_{wall}x_{wall} + b_{wall} \frac{dx}{dt} & \text{for } x_{wall} > 0 \\ 0 & \text{for } x_{wall} \leq 0 \end{cases} \quad \text{Eq. 4.24}$$

O-rings add friction to the system when used as dynamic seals. Modeling the friction force was done using equations developed by Thoman (1992) and the Parker O-Ring Handbook ORD 5700 (2007).

$$F_{oring} = F_C + F_H \quad \text{Eq. 4.25}$$

$$F_C = f_c L_{r/p} \quad \text{Eq. 4.26}$$

$$F_H = f_h A_{r/p} \quad \text{Eq. 4.27}$$

$$f_h = \frac{1}{375} p + 68947.5 \quad \text{Eq. 4.28}$$

Where f_c is the friction coefficient from O-ring compression found empirically, f_h is the friction coefficient from the fluid pressure in operation, $L_{r/p}$ is the length of seal contact for a rod or piston groove, and $A_{r/p}$ is the projected sealing area of the rod or piston groove.

Glide rings are added to dynamic seals to reduce friction forces further. Predicting friction from glide rings is a difficult process. Coulomb and viscous friction models can be applied to dynamic sealing to predict friction. Coulomb friction influences the majority at lower velocities while viscous friction exists at higher velocities. This is commonly described in a Stribeck curve diagram, Figure 4.10. The dry friction region exists when no lubricant exists between the seal and mating surfaces. Only coulomb friction exists here. In the mixed region, the load is carried by the hydrodynamic pressure and the dry asperities. Here, the friction is at its minimal value. Lastly, in the

hydrodynamic region, a film of lubricant separates the two surfaces. Viscous friction dominates this region with an increasing friction force with increasing velocity.

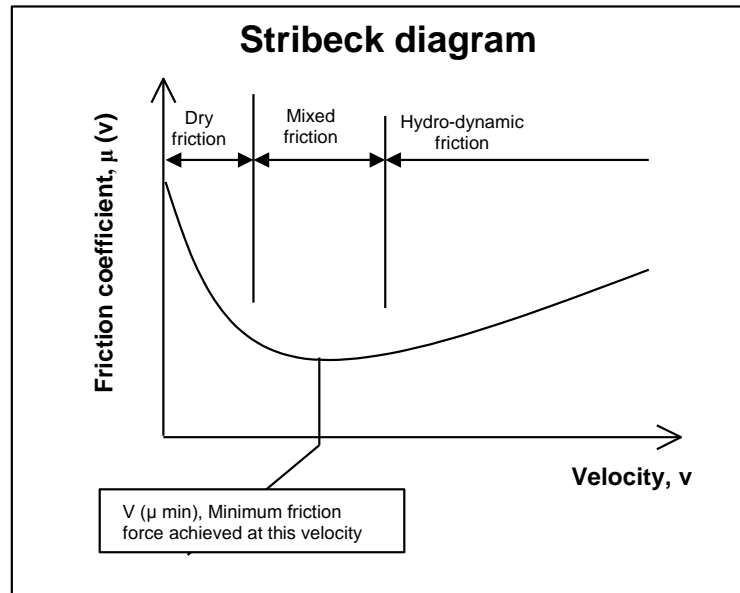


Figure 4.10: Stribeck diagram (Black, 2003)

Analytical equations describe the process, but are often highly inaccurate. Friction depends upon the application pressure, temperature, percent of squeeze, surface finish of the rod, seal type geometry, and material modulus. Due to this many parameters needed to be controlled, seal manufacturers use a non-linear FEA to help predict friction (Parker Fluid Power, 2007). In general, friction differences from O-rings is on the order of a magnitude less for glide rings.

The free body diagram of all the forces listed thus far can be seen in Figure 4.11.

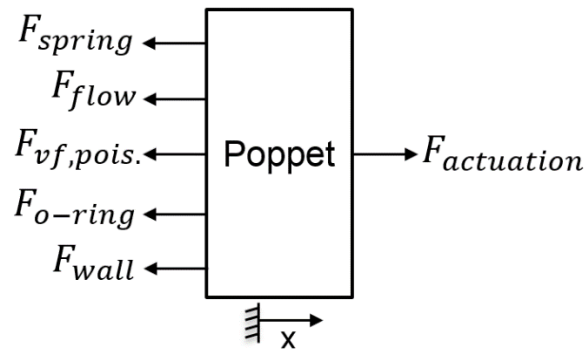


Figure 4.11: FBD for the ECAV

The free body diagram in the figure depicts the forces generated as the poppet valve opens. The actuation force must overcome all the other dissipative forces to fully actuate. The spring force helps aid the actuation force in closing the poppet.

The total motion of the ECAV is equated in Equation 4.29.

$$m \frac{d^2 x}{dt^2} = F_{actuation} - F_{spring} - F_{flow} - F_{oring} - F_{wall} \quad \text{Eq. 4.29}$$

With acceleration of the poppet now known, the velocity can be found.

$$\frac{dx}{dt} = \int \frac{d^2 x}{dt^2} dt \quad \text{Eq. 4.30}$$

From the solved velocity, position is found through the integral of it.

$$x = \int \frac{dx}{dt} dt \quad \text{Eq. 4.31}$$

4.5 Model Implementation

The initial model described the electromagnetic relationship converting the peak and hold voltage to a flux density inside the core of the actuator which ultimately generates a resultant shear force dependent upon a yield stress lookup table. Figure 4.12 shows this relationship in the Simulink model.

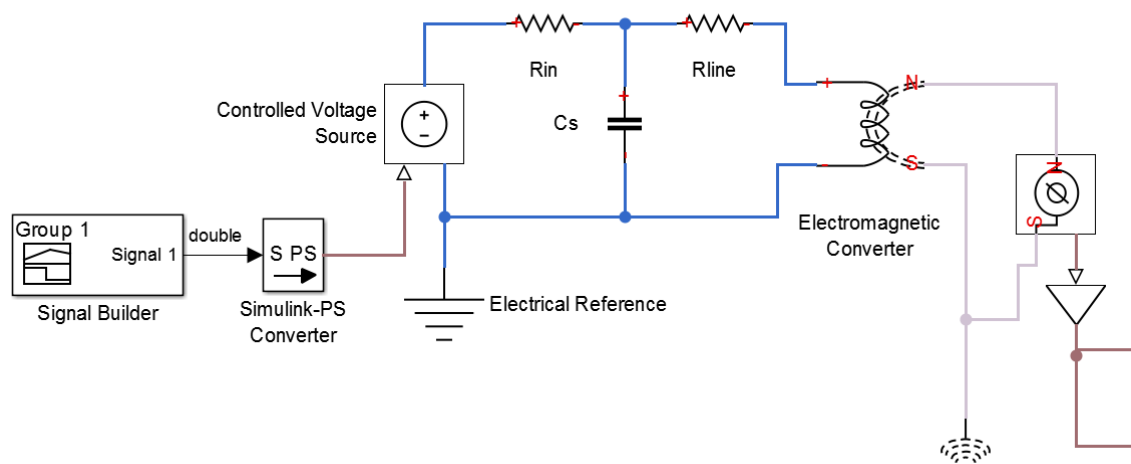


Figure 4.12: Peak and hold voltage signal to magnetic flux density

After the electromagnetic domain was finished, the mechanical and fluidic domains were set up. Since most of the equations in these domains depend upon the valve's geometry and operation parameters, the model was finalized after the ECAV was prototyped. The equations generated from this chapter served as a design tool for properly sizing the valve's geometry for high performance characteristics.

CHAPTER 5. PROTOTYPE ECAV DESIGN

After the initial model was created in Simulink, work began in PTC Creo to create a CAD model. The design hereinafter is iterative in that design choices based on simulation ultimately had to be made machinable while also sourcing components that were available to purchase from vendors. Manufacturability and ease of assembly were heavily weighted and drove the final design of the poppet valve and actuator assembly.

5.1 ECA Assembly

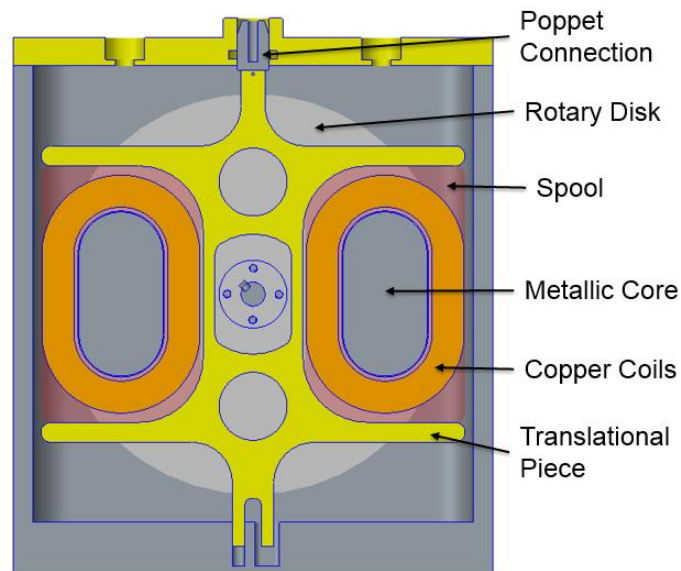


Figure 5.1: ECA box cross section

Figure 5.1 shows the sectioned view of the actuator assembly. The translational piece was updated from the prototype tested by Xiong and Skelton, 2014. The copper coils are wound around a 3D printed plastic spool with the ferrous core inserted into the center of the spool. The spools are then epoxied around the C opening of each side of the translational piece to hold in place. The translational piece is pinned to the poppet connector cylinder at the top and is installed in a false floor at the bottom of the assembly.

5.1.1 ECA Assembly Structural Analysis

5.1.1.1 Actuator Assembly

The false floor aids in reducing the bending moment acted upon the translational piece when the coils become energized. Figure 5.2 shows the resulting total deformation and equivalent stress when one coil is energized. The maximum actuation force (100N) was applied to the upper surface of one side of the coil set. The poppet connector and the floor fork were held as supports. The maximum deformation was found to be 0.005 mm at an equivalent stress of 25.4 MPa, well below the tensile strength of 6061 aluminum (270 MPa). The actuator transfers its reaction force through a pinned connection between the actuator and the spool or poppet valve. A coiled spring pin with a proof double shear strength of 400 N was selected, four times the force generated through actuation.

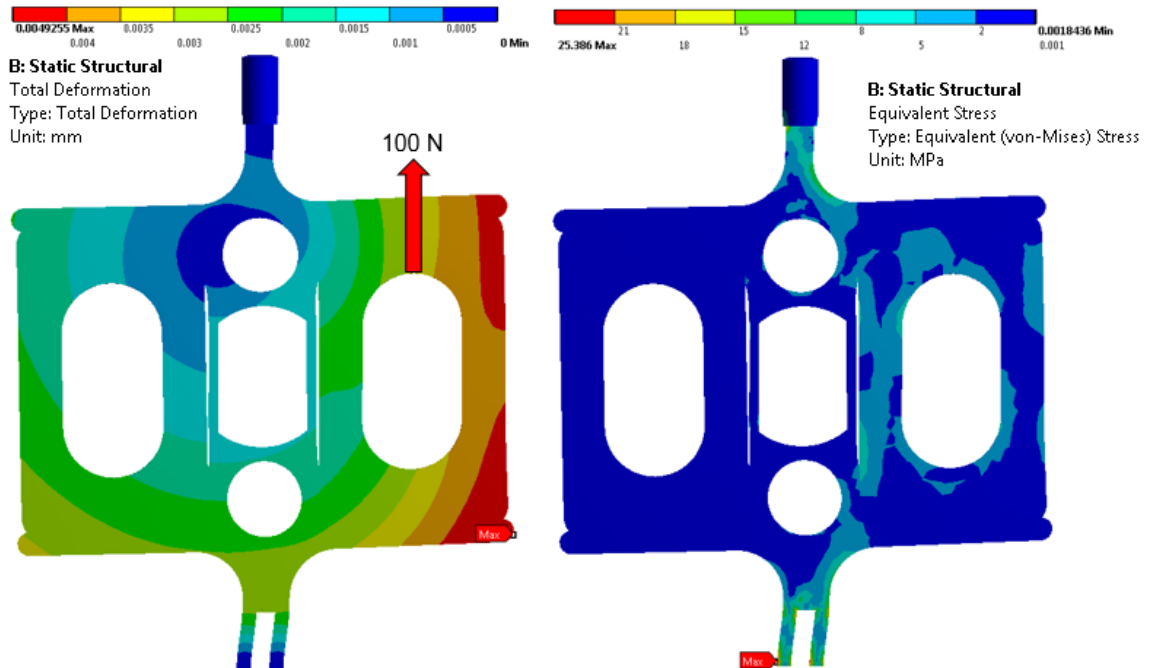


Figure 5.2 Structural FEA on the actuator assembly

5.1.1.2 Actuator Box Assembly

Figure 5.3 shows a side view of the components within the actuator box. The shaft must carry the load from the energy source and transmit it to the disk subassembly. The shaft undergoes a maximum torque of 12Nm and a maximum bending moment of 0.44Nm from the stepper motor driving it and the weight of the disk subassembly while no loads are applied in tension.

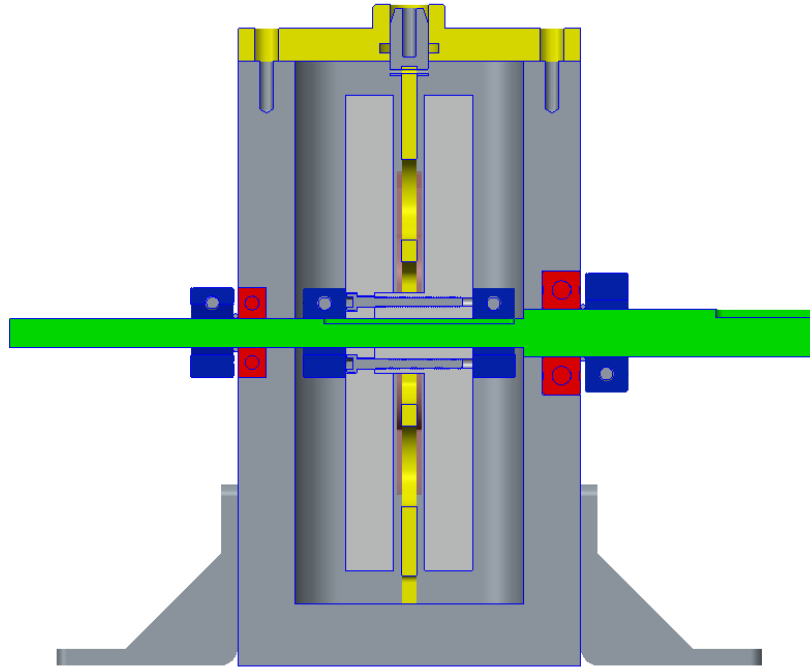


Figure 5.3: Actuator box assembly

The equation for finding stress due to a bending moment on the shaft is:

$$\sigma_{\max} = K_t \frac{32M}{\pi d^3} \quad \text{Eq. 5.1}$$

Where M is 0.44Nm, d is 0.006m, and K_t , the stress concentration factor for the stepped shaft, is 1.15. From this, σ_{\max} is found to be 35.7MPa.

Shear stress from torsion applied to the shaft is found from the equation:

$$\tau_{\max} = K_t \frac{16T}{\pi d^3} \quad \text{Eq. 5.2}$$

Where T is 12Nm, K_t is 1.15, and d is 6mm. the maximum torsion is solved to be 325MPa. The metric shaft selected has a yield stress of 115 ksi or 793 MPa, well above the max shear stress subjected to the shaft in this experiment.

The load from the shaft is transferred to the disk through a key on the shaft. The force on the key at the shaft surface, F , is:

$$F = \frac{T}{r} \quad \text{Eq. 5.3}$$

Where T is the torque on the shaft, and r is the radius of the shaft. From this, a force on the key is found to be 4,000N. To carry this load, the length required (L) for the key is (Krutz,199):

$$\tau_{all} = \frac{\sigma_{all}}{2} = \frac{3F}{2A} \quad \text{Eq. 5.4}$$

$$A = \frac{1}{4}L \quad \text{Eq. 5.5}$$

Where τ_{all} is the allowable shear stress on the shaft, A is the shear area. A minimum length of 8mm is required to carry the load generated by the power source. For an added factor of safety, the key was made to be the full length of the disk subassembly. The male and female disks are fastened together by four bolts.

5.2 Poppet Valve Assembly

5.2.1 Valve Block Design

Figure 5.4 depicts the sectioned view of the valve components inside the assembly.

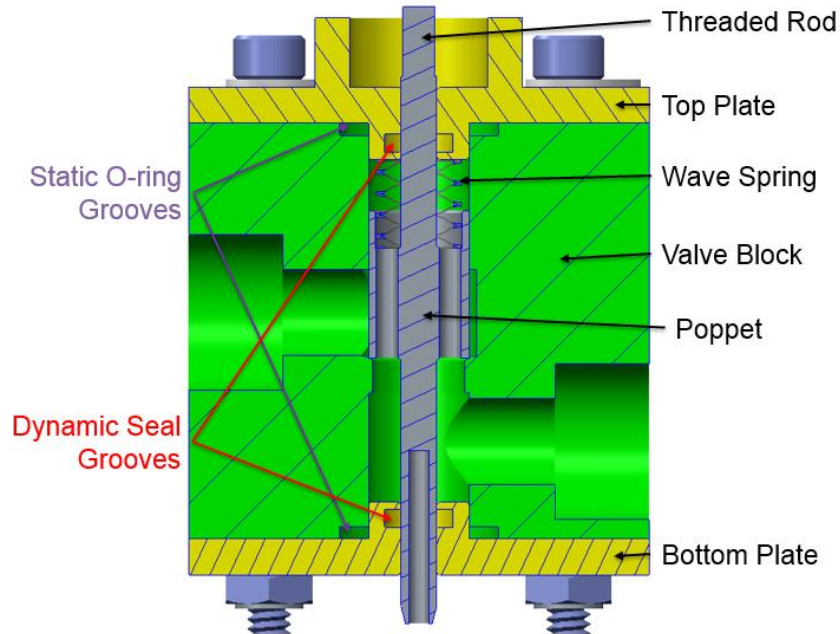


Figure 5.4: Cross section of valve block assembly

The components are assembled together with four bolts and aligned via the plate inserts into the valve body cavity. The spring installed on the poppet aids in positive poppet sealing when the poppet is closed. A wave spring was chosen to minimize the space required within the valve body volume. The Smalley wave spring CS037-L6 can compress 6 mm in its linear range, operates in a bore of 9.5 mm, clears a shaft diameter of 6.35mm, and generates a force of 17 N at work height, enough to overcome internal friction and the weight of the actuator. The leakage path between the valve block and plates is prevented through two static seal grooves that are sized for a Parker 2-015 O-ring. The next section goes into further detail on the dynamic seal design.

5.2.2 O-Ring Selection

In general, a piston groove O-ring generates more friction for the same O-ring size when compared to a rod groove O-ring due to the larger projected sealing area A_p . Since the ECA is separated from the valve body, a dynamic seal on the translational piece was necessary for implementation. An additional seal was needed to keep the poppet pressure balanced. Figure 5.5 depicts an early concept valve design and shows the locations of the two dynamic seals specified.

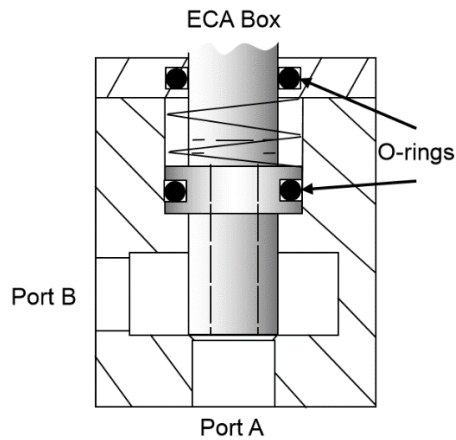


Figure 5.5: O-ring sealing locations

Both O-rings pictured here seal against high pressure hydraulic fluid while the top O-ring also acts to separate the MR fluid from the hydraulic oil. Pressure balancing is achieved with these O-rings as the area exposed to port A equals the spool rim area between the two O-rings that shares the same pressure at port A. The piston O-ring alone in Figure 5.5 created a large friction force from the sealing area, A_p . Parker O-ring size no. 2-015, a size that would fit the piston groove, generates a friction force of 30N at 100 bar. After implementing the friction forces in the ECAV model, it became apparent that a new

design was needed. Figure 5.6 shows the updated pressure balanced poppet with two small shafts exiting the valve body.

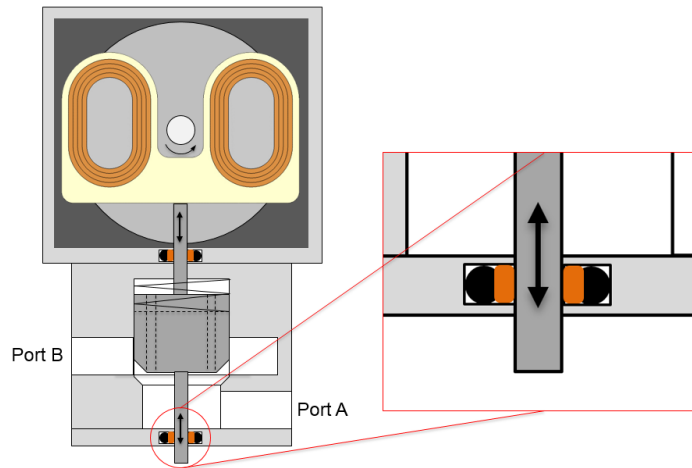


Figure 5.6: Updated sealing locations for the ECAV

In this updated design, the top shaft connects to the actuator assembly, while the bottom shaft exits the valve for measurement purposes that will be described in chapter 6. These rods were sized for the smallest dynamic O-rings available from Parker (no. 2-006) to get the most reduced friction. At 10 bar, the O-rings exert 15.2N of friction combined. At the maximum testable pressure (100 bar), the total friction equates to 25.3N. In an effort to reduce friction even more, slipper seal glide rings were added to the assembly. These can be seen between the O-ring and the poppet rod. Glide rings introduce less friction due to the PTFE material's coefficient of friction being less than rubber elastomer's coefficient of friction. In addition, the seal creates a wider contact area against the rod, distributing contact more evenly, depicted in Figure 5.7.

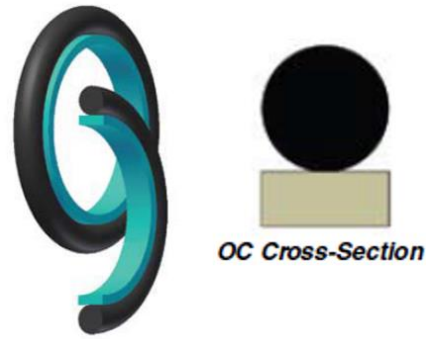


Figure 5.7: Parker OC rod seal with cross section (Parker Fluid Power, 2007)

Parker PTFE rod cap seal with an OC profile was chosen for the poppet valve rods. The operating range in terms of max surface speed, temperature and pressure ranges all correspond to the application of the ECAV and the max testable requirements on the test stand.

5.2.3 Valve Assembly Structural Analysis

5.2.3.1 Bolt Structural Calculation

Designing the bolts to safely hold a pressure of 350 bar indicates a corresponding force of 8500 N. A 10-24 socket head cap screw was chosen for the assembly. Screws of this size have a minimum tensile strength of 170,000 psi (1172 MPa) with a minor diameter area of 0.0146 in² (9.4mm²). The resulting load factor equation taken from Budynas and Nisbett (2008):

$$n_L = \frac{S_p A_t - F_i}{CP} \quad \text{Eq. 5.6}$$

where S_p is the proof strength, A_t is the tensile stress area (.0175 in²), F_i is the preload, C is the fraction of external load carried, and P is the external tensile load per bolt. The load

factor using one bolt alone is greater than one, proving four bolts would provide the adequate force necessary.

5.2.3.2 Finite Element Analysis

3D Structural FEA on the valve assembly solved for equivalent (von-Mises) stress and deformation. A max pressure of 35 MPa (350 bar) was set on the internal cavity surfaces that would be under pressure. Reaction forces from the actuator on the poppet and the poppet hitting the valve seat and upper valve plate were also implemented into the analysis. The maximum stress of 216 MPa occurs on the poppet chamfer. The poppet is made from 0.5” annealed 4140 steel rod with a yield strength of 417 MPa, while the valve block and plates are made from a 2”x2” square bar of 4140 steel with a yield strength of 655 MPa. Since the test stand can only reach 200 bar, it can be concluded that the valve will operate under the full range of experimental testing. Figure 5.8: Equivalent stress on valve assembly details maximum stress seen on the assembly

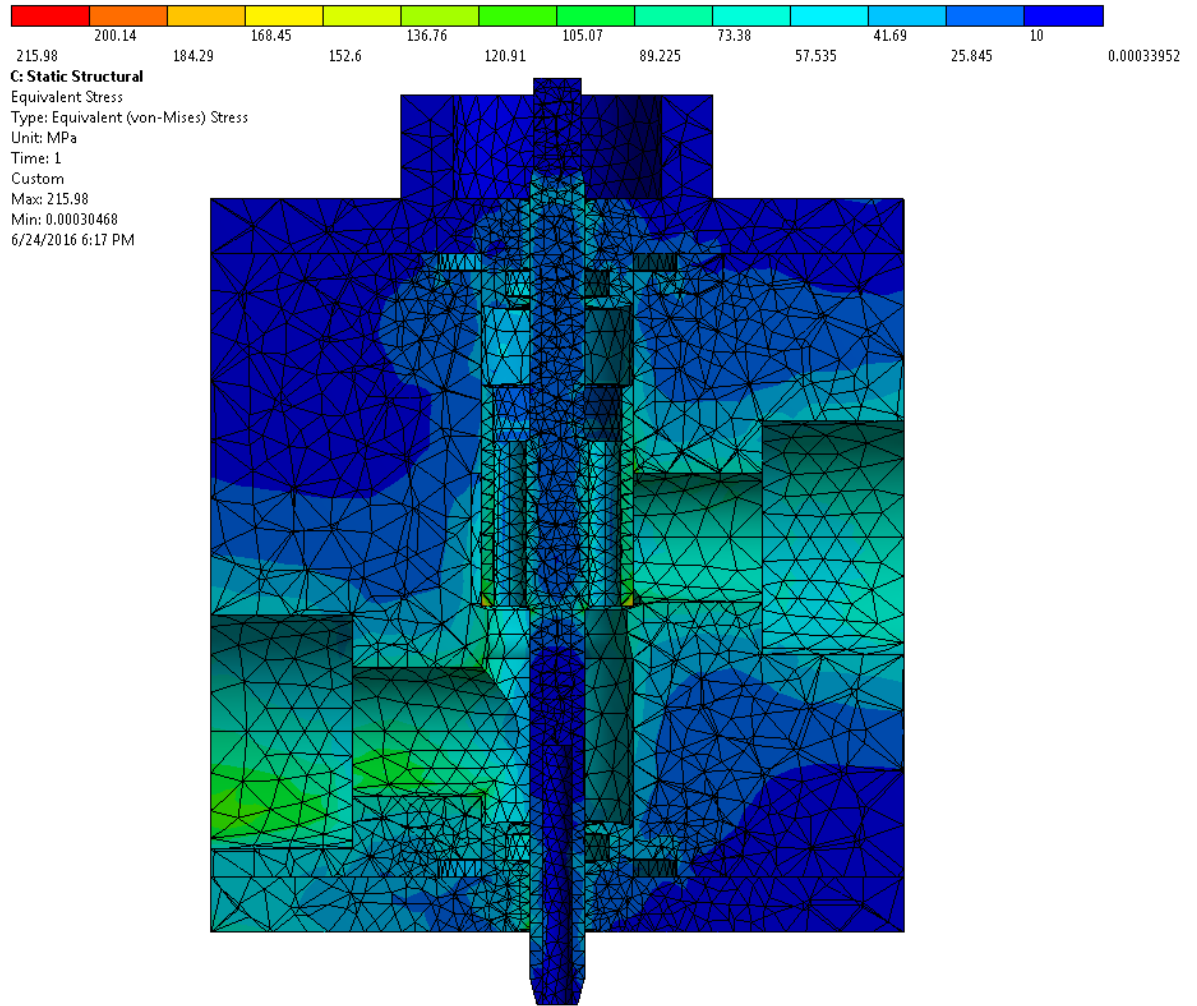


Figure 5.8: Equivalent stress on valve assembly

5.3 Machined ECAV Assembly

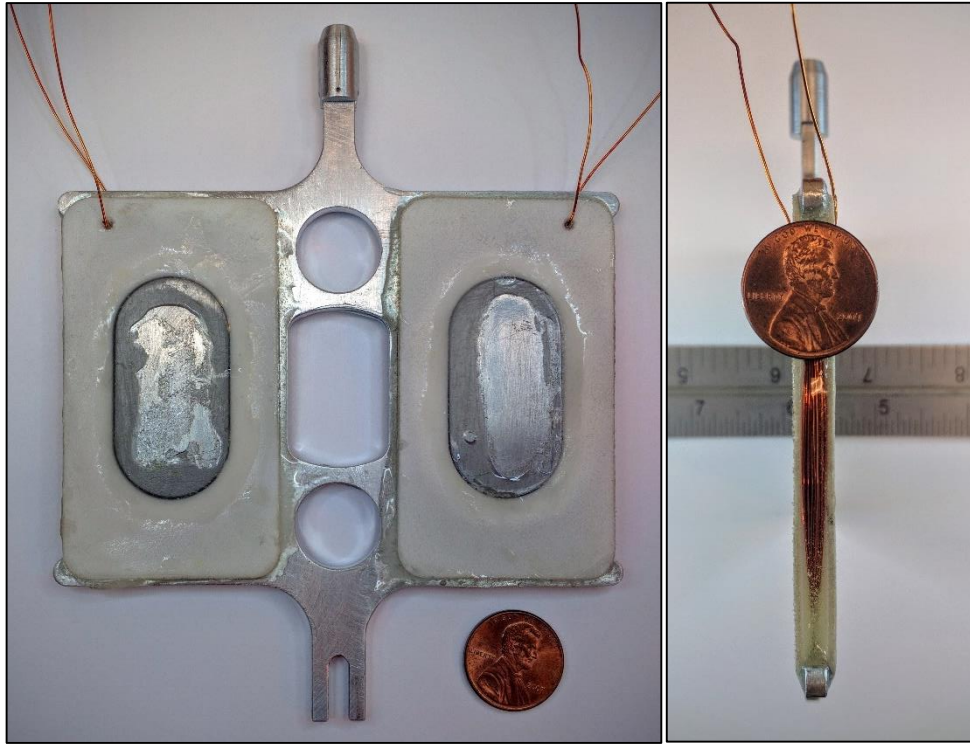


Figure 5.9: Actuator subassembly front and side

The actuator, pictured in Figure 5.9, was assembled by inserting the AISI 1008 steel core pieces followed with winding the PA 2200, 3D printed plastic spools with 26-gauge copper wire. The low carbon steel was selected for its strong magnetic permeability and the plastic material was selected for its relatively high tensile strength of 48 MPa (EOS GmbH, 2008). The coil sets are then epoxied to the aluminum frame of the actuator. Assembling with an adhesive over mechanical fasteners lowers the weight and distributes the stress across the entire bonded area. The actuator frame was machined from 1/8" (3.18mm) thick 6061 aluminum. The actuator cylinder was also machined from aluminum and pinned to the frame with a 0.031" (0.79mm) nominal diameter, alloy steel

standard duty coiled pin rated for a minimum double shear strength of 90lbs (400 N).

Table 5.1 displays the weight of each component on the actuator.

Table 5.1: Actuator component masses

Component	Mass/Each
Steel core (x2)	31g
Actuator aluminum frame	21g
Plastic wire spool (x2)	5g
Total (with copper wire, epoxy)	129g

The actuator box, seen in Figure 5.10 without the top plate installed, shows the box filled with MR fluid and the disk assembled and installed inside the box with the actuator inside its gap and the shaft attached to the stepper motor.

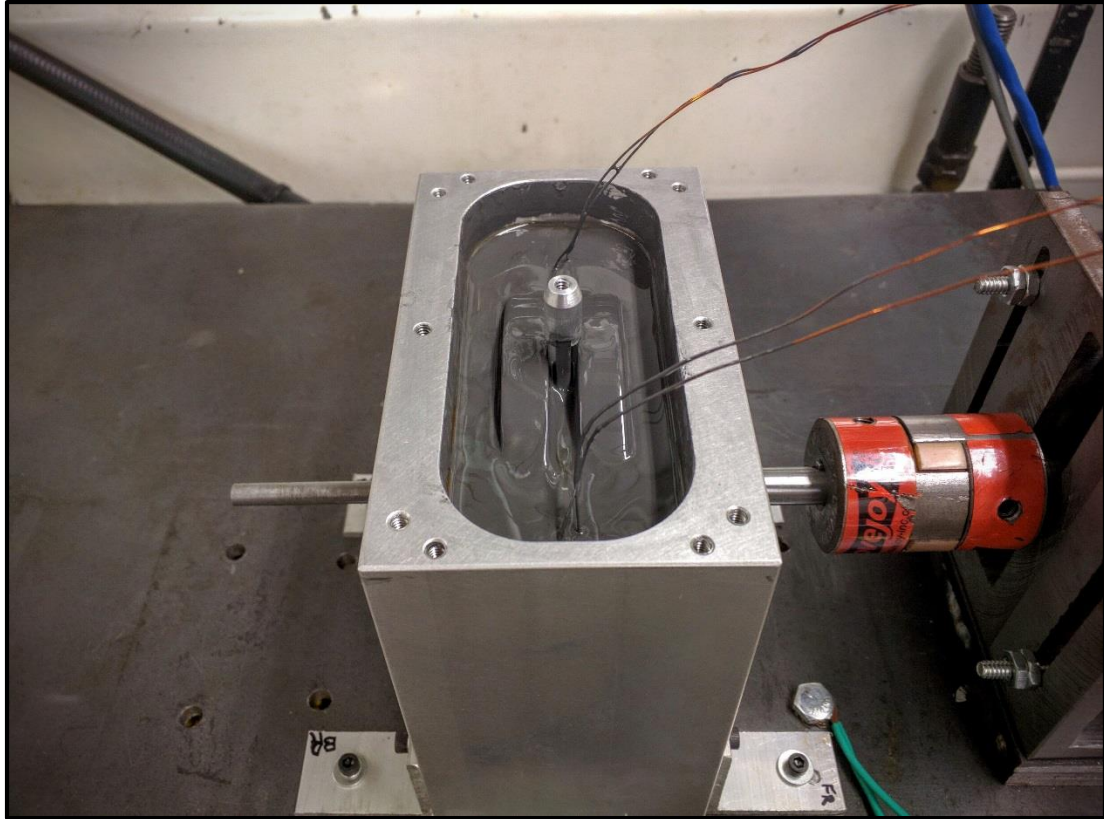


Figure 5.10: Actuator Box Subassembly

The box itself was machined from an aluminum block. Sealed bearings were press fit into the box and the stepped driveshaft was machined with a slip fit tolerance for ease of assembly. The 1045 carbon steel shaft is stepped from a 10mm turned, ground and polished bar stock to 6mm in diameter. Two keyways were cut into the shaft for the disk and shaft coupler. The 10mm side of the shaft connects to the flexible spider shaft coupler. Two O-rings installed on the outside of the box on the shaft with lock collars compressing them against the inner race of the sealed bearing prevents MR fluid from leaking across that interface. Additional lock collars were installed on the inside of the box on the shaft to lock the disk to the shaft and hold alignment with the false floor inside

the box for the actuator to slide in. This increased the width of the box for ease of assembly. The tapped holes on the top of the box allow for fastening brackets from both the poppet and spool valves to the box. The box plate, not pictured in the figure, aligns the top of the actuator with the spool and poppet threaded connection. Two rubber grommets are installed on the plate to allow the actuator copper coils to exit the subassembly and connect with the electric circuit. A rubber gasket was installed between the top of the actuator box and the box plate to prevent the splashing MR fluid from leaking between the two parts.

The poppet valve body, plates, and poppet are machined from AISI 4140 steel. The unbolted assembly with the poppet out of the valve cavity can be seen in Figure 5.11. The pressure balanced poppet is installed into the cavity first with the wave spring, followed by the valve plates over the poppet rods. Extra care is taken installing the top valve plate over the threaded rod portion so as to not damage the PTFE seals inside the valve plate, pictured in blue on the right figure in Figure 5.11. Pipe thread tape over the threads protects the seal from tearing. The 2-105 Parker static O-ring can also be seen on the right figure. This seals the internal valve cavity from atmospheric pressure when the four 10-28 bolts are installed on the assembly.

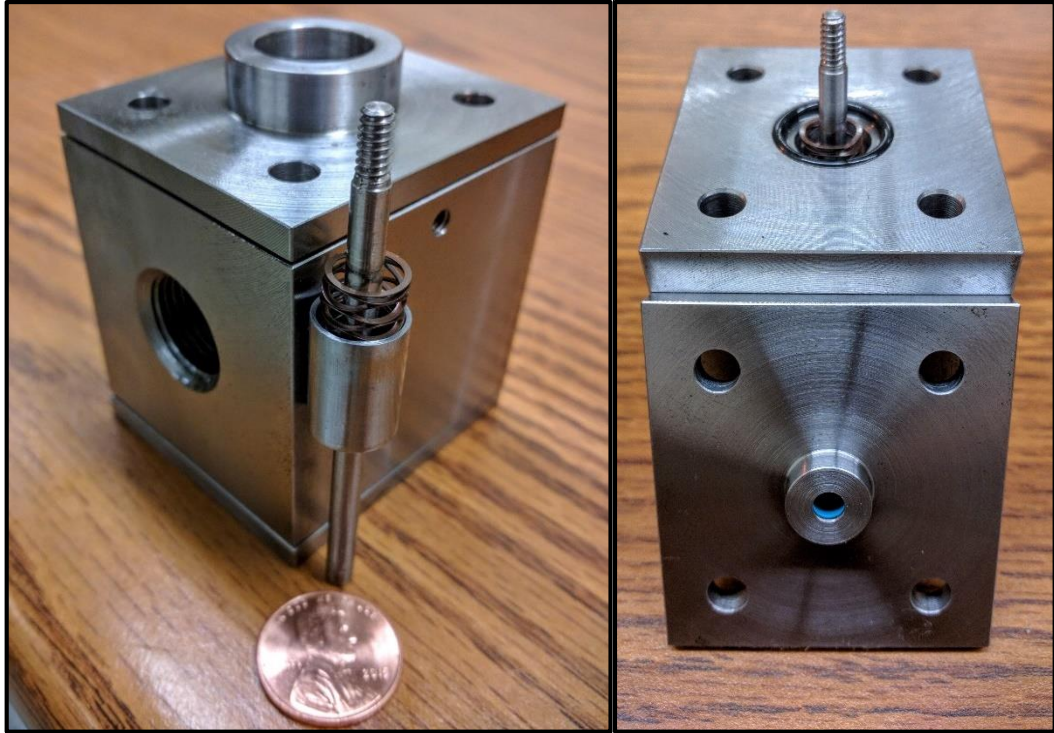


Figure 5.11: Poppet valve block subassembly

5.4 Spool Valve Assembly

A four way, three position, solenoid operated directional spool valve was supplied and modified by Sun Hydraulics. The solenoid assembly was removed where the solenoid pole piece attaches to the spool on the model DNDCXCN valve. Figure 5.12 details the piece removed.



Figure 5.12: Modified DNDC valve next to original model

The original push/pull rod that connects the spool valve to the solenoid pole was modified to fit the original ECA assembly. As pictured in the sectioned view, Figure 5.13, one end of the rod tightens to the actuator while the other attaches to the spool subassembly. A spring returns the spool to its normally closed position when the coils are powered off. The SAE-4 plug seals the internal valve cavity and an O-ring seals the outer diameter of the rod seal groove while a glide ring dynamically seals the rod from atmospheric pressure as it is installed between the O-ring inner diameter and the rod outer

diameter. Finally, the spool valve is aligned with the ECA through the alignment cylinder pictured in red.

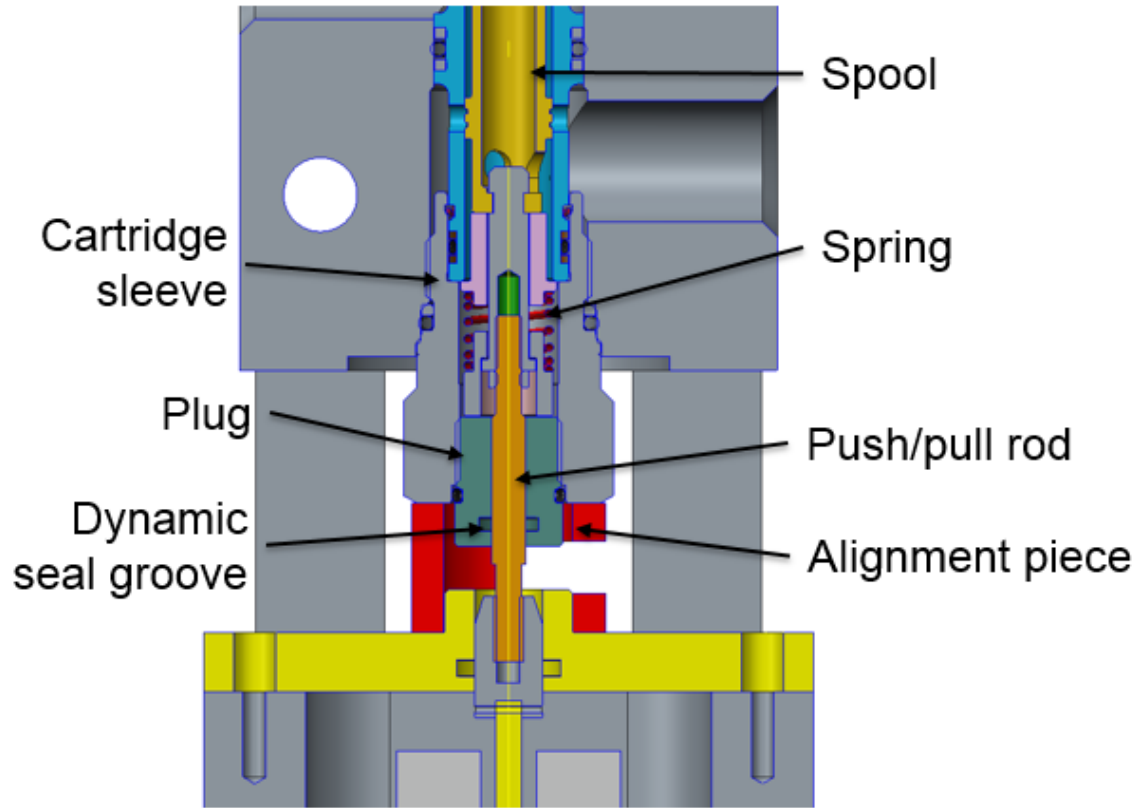


Figure 5.13: CAD model of spool valve modifications

CHAPTER 6. EXPERIMENTAL TESTING

Steady state and dynamic characteristics of the poppet and spool valve prototypes were tested experimentally. The experiments were carried out on a hydraulic test stand, and data was collected through a National Instruments data acquisition system. The software, VeriStand, was used to link the physical signals coming from the sensors on the test stand to the computer for data logging. VeriStand paired with a MATLAB Simulink model housed the calibration curves for the sensors and control for operating the actuation of each valve prototype. Lastly, results found through experiments were compared to the simulated performance.

6.1 Test Stand Components

A Parker Hannifin hydraulic test bench was used for the hydraulic power supply. A hydraulic gear pump supplies the flow for testing while an inline pressure relief valve limits the maximum pressure delivered in testing. Other primary hydraulic components are highlighted in Table 6.1.

Table 6.1: Test bench hydraulic components

Component	Specifications	Make/Model
Hydraulic Power Unit	Q_{max} : 33 l/min Motor: 7.5 kW p_{max} : 125 bar	Parker Hannifin H1 8.1NS3
Brazed Heat Exchanger	p_{max} : 31 bar T_{max} : 177°C	WCR Model 131008556
Filter	10 micron element	Parker Hannifin 12AT10C
Pressure Relief Valve	p_{max} : 206 bar at 38 l/min	Parker Hannifin RP600SF
Hoses	-40 to 93°C 10 mm (3/8 in) ID	Parker Hannifin
Hydraulic Fluid	ν : 32 cSt @ 40°C 5.4 cSt @ 100°C	Shell Tellus 32 506117

6.1.1 Sensors

Table 6.2 outlines all the sensors used on the test stand, along with the physical property being measured. Each sensor was calibrated and chosen for its rating, accuracy, and speed of data collection. Pressure sensors monitored the inlet and outlet ports of the poppet valve as well as the high pressure line and ports A and B on the spool valve. A laser was used to measure the current position of the poppet valve, and a temperature control unit maintained the hydraulic oil between 42-44 °C.

Table 6.2: Sensors used on the test stand

Property	Make	Model	Type	Rating	Accuracy	Speed
Pressure	Kistler	4260A	Piezo-resistive	-1-350 bar	$\pm 0.1\%$ FS	2000 Hz
Pressure	Wika	S-10	Strain gauge	207 bar	$\pm 0.25\%$ FS	1000 Hz
Flow	VSE	VS1	Positive Displacement	0.05 – 80 l/min	$\pm 0.3\%$	-
Differential Pressure	Honeywell	HL-Z	Strain Gauge Deflection	± 10 bar 172 bar line pressure	$\pm 0.25\%$ FS	3000 Hz
Position	Keyence	LK-G82	Semiconductor laser	± 15 mm	$\pm 0.05\%$ FS	2000 Hz
Temperature	Toho	TTM-J4	RTD Type K	-200-1372°C	$\pm 0.3\%$	2 Hz

A differential pressure transducer was used to measure flow generated through each valve dynamically. Both turbine and gear type flow meters are incapable of capturing transient flow rates due to their inherent inertia in the blades of the turbine and gears. The Honeywell HL-Z differential pressure transducer, seen in Figure 6.1, was modified to become an orifice flow meter. An orifice disk with an O-ring face seal is centered in-between the pressure sensors, and the unit measures the differential pressure across the orifice. The maximum pressure drop across the device is ± 10 bar, which limits the maximum flow rate across the orifice. Sizing the orifice correctly to reach max operating flow conditions on the test stand while utilizing the full pressure range of the sensor is

key for accurate flow measurement. One disadvantage of using an orifice meter is the inaccuracy measured at low flows. This effect is mitigated as this investigation deals primarily with capturing the valve characteristics under max flow conditions where flow forces heavily impact the dynamics of the valve. The hole in the orifice was sized to a diameter of 0.159in (4.04mm), drill size 21.

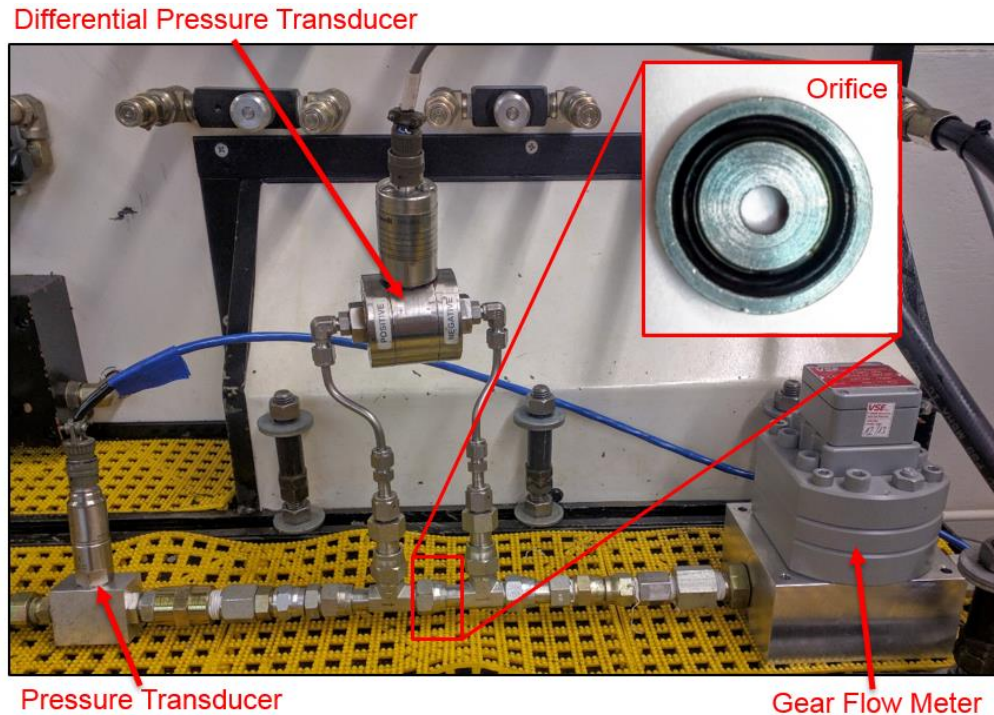


Figure 6.1: Calibrating the differential pressure transducer

The orifice flow meter was calibrated by steadily adjusting the gear flow meter in 1 L/min increments from 0 to 33 L/min. Inline pressure was recorded at each steady state flow condition, and the temperature of the hydraulic fluid was maintained at 43 °C. A PQ curve was generated, and a line of best fit was set up for the calibration.

6.2 NI Data Acquisition System

A National Instruments chassis, NI PXI-1031, houses the NI PXI-8108 controller and NI PXI-7813R reconfigurable I/O. The controller runs the Simulink model with the associated calibrations and valve control and records data at a rate of 5,000Hz. The VeriStand project screen, figure 6.2, allows the user to map the physical ports with the computer to record data, send commands to actuate the valve, and change experimental conditions like the forward and reverse peak and hold durations.

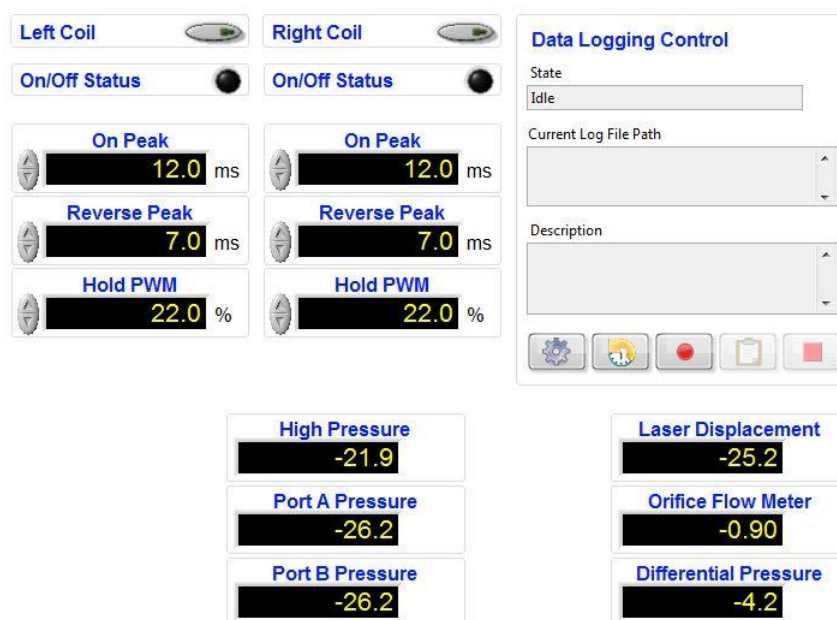


Figure 6.2: VeriStand user interface

6.3 Electric Circuit

An electric circuit was modified to carry out the experiments for the ECAV. The circuit requires the implementation of turning on and off (reverse current) peak and hold voltage strategies. An H-bridge was used to achieve both forward and reverse strategies. It can switch the polarity of the voltage and the direction of current in the circuit through the

use of four solid state switches. The voltage limit of the H-bridges on the circuit was 55V, limiting the maximum voltage testing to 55V at 3A of continuous current. An optocoupler isolates the high voltage for actuating the valves from the logic circuit. The input signal is inverted by the optocoupler, so a hex inverter is in the circuit to invert the signal back. Controlling the PWM and pin direction in the circuit effectively controlled the peak and hold duration time and for both forward and reverse signals.

6.4 Actuator Setup and Experimental Results

The actuator was tested alone first to establish a baseline for comparing the actuator with previous work, along with the poppet and spool valve results. The actuator by itself has no upper stop in place without a valve installed, so testing experimentally could only actuate the assembly in one direction to assure that the actuator never left the false floor supports. The actuator was lifted to a starting height by hand, then commanded to actuate downward. A stepper motor, powered from a motor driver, is controlled by tuning the frequency of a 5V signal from a signal generator. Figure 6.3 shows a typical response that was found from actuating the ECA at a disk rotation speed of 300-900RPM with a 12ms peak and hold voltage of 55V and 12V, respectively.

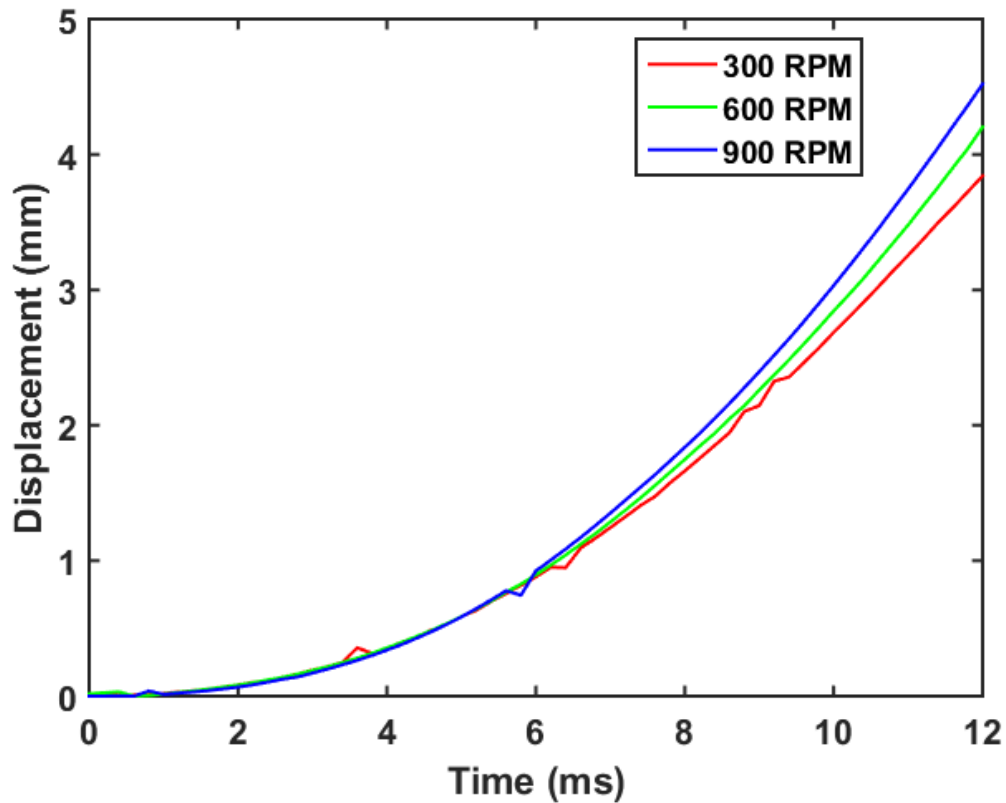


Figure 6.3: Displacement profile for one switch, 300RPM

Testing at higher disk speeds increased the displacement profiles but also generated a MR fluid leakage path, as the disk would begin to throw fluid out of the 3mm grommet hole that allows the ECA coils to exit the box. The 1.8ms delay was constant across experimental testing.

Testing the actuator alone increases the play of the pinned connection on the top of the actuator between the actuator frame and the actuator cylinder that would normally be threaded into the poppet or spool valve. As one of the coils becomes energized, the cylinder that is pinned to the now torqued actuator frame is free to rotate slightly

sideways around the pin and increases sliding friction as the assembly moves. While this test has the added benefit of no valve friction or added mass to the actuator from the valve assembly, one would expect slightly faster actuation response curves once the top of the actuator is fully supported.

6.5 Poppet Valve Setup and Experimental Results

Figure 6.4 lays out the hydraulic schematic for testing the poppet valve attached to the actuator. Flow from the fixed displacement gear pump was controlled with a variable orifice needle valve. System pressure was set through the pressure relief valve on the test stand. Pressure was recorded at both ports on the poppet valve, and flow was dynamically measured through the orifice meter.

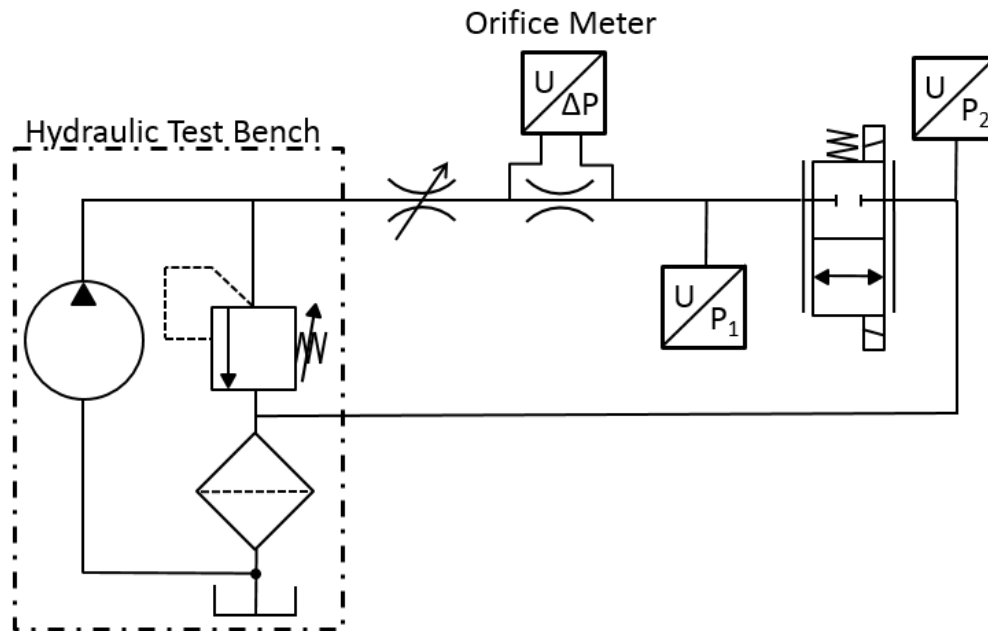


Figure 6.4: Poppet valve hydraulic test circuit

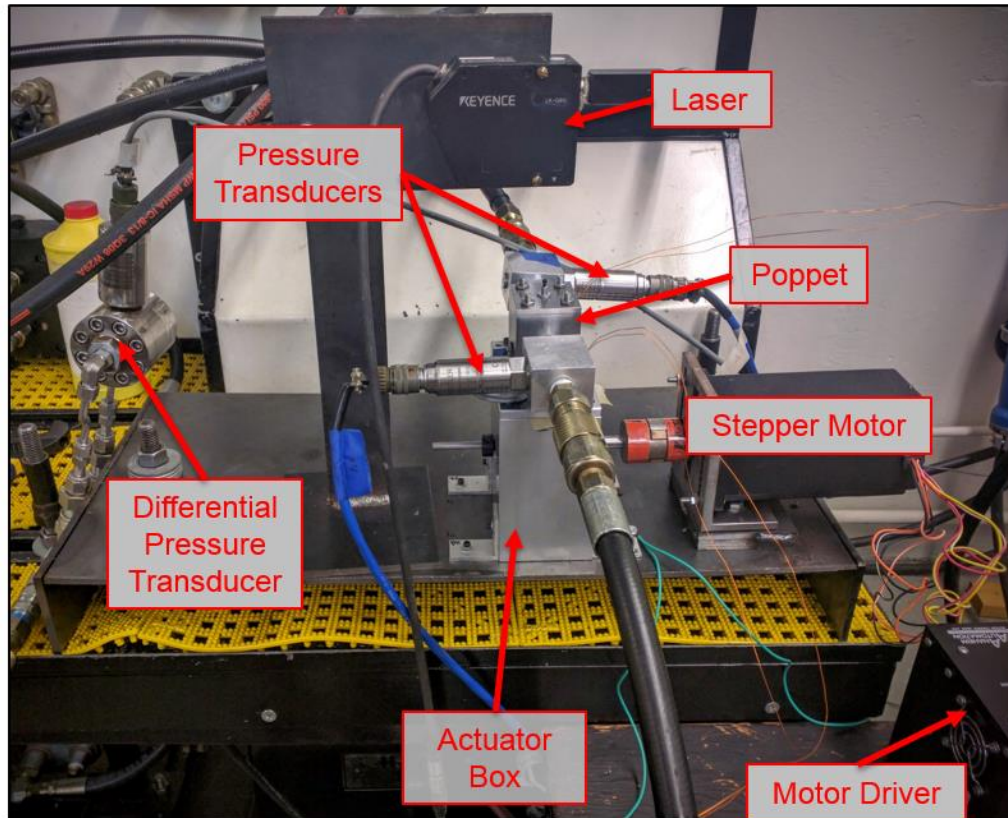


Figure 6.5: Poppet valve test stand

Figure 6.5 depicts the test set up for the poppet valve. The poppet valve block threads into the actuator box and is secured through two brackets on both sides of the valve block. The poppet valve was assembled to actuate only 4 of the 5.6mm total displacement to ensure adequate clearance after tolerance stack up between the valve subassembly and the actuator subassembly. The pressure transducers are on either immediate side of the poppet valve to more accurately measure the pressure drop across the valve by minimizing the pressure drop across hydraulic fittings. The laser positioned directly above the poppet valve records position displacement from the rod of the poppet exiting

the valve block. Bidirectional flow was tested on the poppet valve; Figure 6.6 shows the flow path directions under investigation.

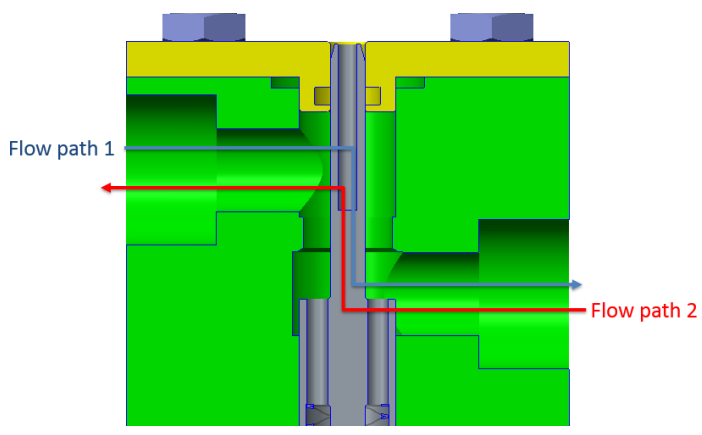


Figure 6.6: Flow paths through the poppet valve

Steady state pressure-flow performance was characterized first. The valve was held open at 5.6mm displacement as the flow rate was incrementally increased in 1L/min intervals and the pressure was recorded for each interval. Figure 6.7 details the experimental results found in testing to max test stand flow (left) and extrapolation to 100 L/min flow with the corresponding pressure drop (right).

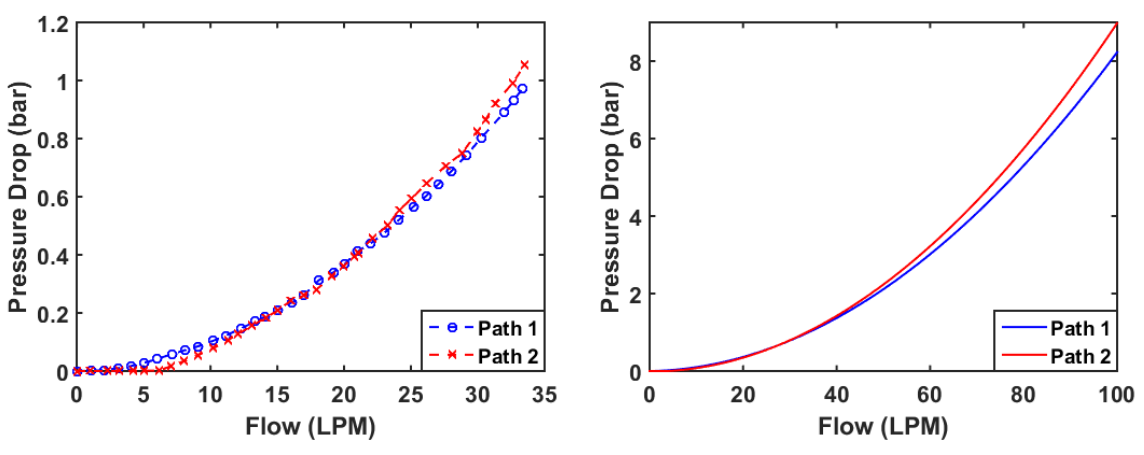


Figure 6.7: Pressure drop versus flow of the poppet valve

Results found experimentally that the pressure drop across the valve is 0.97bar and 1.05bar for flow paths 1 and 2, respectively, at 33L/min flow rate. After generating a second order polynomial best fit line from the experimental results, the pressure drop at 100L/min is 8.23 and 8.98 bar respectively. This value was found to be 3 to 4 bar higher than anticipated from the goal of generating 100L/min flow rate at a 5bar Δp . Additional pressure drop was created across the valve when the design of the poppet changed to a dual rod layout. With this design, the maximum flow area ($\sim 75\text{mm}^2$) is achieved after the poppet exceeds 2.2mm of displacement. After this displacement, the flow area between the poppet rod and the valve block seat becomes the limiting area.

6.5.1 Dynamic Poppet Experimental Results

In order to effectively compare the results across the poppet valve dynamic studies, a set of controls were put in place under the following conditions:

- Electrical circuit controls
 - Peak voltage: 55V
 - Holding voltage: 12V
 - Peak Duration: 6ms, 8ms, 12ms, 14ms
 - Shaft rotation speed: 300RPM
- Hydraulic circuit controls
 - Flow Rate: 33 L/min, (maximum supplied by test stand)
 - Pressure drop: 500 psi (34 bar)

Tests on the poppet valve were carried out by lengthening the amount of time peaking the voltage signal. The first set of tests were at a 6ms peak duration of 55V. Figure 6.8 shows

a typical response curve at 6ms peaking. In this test the poppet was actuated on/off twice. The peak and hold coil signal commands on the actuator are plotted with the measured displacement for comparison. The complete duration of the signal being sent is dependent upon the user clicking the button in VeriStand. With the disk spinning in the counterclockwise direction at 300RPM, the right coil signal energizes the right coil on the actuator and lifts the valve from 0mm to 4mm stroke. Conversely, the left coil signal closes the valve from 4mm to 0mm. The top graph in the figure shows the two on/off profiles that were recorded. The bottom two graphs are zoomed in response curves for the first on/off actuation response. The right coil signal, (bottom left graph), actuates the valve to 4mm in a 221ms response time with a 209.6ms delay. The time spent transitioning was 11.4ms. The left coil signal, (bottom right graph), actuated the poppet back to 0mm in a total response time of 25.2ms with a 4ms delay. The time spent transitioning was 21.2ms.

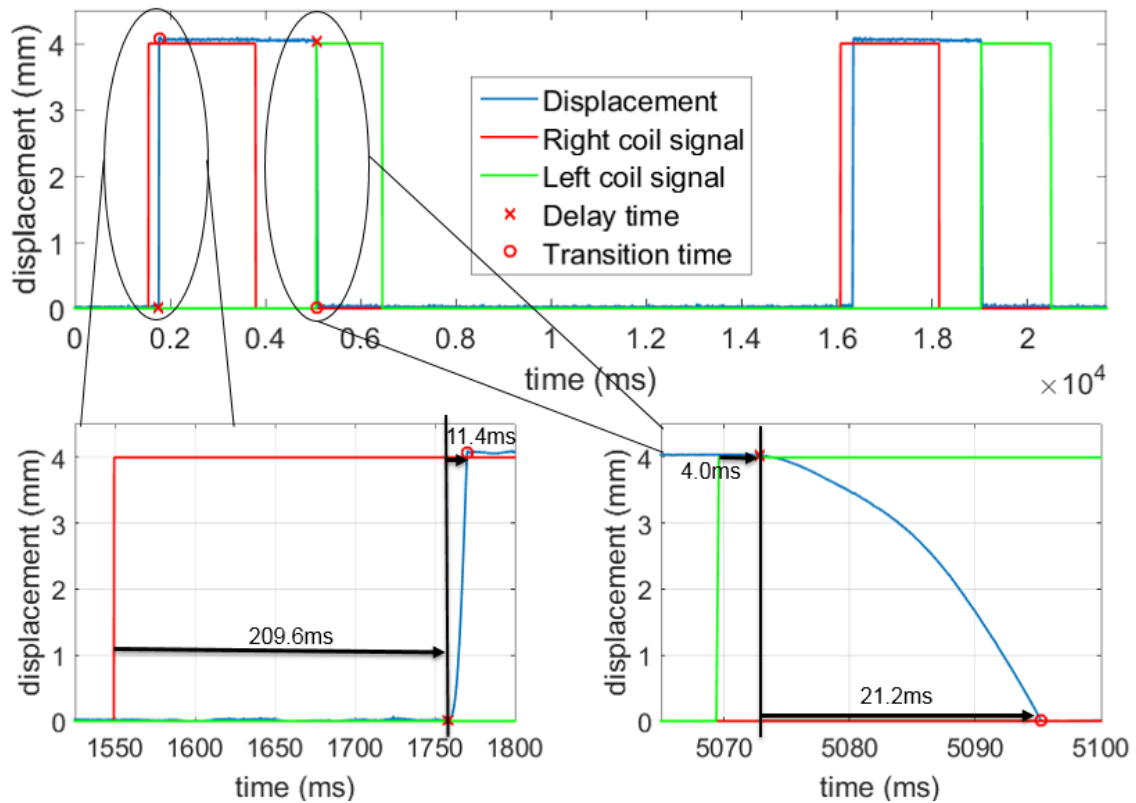


Figure 6.8: Displacement on/off profile

This actuation test, along with other results at 6ms peaking were considerably slow in actuation response time. Increasing the time spent peaking the coil sets along with reducing system friction was investigated. The weight of the sensors and hydraulic hoses on the valve block was enough to slightly misalign the poppet with the actuator, so shims were added between the valve block and actuator box to properly align the two subassemblies.

Figure 6.9 details a typical dynamic test found experimentally at a 12ms peak voltage time after shims were added. In the first plot, the poppet is actuated on/off twice. Figure

6.10 goes into more detail on this. After the coil signal is turned off, the valve continues to stay in the corresponding position. This is from a mix of friction in the system as well as some residual magnetism. The valve is able to open against the maximum flow testable (33L/min) at a system set pressure of 500psi (34.5bar). From the flow graph, there is an average of 3.2 L/min flow rate that occurs after the valve is closed. This is from leakage around the spool sealing area between the poppet outer wall and valve block interface. Hydraulic fluid flows through the pressure balancing holes inside the poppet and out around the poppet wall. The outer diameter of the poppet was machined to fit the valve block cavity, and the clearance tolerance around the diameter was not fully held when machined.

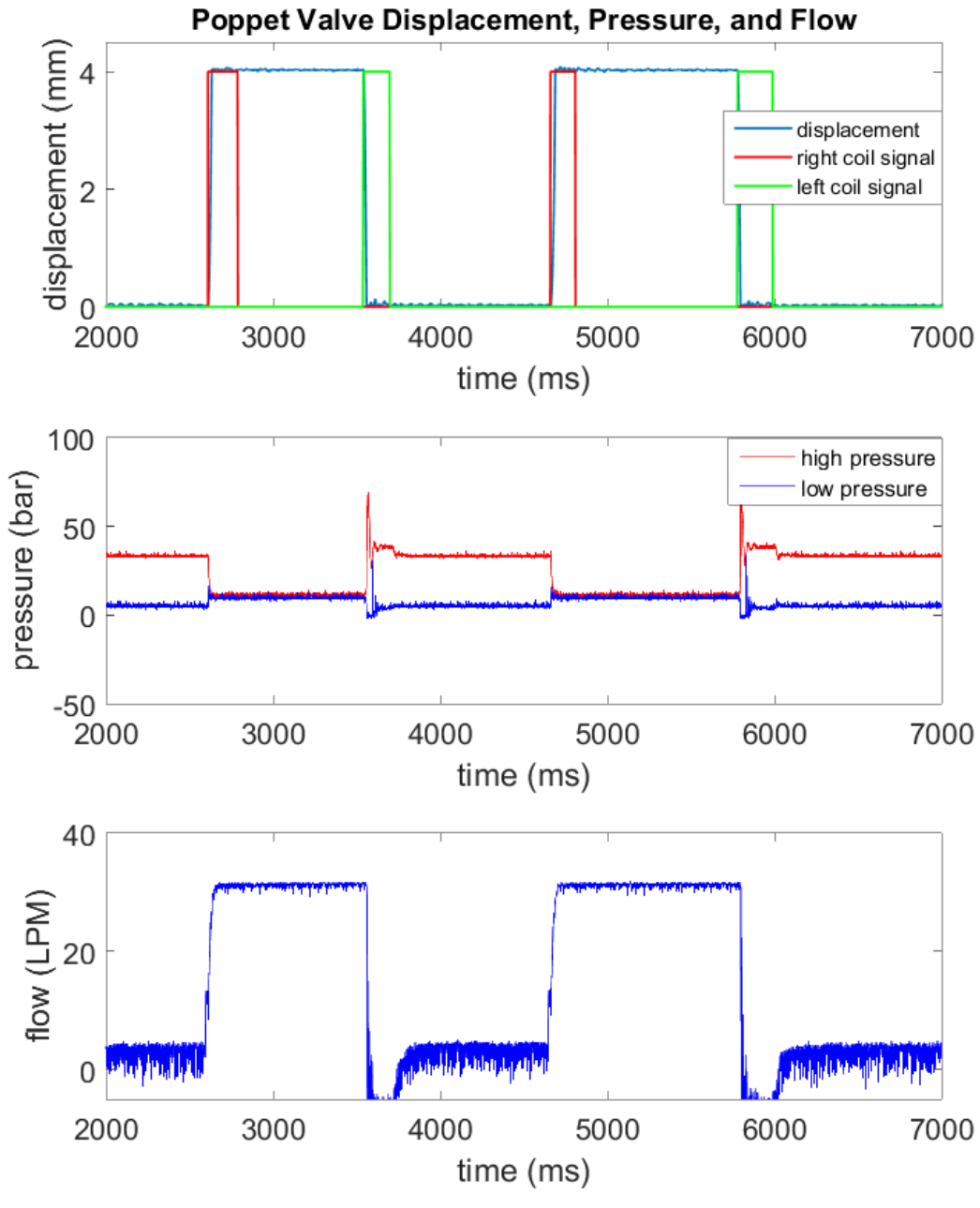


Figure 6.9: Poppet valve dynamic experimental results

Figure 6.10 visually shows a zoomed in, single on/off response time for the poppet valve. The bottom left figure shows the total on response time is 22.4ms. The delay in turning on is 2.6ms, making the transition time 19.8ms from 0 to 4mm displacement. The bottom

right figure shows the off response time of 19.8ms. The delay is 2.8ms with a transition time of 17ms.

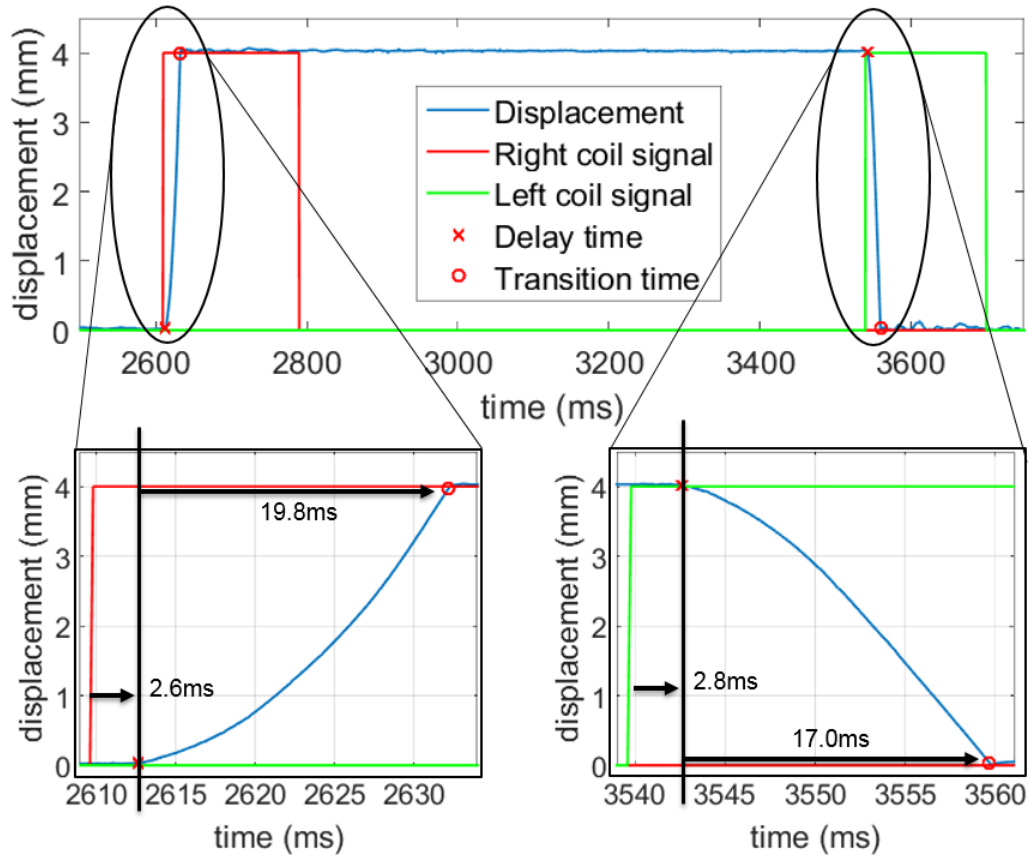


Figure 6.10: Dynamic displacement profile

The off response time across the 12ms peak voltage signal was found to be 2-3ms on average faster in total response time. As the poppet closes, flow forces and the installed spring assist the direction of movement. Overall valve response time had a positive correlation with increased peak voltage duration up until 12ms. After that the response times didn't improve significantly.

6.6 Comparison with Simulation Performance

Figure 6.11, below compares the simulated displacement of the poppet valve with the experimental results generated in the turn on response time from Figure 6.10. A lookup table of flow forces for a 34.5 bar pressure drop across the valve was implemented into the model to depict the same pressure drop as what was tested experimentally. The simulated performance predicts a 4mm displacement in 7.9ms when the actual resulted in 22.4ms.

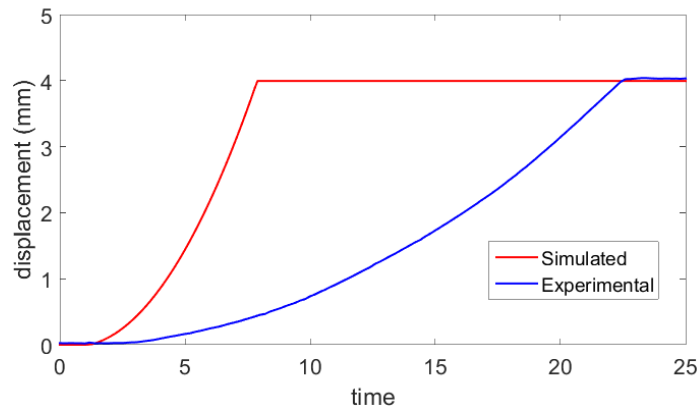


Figure 6.11: Simulated versus experimental results

The model in Simulink takes several assumptions into account ranging from average flux density inside the metallic cores of the actuator to a perfectly pressure balanced poppet. Tolerances in machining and misalignment in assembly added friction to the poppet valve that wasn't accounted for in the model. Sealing friction on the prototype was greatly increased as one of the rod glands for the O-ring and glide ring assembly was .013" (0.33mm) smaller than tolerance adding almost 20% more squeeze on the rod. The flow force lookup table that heavily impacts the dynamics of the valve has several assumptions of its own ranging from downstream chamber size to the jet angle formation of the fluid

and when it separates from the poppet. As a general conclusion, a poppet valve that is machined to a higher tolerance and assembled to the actuator as one piece, perhaps in a press-fit cartridge, would remove the chance of misalignment with the actuator and would greatly impact the performance of the poppet valve.

6.7 Spool Valve Setup and Experimental Results

The hydraulic schematic for the 4-way 3-position spool valve tests can be seen in Figure 6.12. Three pressure sensors measured the high pressure port, along with ports A and B. A variable orifice needle valve is placed between ports A and B to simulate a load on the valve. The orifice meter measured the flow rate through the spool valve, and an accumulator was added onto the circuit to filter the pressure ripple from the fixed displacement gear pump on the test bench.

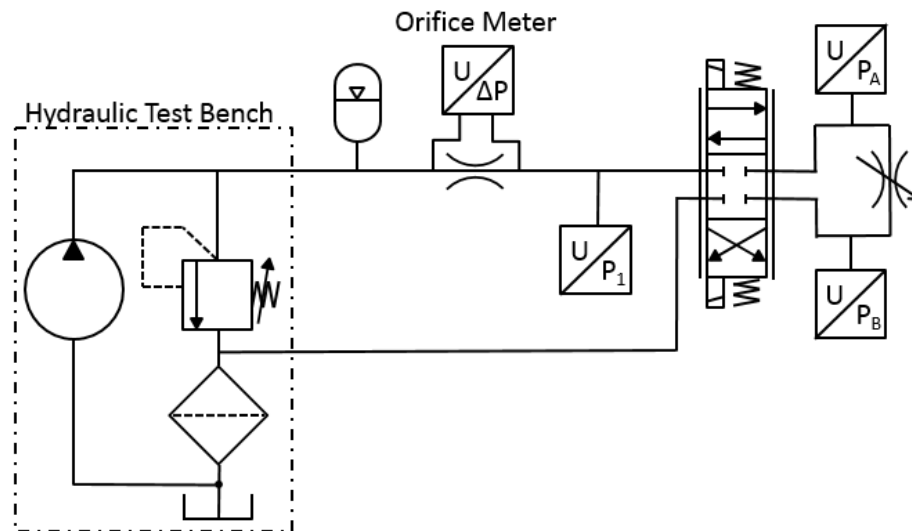


Figure 6.12: Spool valve hydraulic test circuit

The test stand components are shown in Figure 6.13. The modified cartridge spool valve threads into the actuator box assembly and is fastened to the box through four brackets. Quick connect hoses were routed to the valve manifold to complete the circuit. Like the poppet valve, the pressure transducers were assembled as close to the manifold ports as possible to minimize the pressure drop recorded across the valve.

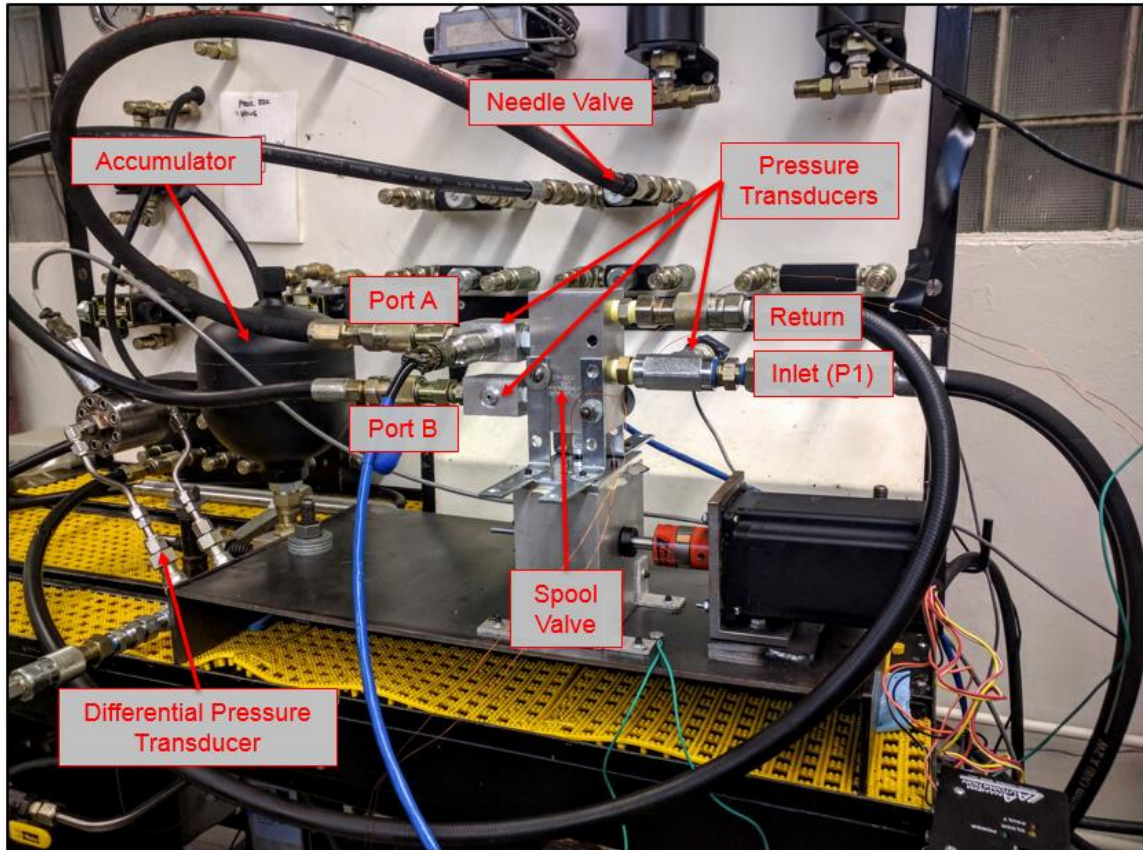


Figure 6.13: Spool valve test stand

Investigation into the spool valve's response time was done initially under steady state conditions, followed by dynamic experiments. Steady state tests were carried out by pressurizing the system while the spool was in its closed state, followed by a command signal to open the valve and divert flow to either port A or B. This result is generated

from a control for zero residual magnetism in the system, as tests were conducted solely in a one direction response. After the command was sent, the pressure drop across ports A and B was calculated, and from that, total delay and transition times were determined. The delay in the valve is estimated by the duration of time it takes from the signal being sent to a 10% decrease in the total magnitude of pressure drop across the working ports A and B. The high and low pressures that make up the total pressure drop are taken from steady state conditions. The amount of time it takes from 10% to 90% of difference in pressure drop is estimated to be the transition time. Estimating delay and transition timing this way gives a consistent result and has been seen in literature as a way to accurately describe response in instances of overshoot-settling conditions (Breidi et al., 2014).

Figure 6.14 details the results from a 12ms peak and hold, 300rpm disk speed test opening the valve to position 3, connecting port B to high pressure and routing port A to tank. This graph was generated early in testing before the accumulator was added to the system to filter the high pressure line. With an average pressure drop across the ports being 6.9 bar, the delay and transition time were calculated for times when the pressure drop reached .69 bar and 6.2 bar respectively. The delay time was calculated to be 1.8ms and the transition time was 1.4ms. With that small of a pressure drop, max flow from the test stand was not reached. To test the capabilities at larger flow rates, the pressure drop between the ports was raised and an accumulator was added to help filter pressure spikes in the circuit to get a more accurate flow measurement from the orifice flow meter.

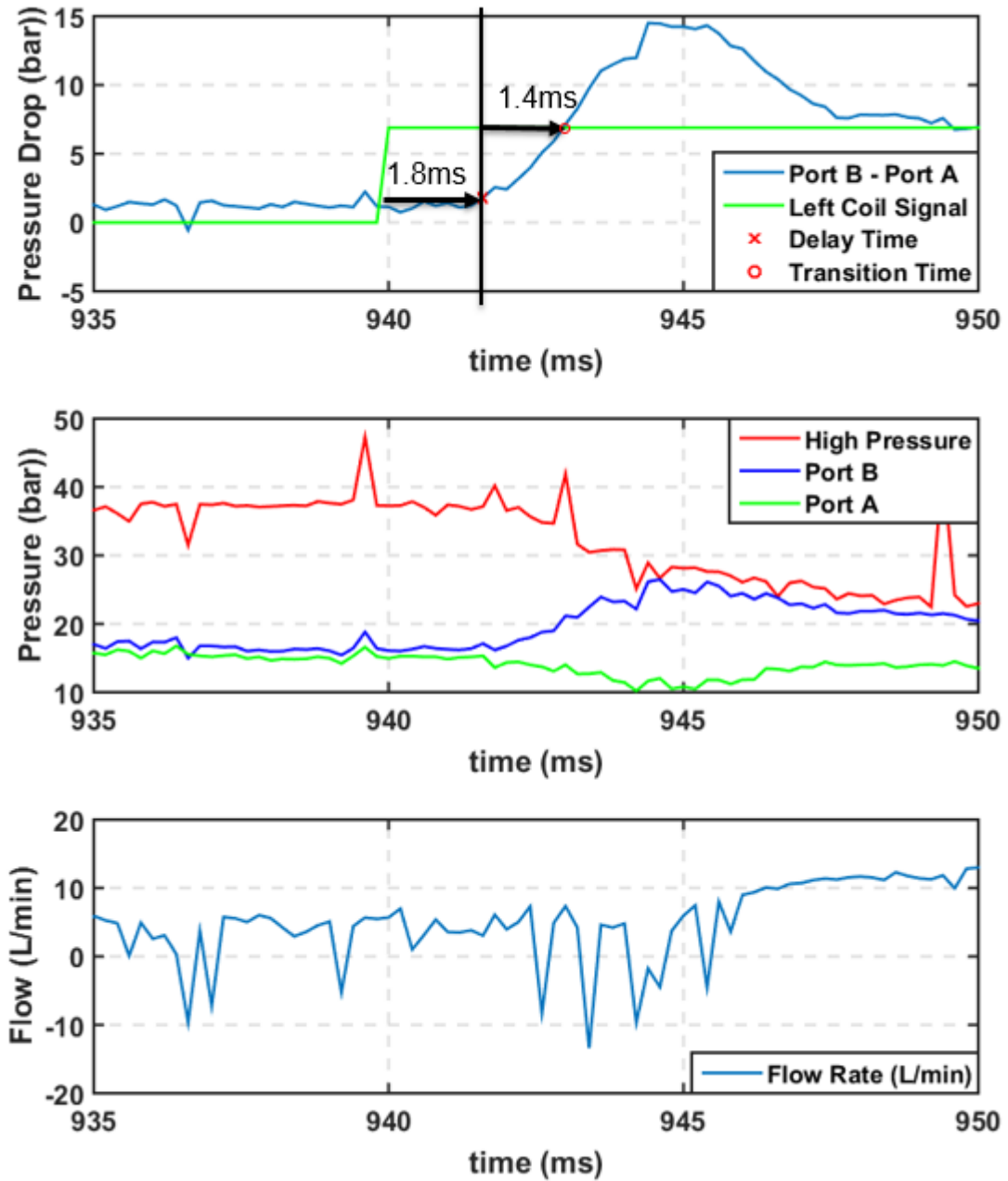


Figure 6.14: Step response (port B with high)

Figure 6.15 depicts the step response from closed to position 1, when port A is connected to the high pressure line and B is routed to tank. With an averaged overall pressure drop

of 20.7 bar, the delay time is found when the pressure drop reaches 2.07 bar and the transition time is at 18.6 bar. The results found that the delay time was consistent with the poppet valve results at 2.6ms; however, the transition time was reached faster in 2.2ms. This equates to a 4.8ms total response time switching the spool valve from its closed position to connect the high pressure port with port A.

A step response measurement was conducted to see the effect of residual magnetism on the actuator's response. After testing dynamically, the spool was quickly set back to closed centered position by hand and commanded to actuate to position 1, (port A with high pressure). Figure 6.16 shows the results found. As expected, the delay was increased considerably in reaching 10% of total pressure drop. The total delay was 7.6ms with a transitional time of 0.8ms. This gives a benchmark for comparing dynamic tests that will have residual magnetism on the coil that is not turned on.

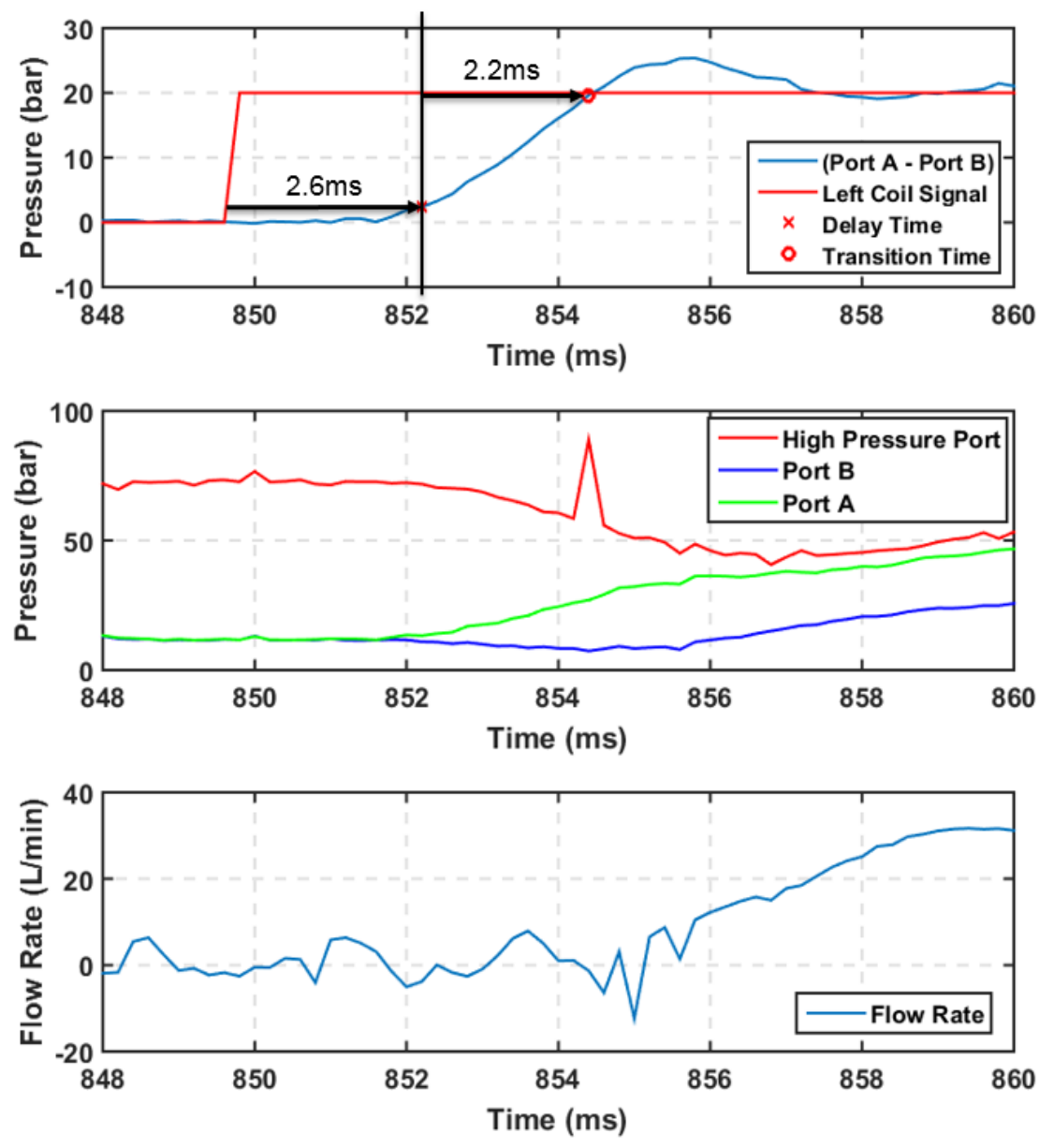


Figure 6.15: Step response (port A with high)

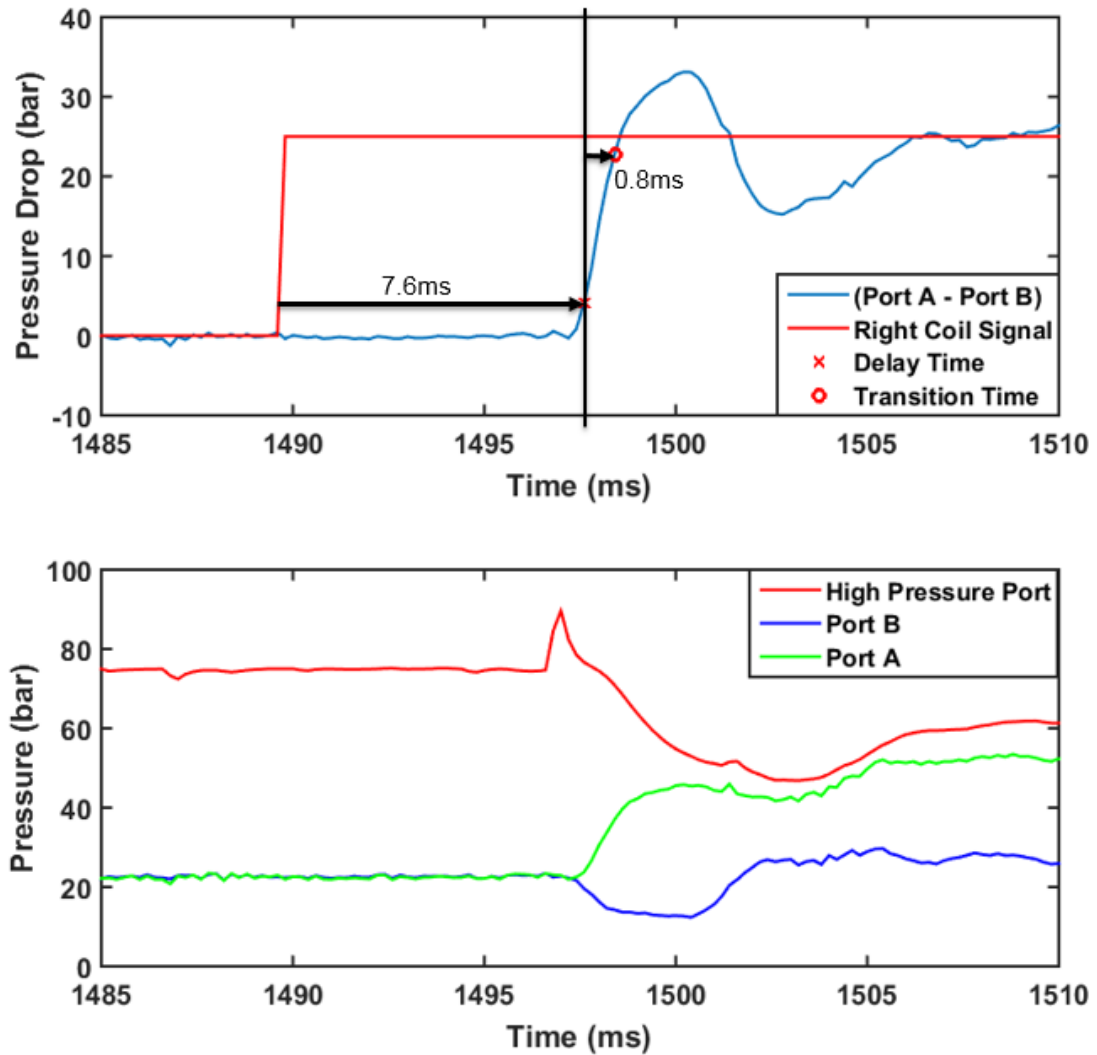


Figure 6.16: Step response to position 1 with residual magnetism

6.7.1 Dynamic Spool Experimental Results

After the step response from closed centered position was found for the spool valve, the dynamic movement of the spool valve was investigated. The coil command signals switched the position of the 4 way, 3 position spool valve from the high pressure port to

both ports A and B. The commanded signal was able to alternate the spool from position 1 to position 3 and back again. This can be seen in Figure 6.17.

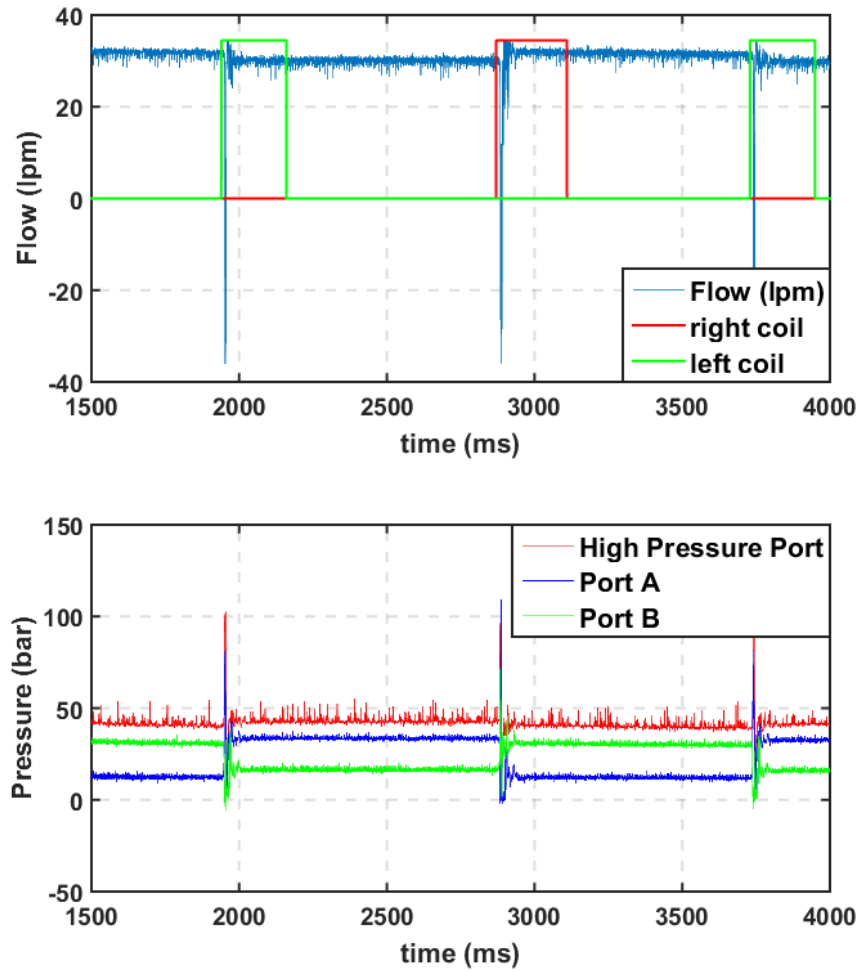


Figure 6.17: Alternating flow directions on the spool valve

At first, port A is connected with the high pressure port, and the test stand is providing max flow. At time 1.94s (1940ms), the left coil signal is commanded to actuate the spool, and the flow path is reversed to connect the high pressure port with port B, switching port A to tank. With the orifice flow meter installed on the high pressure line, the flow rate

recorded dropped near 0 before rising again to the max flow rate supplied by the gear pump on the test stand. The measured flow rate is always positive as it is positioned directly before the valve. If it were in-between the working port's A and B, the flow rate would be recorded from -33 to 33 L/min. An illustration of this is shown in Figure 6.18.

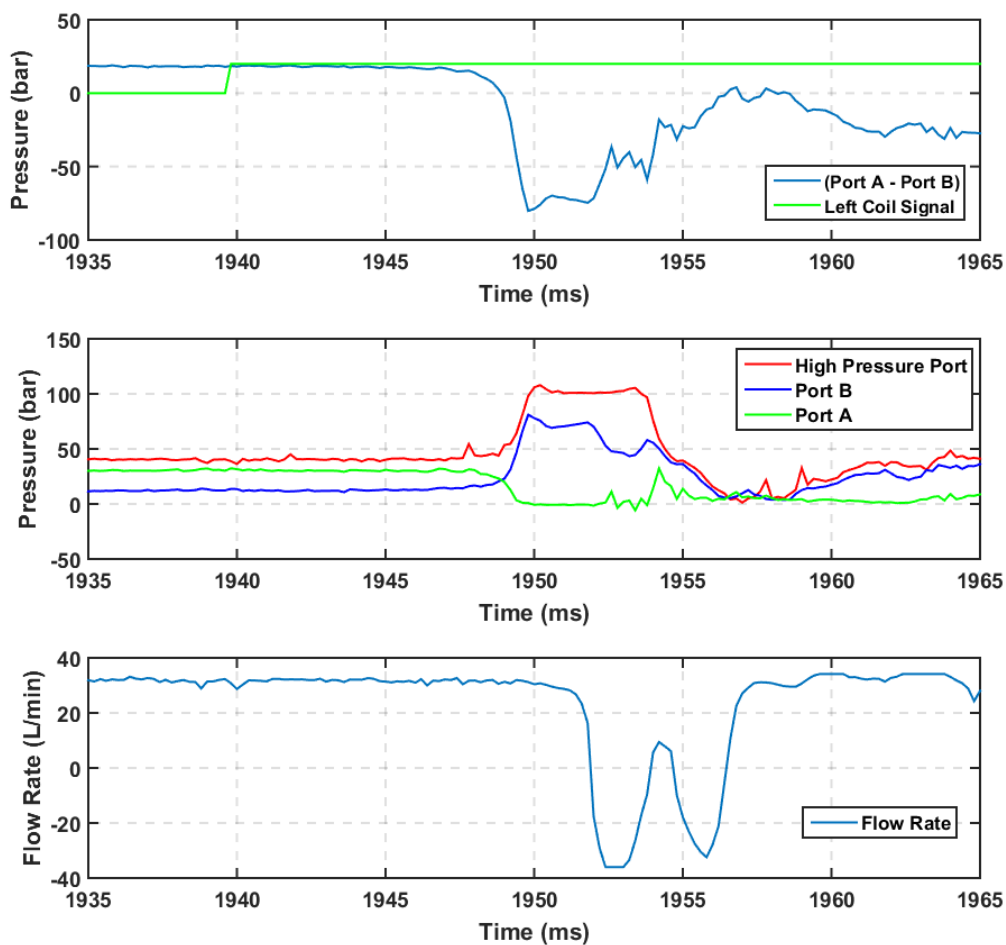


Figure 6.18: Switching high pressure from port A to port B

A delay of 9.2ms occurs before the pressure drop between the two ports drops 10% below a steady pressure of 17.9 bar until the two ports become equal at time 1948.8ms. At this

point, the valve is transitioning through its closed state, and system pressure builds up to the set pressure of the test stand relief valve. At time 1956.6ms, the working pressure port's A and B are again equal and port B now rises to the high pressure line signifying the position has changed fully from position 1 to position 3. The pressure at port B rises 90% higher than port A at time 1959.6ms near the end of Figure 6.18 signifying a full transition has taken place. This indicates a full response time of 19.6ms. The distance the spool valve has to travel in that allotted time is 6.2mm, 3.1mm for each position on the spool valve. Figure 6.19 depicts a similar story, only with the right coil set being energized. This moves the spool from position 3 to position 1. The initial valve delay is 11.2ms and the full response to 90% pressure drop after port A has been switched to the high pressure line is in 20.2ms.

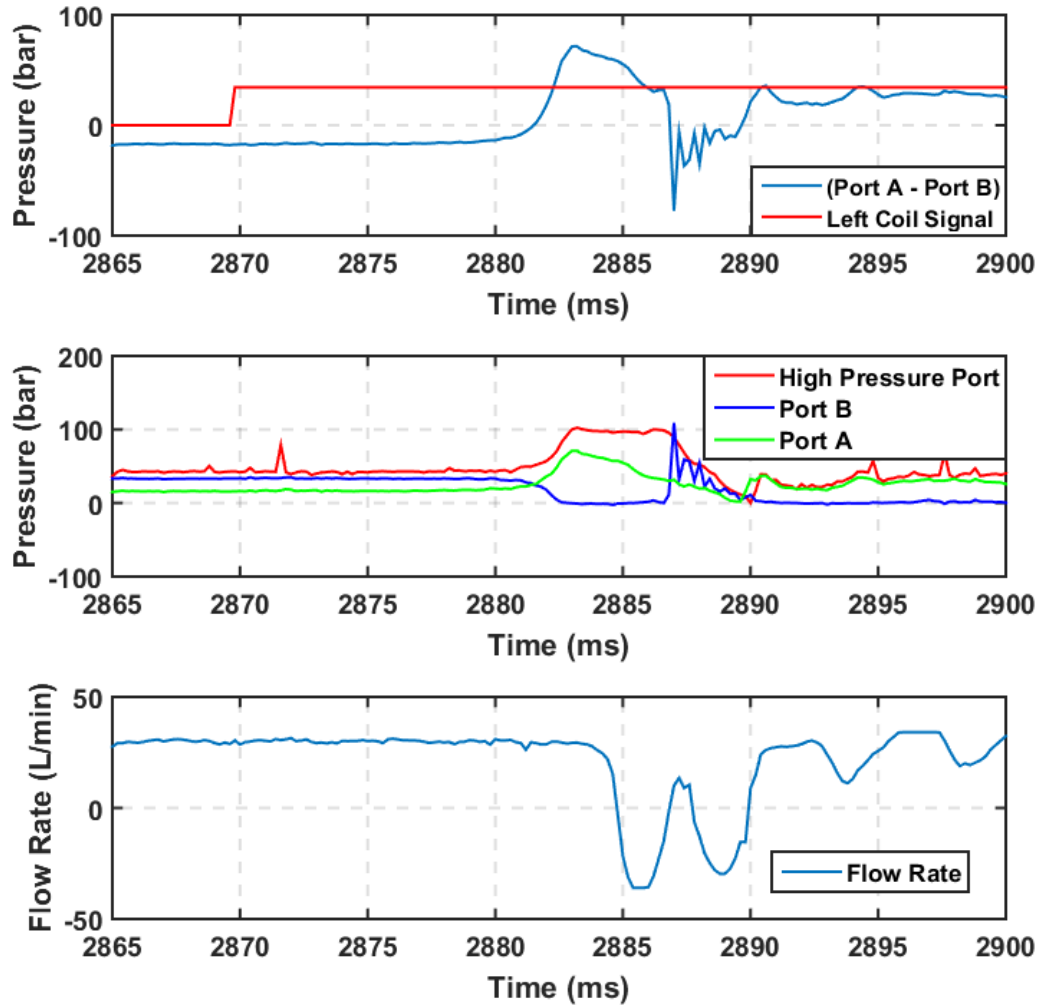


Figure 6.19: Switching high pressure from port B to port A

The larger initial valve delays under dynamic conditions were expected to be larger due to the spool's deadband along with the residual magnetism occurring inside the system. When actuating the valve from position 1 to 3 and vice versa, the total deadband is close to double that of the step response data sets, measured at 1.6mm before any pressure-flow characteristics can be recorded. The spool valve has a deadband of 0.8mm in either

direction of actuation. The friction and residual magnetism build up is enough to overpower the installed spring and hold the spool in place even after the signal is shut off. The best results for actuation came when the reverse peak duration was at 6ms, half that of the peak duration.

CHAPTER 7. CONCLUSION

The main research objective of this research was to integrate the energy coupling actuator with both a poppet and a spool valve body to experimentally investigate the performance of each. This would be done by developing an integrated electrical circuit, sensors, actuator, and valve into one assembly for experimental testing. Lastly the control for the valves were set to be bidirectional and proportional in output.

Initial research in describing the valve body's multiple domains of operation was completed and equations were formed to predict its performance. The electromagnetic model was created initially to predict the MR fluid's shear strength inside the actuator. CFD was done to model the hydraulic domain and solve for fluid flow forces given a pressure drop across the valve with laminar leakage and viscous friction. The mechanical domain tied together friction and reaction forces from the poppet acceleration. These subsystems aided in prototyping as they acted as a design tool for developing a high performance valve. Ultimately, however the design had to converge on manufacturability and what was available to purchase from off the shelf components.

A prototype ECAV and modified spool valve from Sun Hydraulics was modeled in CAD and manufactured. Experimental testing concluded the research. PQ curves were

generated for the machined poppet valve under steady state conditions. Investigation showed that the valve was capable of producing 80 L/min flow at a 5 bar pressure drop across the valve. Dynamic experiments proved that the spool outperformed the poppet valve in response times generated by about 10ms.

The experimental results served as a proof-of-concept for the poppet and spool valve actuation, however the overall design can be optimized further. Future work improving the performance of the valve overcoming limitations of MR fluid leakage as disk speed increases, friction inside the valve, and higher driving voltages will greatly impact the valve performance for the better. Previous work shows that voltages up to 96V can create faster response times on the order of magnitude of a few milliseconds when compared to a 48V peak voltage. Designing the actuator box with compactness in mind over ease of assembly could greatly reduce the profile of the valve. The box is larger than it needs to be currently to accommodate adequate space for both the spool and poppet valve for experimental result generation purposes. The actuator could easily be scaled to its operating usage. If large flow forces will never be seen in a particular application, then the disk and actuator box could scale down to size. An in-depth analysis on removing residual magnetism inside the actuator is another option to improve the performance. Tuning the reverse peak duration alone did not seem to diminish their effects fully. Lastly, the proportional, position feedback control needs to be developed to prove the ECAV can perform equal tasks of proportional valves found in industry today.

LIST OF REFERENCES

LIST OF REFERENCES

- Bergada, J. M., Watton, J. (2004). A direct solution for flowrate and force along a cone-seated poppet valve for laminar flow conditions. Proceedings of the Institution of Mechanical Engineers, Part I: Journal of Systems and Control Engineering.
- Bertin, M.J.F., Plummer, A. R., Bowen, C. R., and Johnston, D. N. An investigation of piezoelectric ring benders and their potential for actuating servovalves. In: Bath/ASME Symposium on Power Transmission and Motion Control FPMC2014, Bath, September 2014.
- Besch, B. (2012). "Introduction to Electro-hydraulic Proportional and Servo Valves." Fluid Power Conference & Expo. St. Paul, Minnesota. Lecture.
- Black, G. (2003). Seal Friction Measurement. Sun Hydraulics Corporation.
- Breidi, F., Helmus, T., Holland, M., & Lumkes, J. (2014). The Impact of Peak-and-Hold and Reverse Current Driving Strategies on the Dynamic Performance of Commercial Cartridge Valves. *Proceedings of the ASME/BATH 2014 Symposium on Fluid Power & Motion Control, Bath, UK.*
- Budynas, R., & Nisbett, J. (2008). Shigley's Mechanical Engineering Design (8th ed.). Boston: McGraw
- Chase, T., Hemstad, E., Hargus, A., Fikru, N. (2015). Development of a MEMS Pneumatic Valve. *2015 Fluid Power Innovation & Research Conference (FPIRC15)*
- Cui, P., Burton, R.T., & Ukrainetz, P.R. Development of a high speed ON/OFF valve. *International Off-Highway and Power Plant Congress and Exposition*, Milwaukee, Wisconsin, USA. September 9. - 12., 1991. pp. 21 - 25.
- EOS GmbH – Electro Optical Systems. (2008). Material Data Sheet for PA 2200.
- Fitch, E. & Hong, I. (2001) Hydraulic Component Design and Selection. Stillwater: BarDyne, Inc.

Gauthier, J., Hubert, A., Abadie, J., Chaillet, N., Lexcellent, C. Magnetic shape memory alloy and actuator design. Proceedings of the 5th International Workshop on Microfactories, IWMF'06., Oct 2006, Besancon, France. sur CD ROM - 4 p., 2006.

Hydac (2012). 2/2 Solenoid Directional Valve Poppet Type, Direct-Acting Normally Closed SAE-08 Cartridge – 250 bar Retrieved from: <http://www.hydac.com/de-en/products/valves/directional-valves-solenoid-operated/22-directional-poppet-valves/ws08w/show/Download/index.html>

Ivantysyn, J., & Ivantysynova, M. (2003). *Hydrostatic pumps and motors*. (S. N. Ali, Trans.) New Delhi, India: Tech Books International. (Original work published 1993).

Jeon, J., Han, C., Y.-M. Han and S.-B. Choi, “A New Type of Direct-Drive valve System Driven by a Piezostack Actuator and Sliding Spool,” *Smart Materials and Structures*, 2014.

Johnson, B., Massey, S., & Sturman, O. (2001). Sturman Digital Latching Valve. *Proceedings of the 7th Scandinavian International Conference of Fluid Power*.

Johnston, D. N. (eds.) *Power Transmission and Motion Control, PTMC2004*, pp. 297 - 308 (Professional Engineering Publishing Ltd, 2004).

Karunanidhi, S., Singaperumal, M. Design, analysis and simulation of magnetostrictive actuator and its application to high dynamic servo valve, *Sens. Actuators Phys.* 157 (2010) 185–197./24/

Krutz, G. S. (1999). In *Machine Design for Mobile and Industrial Applications* (pp. 103-108). SAE

Laamanen, A., Siivonen, L., Linjama, M. & Vilenius, M. (2004). Digital Flow Control Unit - an Alternative for a Proportional Valve? In: Burrows, C. R., Edge, K. A. &

Lauttamus, T., Linjama, M., Nurmi, M., Vilenius, M., A novel seat valve with reduced axial forces. *Power Transmission and Motion Control 2006*.

Linjama, D. M. (2008). *Digital Hydraulics Research at IHA*. Paper presented at the First Workop Digital Fluid Power, First Workop Digital Fluid Power.

LORD Corporation (2011). MRF-132DG Magneto-Rheological Fluid. LORD Technical Data.

Love, Lonnie J. (2012). Estimating the Impact (Energy, Emissions and Economics) of the US Fluid Power Industry. United States. doi:10.2172/1061537

- Lugowski, J. (2015). Flow force compensation in a hydraulic valve. ASME Bath 2015 Symposium
- Manring, N. (2004). Modeling spool-valve flow forces. Proceedings of IMECE04. November 13-20, 2004. Anaheim, CA, USA
- Manring, N. (2005). Hydraulic Control Systems. Hoboken: John Wiley & Sons, Inc.
- Mikkola, J., Ahola, V., Lauttamus., T., Luomaranta, M., Linjama, M. (2007). Improving Characteristics of On/Off Solenoid Valves. *The Tenth Scandinavian International Conference on Fluid Power, SICFP'07, May 21-23, 2007, Tampere, Finland*
- Merrill, K. (2012). Modeling and Analysis of Active Valve Control of a Digital Pump-Motor. Ph.D. thesis, Purdue University, West Lafayette, IN
- Merrill, K., Holland, M., Batdorff, M, & Lumkes, J. (2010). Comparative study of digital hydraulics and digital electronics. *International Journal of Fluid Power*, 11 (3), 45-51.
- Merritt, H. (1967). Hydraulic Control Systems. John Wiley and Sons. New York.
- MOOG. (2009). Servovalves Direct Drive Servovalves D633/D634 Catalog
- O'Handley, R. C. (2007) DOI: 10.1002/9780470022184.hmm425 In book: Handbook of Magnetism and Advanced Magnetic Materials. Massachusetts Institute of Technology, Cambridge, MA, USA
- Parker Fluid Power Seal Design Guide: EPS 5370. (2007). Parker Hannifin Corporation.
- Parker Hannifin. (2003). Drive and fluid technology: New hydraulic control valve goes down well thanks to its unbelievable performance. Courage to revolutionise. Press Report Kaarst.
- Parker Hannifin Corporation (2009). Operation Manual Series DFplus
- Parker O-Ring Handbook: ORD 5700. (2007). Parker Hannifin Corporation.
- Plummer, A. (2016). Electrohydraulic Servovalves - Past, Present, and Future. *10th International Fluid Power Conference Dresden, Smart Fluid Power. Vol. 2 405-424*
- Pohl, J., Sethson, M., Krus, P., & Palmberg, J., (2002). Modelling and validation of a fast switching valve intended for combustion engine valve trains. *Journal of Systems and Control Engineering*, 216, 105-116.
- Reuter, J.,Maerkl, S. and Jaekle M. (2010).Optimized Control Strategies for Fast Switching Solenoid Valves. *International Journal of Fluid Power, Vol.11(2010) No.3, pp.23-33.*

- Reynaerts, D., Van Brussel, H. (1998). Design Aspects of Shape Memory Actuators. *Mechatronics* 8 635-656
- Scheidl R., Kogler H., Winkler B.: Hydraulic Switching Control - Objectives, Concepts, Challenges and Potential Applications, in: Proceedings of 2012 International Conference of Hydraulics and Pneumatics, 7 - 9 November, Calimanesti-Caciulata, Romani, Page(s) 56-67, 2012.
- Sirohi, J., Chopra, I., 2003. Design and development of a high pumping frequency piezoelectric hydraulic hybrid actuator. *Journal of Intelligent Materials Systems and Structures*, 14(3):135-147. [doi:10.1177/1045389X03014003002]
- Skelton, D. (2014). Design of a High Performance Actuation System Enabled By Energy Coupling Actuation. Master's Thesis, Purdue University
- Sorensen, H., Numerical and experimental analyses of flow and flow force characteristics for hydraulic seat valves with difference in shape, *Proceedings of the Bath Workshop on Power Transmission & Motion Control, University of Bath, U.K, 1999.*
- Stone, J. (1960). Discharge Coefficients and Steady-State Flow Forces for Hydraulic Poppet Valves. *Journal of Basic Engineering*.
- Sturman, O. E. (1998). USA Patent No. 5718264. High Speed 3-way Control Valve
- Thoman, R. (1992). An empirical approach to seal friction. Aerotech '92. October 5-8. Anaheim, CA, USA.
- Truong, D. Q., Ahn, K. (2012). MR Fluid Damper and Its Application to Force Sensorless Damping Control System, Smart Actuation and Sensing Systems - Recent Advances and Future Challenges, Dr. Giovanni Berselli (Ed.), InTech, DOI: 10.5772/51391.
- Tu, H. C., Rannow, M., Wang, M., Li, P., Chase, T., and Van de Ven, J., 2012, "Design, Modeling, and Validation of a High-Speed Rotary Pulse-Width-Modulation On/Off Hydraulic Valve," *ASME J. Dyn. Sys., Meas., Control*, 134(6), p. 061002.
- Va, D., Edge, K., & Vaughan, N. (1991). Experimental investigation of flow and force characteristics of hydraulic poppet and disc valves. Proceedings of the Institution of Mechanical Engineers, Part A: Journal of Power and Energy, 205(31), 161-171.
- Van de Ven, J. D., and Katz, A., 2011, "Phase-Shift High-Speed Valve for Switch-Mode Control," *ASME J. Dyn. Sys., Meas., Control*, 133(1), p. 011003.

- Vaughan, N., Johnston, D., & Edge, K. (1992). Numerical simulation of fluid flow in poppet valves. *Proceedings of the Institution of Mechanical Engineers, Part C: Journal of Mechanical Engineering Science*, 206(23), 119-127.
- Watton, J. (2009). *Fundamentals of fluid power control*. Cambridge University Press
- Ivantysyn, J., & Ivantysynova, M. (2003). *Hydrostatic pumps and motors*. (S. N. Ali, Trans.) New Delhi, India: Tech Books International. (Original work published 1993).
- Wilfong G. (2011). Design and Dynamic Analysis of High Speed On/Off Poppet Valves for Digital Pump/Motors. Master Thesis, Purdue University.
- Winkler, B., Ploeckinger, A., & Scheidl, R. (2010). A Novel Piloted Fast Switching Multi Poppet Valve. *International Journal of Fluid Power*, 11(3), 7-14.
- Xiong, S. (2014). Multi-Physics Coupled Modeling and Analysis for the Design of High Speed Valves. PhD. Thesis, Purdue University
- Xu, B., Ding, R., Zhang, J., Su, Q., Modeling and Dynamic Characteristics Analysis on a Three-Stage Fast-Response and Large-Flow Directional Valve *Energy Conversion and Management Volume 79, March 2014, Pages 187–199*
- Yang, Z., He, Z., Li, D., Xue, G., Cui, X., Hydraulic amplifier design and its application to direct drive valve based on magnetostrictive actuator, *Sens. Actuators Phys.* 216 (2014) 52–63.
- Yousong, S., Yongwu, L., Shanshan, P., Mian, L. & Dinghua, L. A new type of fast-acting on-off valve. *Proceedings of the 1st International Symposium on Fluid Power Transmission and Control*, Beijing, China. October 13. - 15., 1991. pp. 34 - 37.
- Yifei, H., Shuxing, Y., Yu, W. & Fan, C. A method of removing the flow force on high speed electric-hydraulic on-off valves. *Fluid Power Transmission and Control Proceedings of the 2nd International Conference*, Hangzhou, China. 1989. pp. 305 - 307.
- .

APPENDIX

APPENDIX

Orifice Meter Calibration Curve

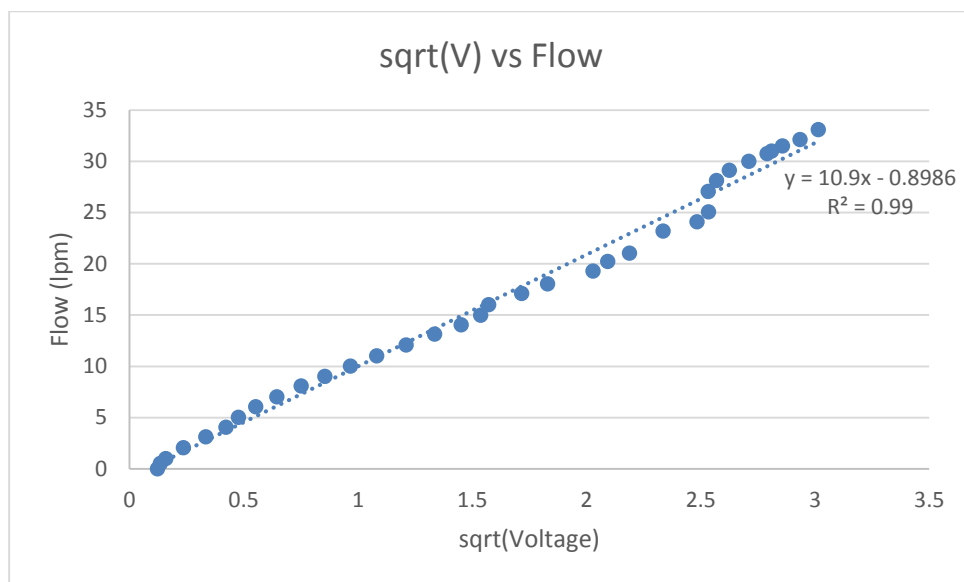


Table 7.1: Measured PQ for calibration

Voltage(V)	Q (lpm)	dp (PSI)	sqrt(V)
0.015472	0.002185	0.232086	0.124388
0.040436	1.390998	0.606537	0.201087
0.078385	2.487977	1.175774	0.279973
0.189888	4.638655	2.848317	0.435761
0.287995	5.854078	4.31993	0.536652
0.410296	6.912061	6.154435	0.640543
0.524689	7.743114	7.870331	0.724354
0.707318	8.710295	10.60977	0.841022
0.86558	9.486828	12.9837	0.930366
1.247167	11.04276	18.7075	1.116766
1.631978	12.40596	24.47967	1.277489
2.205939	13.47709	33.08909	1.48524
2.253805	14.65543	33.80708	1.501268
2.351863	15.61295	35.27795	1.533579
2.466116	16.56191	36.99173	1.570387
3.220522	17.78394	48.30783	1.794581
3.822424	19.50038	57.33636	1.955102
4.164759	20.37842	62.47138	2.040774
4.838854	21.34171	72.58281	2.19974
5.3043	22.65816	79.56451	2.303107
5.416245	24.10462	81.24367	2.327283
5.780959	25.16933	86.71439	2.404362
5.828816	26.19587	87.43223	2.414294
6.036152	27.29991	90.54228	2.456858
6.716226	28.61525	100.7434	2.591568
7.284695	29.67379	109.2704	2.699017
7.92992	30.66525	118.9488	2.816011
8.60746	31.61537	129.1119	2.933847
8.969398	32.40212	134.541	2.994895
9.202993	32.92579	138.0449	3.033643

PQ Measured Data for Extrapolating

